STUDY OF OUTPUT POWER OF BROADLY TUNABLE InGaAsP/InP AMQW LASERS

By

HESHAM M. ENSHASY, B.S., M. E.

A Thesis

Submitted to the School of Graduate Studies

in Partial Fulfillment of the Requirements

for the Degree

Doctor of Philosophy

McMaster University

DOCTOR OF PHILOSOPHY (2010) **McMaster University**

Department of Engineering Physics **Hamilton, Ontario**

TITLE: Study of output power of broadly tunable InGaAsP/InP AMQW lasers

AUTHOR: Hesham M. Enshasy, B. S. (University of Garyounis)

M. E. (Nebraska University – Lincoln)

SUPERVISOR: Professor Daniel T. Cassidy

NUMBER OF PAGES: XIX, 171

Abstract

Broadly tunable InGaAsP/InP asymmetric multiple quantum well (AMQW) ridge waveguide laser diodes suffer from low output power. The output power problem of the AMQW laser diodes limits the use of these lasers in certain applications. Both theoretical and experimental studies were carried out in this work to understand the reasons behind this output power problem and to put forth solutions to this problem. As a starting point a commercial beam propagation method (BPM) optical simulator was used to optimize the confinement factor of the laser diodes. The laser diode output power almost doubled as a result of optical confinement optimization, which opens the door for improvement from electrical and thermal optimization.

A commercially available partial differential equation solver, FlexPDE, was used to solve the main electronic and thermal equations and simulate a laser diode device. The FlexPDE simulations – which were validated with published data – showed poor current injection efficiency to the center of the device active region. The FlexPDE simulations showed that the main reason for this poor current injection efficiency is the ridge structure. Since the ridge structure is an essential part of this type of laser diode, effort was put forth to reduce the effect of the ridge structure on the current injection efficiency. Both simulation and experimental data showed that extending the doping profile closer to the active area would improve significantly the output power. On the other hand, a proposed forced electrical confinement method showed potential to improve the output power of the device theoretically and experimentally. The over all output power improvement went from a range of 2-5 mW to a range of 15-18 mW as a result of this

study. A discussion of the two distinct output power profiles is included in the study, while detailed explanations of the dip in the power profile supported by experimental data are reported.

A new method of distance measurement using one of the first, optimized, broadly tunable InGaAsP/InP short-external-cavity diode lasers is reported. Non-linear, least squares fitting method was used to extract estimates of distance from the raw data. This fitting method together with the wide tuning range (100 nm) made it possible to achieve sub–micron resolution of distance even in the presence of noise.

Acknowledgements

I would like to thank all the people who helped me through my Ph.D study and made this work possible. First I would like to express my deep gratitude to my supervisor, Dr. Daniel T. Cassidy, for his support and guidance throughout this work. I also would like to thank Dr. Brad. J. Robinson for growing the samples. Many thanks also to Ms. Doris V. Stevanovic, Dr. Zhilin Peng, and Dr. Doug Bruce for clean room training and help in processing the wafers.

Thanks to Dr. Ray LaPierre and Dr. Joseph Hayward, my other committee members for their effort and suggestions that led me to the right direction through this work.

I would like to thank my labmates Dr. Ferdous K. Khan, Dr. Jingcong Wang, Dr. Huiling Wang, and Jia Huiwen for the nice time and discussions we had together.

My parents, sisters, and brothers deserve my thanks for their encouragement and support. Thanks again for your love and help.

Finally, my wife deserves my biggest thanks for her unlimited support and encouragements. Thanks for being my wife and my best friend.

To my family

Table of Contents:

List of Figures:

Figure A.5: *J-V curve from published results and from simulation at different applied voltages.*

List of Tables

Chapter 1

1. Introduction:

Since their first appearance in 1975 by Van der Ziel *et al.*[1], quantum well (QW) diode lasers became very attractive for researchers because of their physical and technological importance. QW diode lasers are a physical representation of the particles-trapped-in-a-potential-well problem that is one of the basics found in college level text books on quantum mechanics. Quantum wells can be achieved by sandwiching a very thin low bandgap material with wider bandgap materials. It was estimated by Dingle and Henry[2] in 1976 that there is a reduction in carrier density for the same gain in QW lasers compared to bulk lasers. The many advantages of QW lasers, including but not limited to threshold reduction and room temperature operation, led to commercialization of this type of photonic device. Multiple quantum well (MQW) lasers were first reported by Holonyak *et al*[3]. in 1978, but the need for improvement in device performance and wavelength tunability was the driver to develop high quality MQW diode lasers.

Asymmetric MQW diode lasers are special cases of MQW diode lasers; they were first demonstrated by Ikeda *et al.*[4] in 1987. AMQW diode lasers have QWs of different compositions or different thicknesses in the same device. They are a promising light source for communication, sensing, and medical applications.

1.1. Ridge Waveguide AMQW Diode Lasers:

Wave guiding in laser diodes can take different mechanisms according to the laser design and application. Gain guiding, quasi-index guiding, and index guiding are three main guiding mechanisms of light in laser devices. For high quality beams and single spatial mode operation, researchers design and fabricate their lasers with ridge waveguides[5,6,7]. A ridge waveguide is a mesa of width of 2 – 3 μm and 0.5 – 3 μm of depth. The purpose of the ridge is to confine and center the light on the active area under the ridge, to select the fundamental spatial mode of the cavity, and to improve the beam quality of the laser light. Figure 1.1 shows a cross section illustration of a ridge waveguide laser similar to the lasers that are the target of my study. See Chapter 6 for the complete fabrication process of this type of laser.

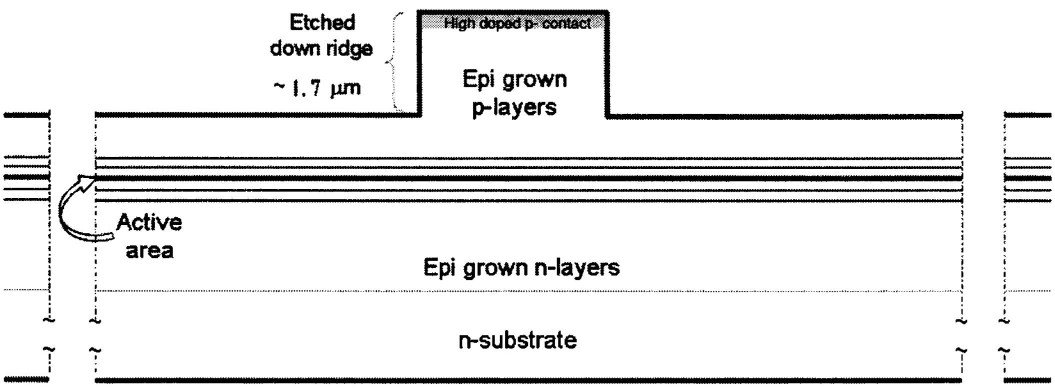

Figure 1.1: *Cross section of ridge waveguide laser similar to the laser under study. See Chapter 6 for full details of the fabrication process.*

Current confinement in this type of laser is formed by opening a via in the insulation layer on top of the highly doped p-contact layer and evaporating metallization above the opening – not shown in Figure 1.1. This way the current is expected to pass through the ridge to the active area underneath and pass through the n-substrate. So it is essential for single spatial mode operation and high beam quality to have the ridge formation as stated earlier.

As for the active area it can be a single quantum well (SQW) or multiple quantum wells (MQW). Ridge waveguide AMQW lasers, with single spatial mode operation and wide tunable range, show potential as a light source for many applications. Recent publications showed tuning ranges of over 100 nm for AMQW ridge waveguide laser diodes in different applications. For example; Woodworth *et al.*[8] were the first to show in 2001 that single AMQW ridge waveguide lasers can be used as widely tunable spectroscopic light sources for trace-gas detection. In 2007, Enshasy *et al.*[9] were the first to demonstrate that a single AMQW ridge waveguide laser can be used as a broadly tunable light source for sub-micron resolution distance measurement system without ambiguity (see Chapter 5 in this work). In 2008, Wang *et al.*[10] demonstrated that AMQW laser diodes can be used for optical coherence tomography (OCT).

AMQWs can be either compositionally[11] asymmetric, dimensionally asymmetric[12], or a mixture of both,[13] as shown in Figure 1.2. Compositionally AMQWs can be achieved by fixing the width of all QW's to the same width and changing the composition of each well to get different lasing wavelengths from the wells. Dimensionally AMQWs can be achieved by fixing the composition of all QW's to the same level and changing the width of the QW's, also to get different lasing wavelengths from the wells. The mixed AMQW can be achieved by changing both composition and dimension of each QW to get different wavelengths from each well.

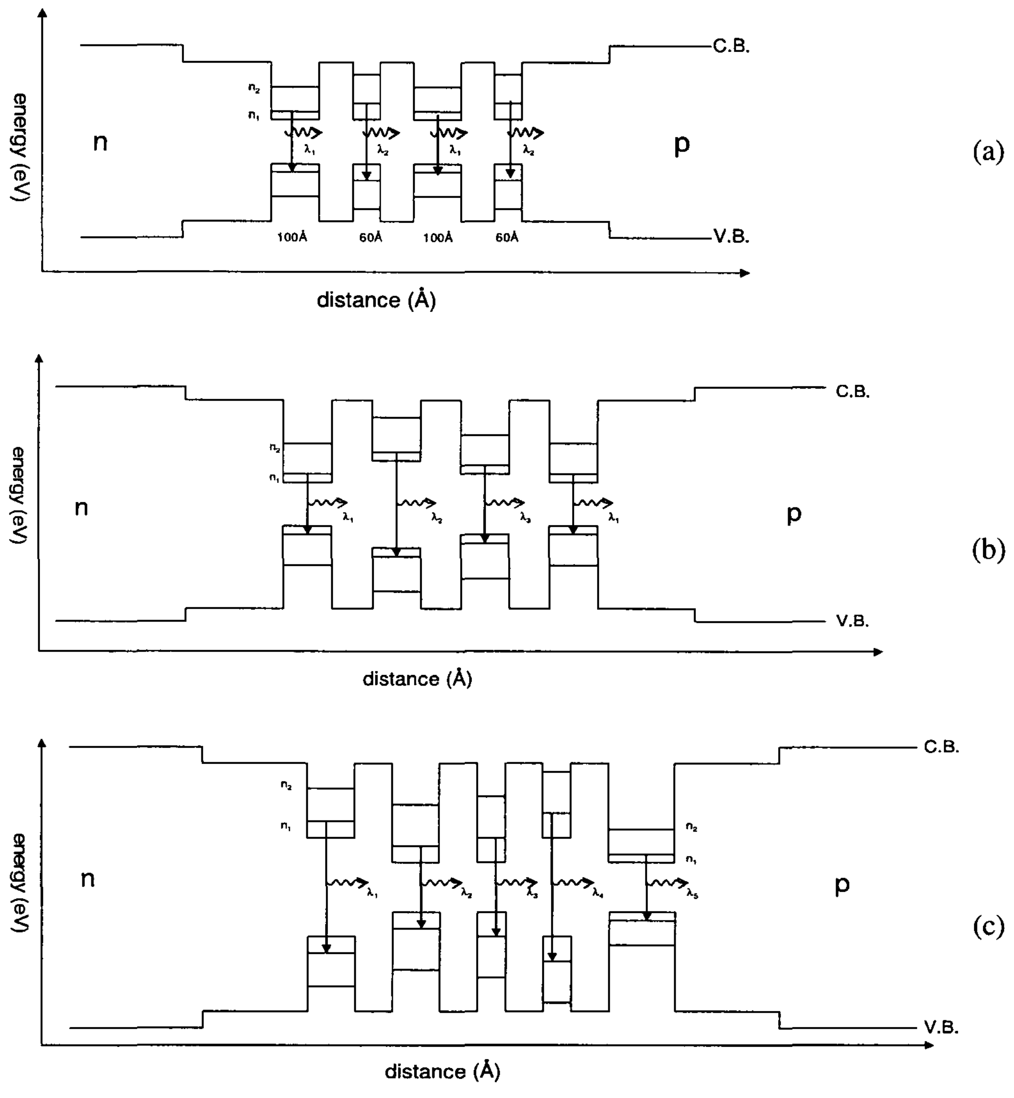

Figure 1.2: *Schematic band diagram of (a) dimensionally AMQW where the compositions of the wells are fixed but the dimensions are varying; (b) compositionally AMQW where the dimensions of the wells are fixed but the compositions are varying; and, (c) mixed AMQW laser diode where both dimensions and compositions of the wells are varying.*

Until now there has been no published study to favour one type of AMQW over another for certain applications. But what is known is that AMQWs can generate wide gain profiles[4, 8-13]. The wide gain profile allows for broad tuning ranges of AMQW laser diodes in most cases. Our group developed a simulation tool, ***k·p Sim,*** to simulate the QWs of the active region of laser diodes and thus estimate the gain profile of the laser. The user friendly software ***k·p Sim*** uses a Galerkin method[14] to calculate the wave functions for the entire structure using an exact envelope theory. The gain is estimated by finding the gain profile for each QW and then the total gain is the sum of all gain profiles. As an example of an AMQW ridge waveguide laser diode, consider structure 4261 that was designed by our group and grown at McMaster University using the gas source MBE. Structure 4261 gives a tuning range of > 100 nm[9, 10]. The structure consists of five compositionally asymmetric QWs of 100 Å width and separated by four 50 Å barriers. All barriers have the same composition of $(x, y) = (0.225, 0.355)$ where x is the mole fraction of gallium (Ga) and y is the mole fraction of arsenic (As). The structure is shown in Figure 1.3 where the first and the last QW have the same composition of $(x, y) = (0.225, 0.800)$. The second and third QW from the n side have the same composition of $(x, y) = (0.225, 0.690)$. The fourth QW has a composition of $(x, y) = (0.225, 0.71)$ where the important role of this well will be explained later in this section. These compositions give calculated photo luminescence (PL) wavelengths of λ_1= 1585 nm, λ_2 =1421 nm, and λ_3 =1449 nm.

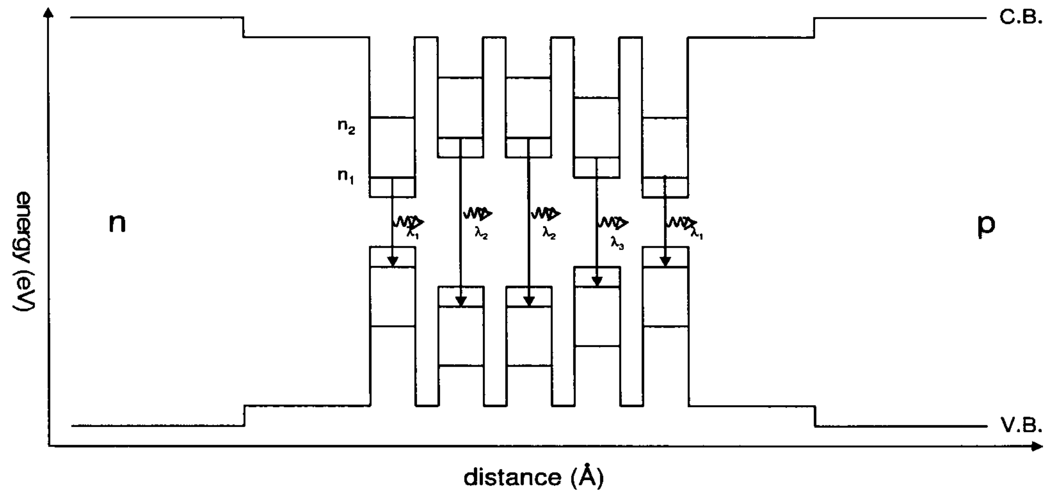

Figure 1.3: *Schematic band diagram of structure 4261. The structure consists of five 100Å wide compositionally asymmetric QWs and separated by four 50Å wide barriers of the same composition.*

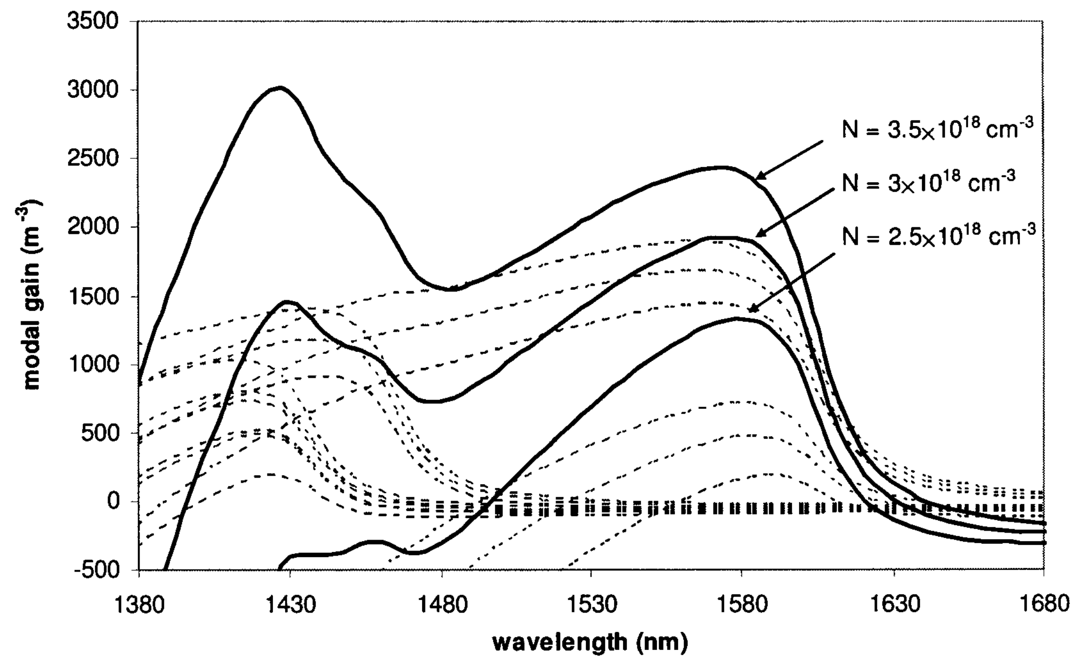

Figure 1.4: *The eight band* ***k·p Sim*** *simulation of modal gain for structure 4261 with carrier concentrations of (2.5, 3, 3.5)x10^{18} cm^{-3}. Solid lines show the total gain and dashed lines show gains from each well.*

The modal gain estimated by ***k·p Sim*** software for this structure is shown in Figure 1.4. The figure shows the modal gain for an eight band Hamiltonian at carrier concentrations of (2.5, 3, 3.5)$\times 10^{18}$ cm^{-3}. The solid lines represent the total gain and the dashed lines show the gains from each well. The eight band Hamiltonian is commonly used in the ***k·p*** method[15, 16]. The Hamiltonian is the eight-band Luttinger-Kohn model[17] for an electron in a quantum well and includes the doubly degenerate valence bands HH, LH and SO plus the doubly degenerate conduction band. The ***k·p Sim*** simulation in Figure 1.4 shows that by using an AMQW structure in the active area the total gain profile of the laser diode can be extended in wavelength. The total gain in the figure shows that the lasing will start at the longer PL wavelength wells (λ_1) and by increasing the current injection the lasing will shift to the shorter PL wavelength wells (λ_2, λ_3). This laser is designed for continuous tuning as much as possible by approximating a flat gain profile. This was done by inserting the fourth QW from the n side at an intermediate PL wavelength (λ_3). The effect of this well will be clearer in the measured gain curve that is shown in the next section.

Experimental results showed that the long wavelength of this laser light is determined by the long wavelength QWs (λ_1) and that the shorter wavelengths will be red shifted by no more than 50 nm from the rest of the QWs (λ_2, λ_3). Figure 1.5 shows a measured OSA intensity spectrum of this laser at different current injection levels. The spectrum clearly shows a red shift in the lasing wavelength (as compared to the expected wavelengths) for the shorter wells. Wang *et al.*[18] studied the red shift in AMQW extensively. They found that the absorption by the long wavelength wells is the reason for this red shift. This absorption is underestimated by the gain models; it should be taken into account in the design of the AMQW laser diodes. The measured PL intensity at room temperature for this structure is shown in Figure 1.6.

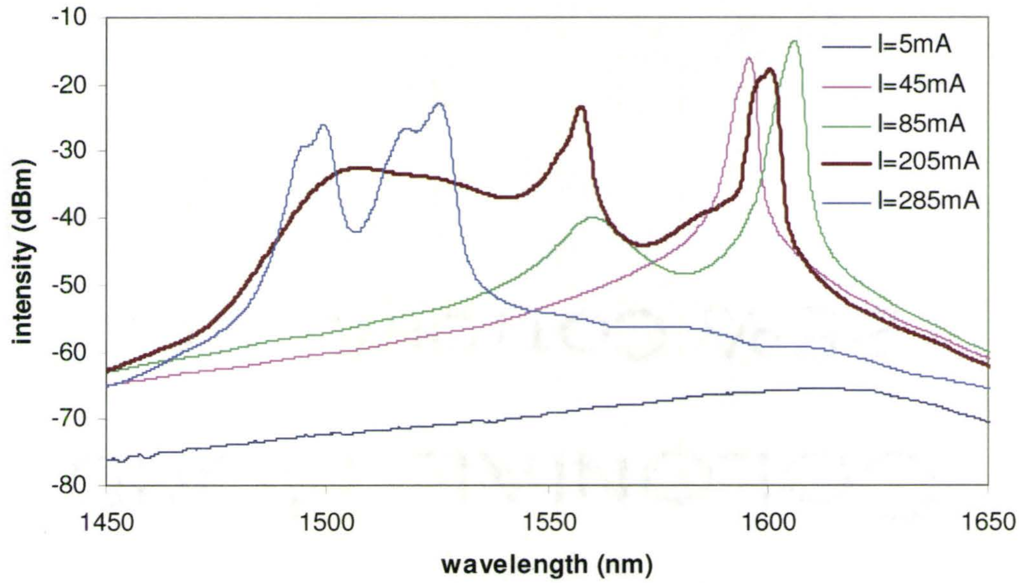

Figure 1.5: *Measured OSA intensity spectrum of 4261 AMQW diode laser at different injection current levels.*

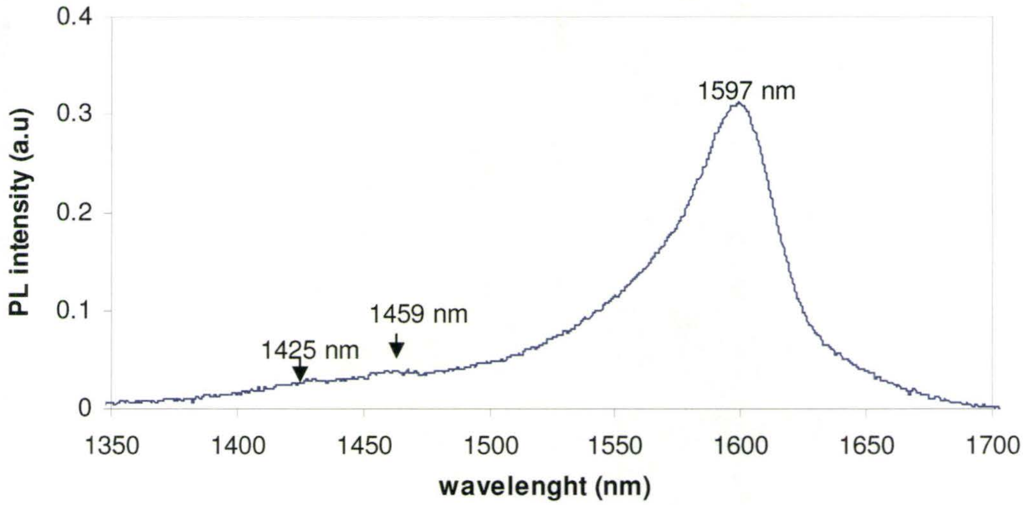

Figure 1.6: *Measured PL intensity for structure 4261 AMQW laser diode at room temperature.*

If one compares the measured PL peaks from Figure 1.6 with the measured laser spectra in Figure 1.5, one can clearly see that the red shift of the lasing peak at 1490 nm for the thin quantum wells is not a growth error. Instead, this shift happens when current is injected into the device but not when the wells are optically pumped as in the PL data of Figure 1.6. This supports the claim by Wang that the red shift is due to the interaction of the light with long and short wavelength wells. It is interesting to see that the shift appears clearly when current is injected into the device.

Despite the red shift phenomena in the AMQW, there exists a very wide tuning range using this type of diode laser. The maximum tuning range that our group achieved was demonstrated by Woodworth[11]. He experimentally showed that he could tune over a 172 nm range. However, a dip in the gain profile, which the third well is supposed to prevent, was deep enough to make it difficult to obtain operation on some of the modes in the middle of the tuning range. Wafer 4261 was a modified design where the devices can be tuned slightly over 110 nm and where operation on the modes in the middle of the tuning range is not difficult to obtain[9,10].

1.2. The power problem in the AMQW ridge waveguide laser diodes:

Ridge waveguide AMQWs can be fabricated with very broad tuning ranges (172 nm)[11] and with single spatial mode operation with a high quality beam profile. It has been mentioned in many publications that this type of laser always shows low power output. Huang *et al.*[13] for instance reported a maximum output power of 0.6 mW for their lasers, while Lin *et al.*[19] and Gingrich *et al.*[20] reported a maximum output power below 5 mW for their AMQW lasers. Our uncoated AMQW lasers give maximum output power in the range of 2-5 mW for each facet. Figure 1.7 show a plot of the measured output power for diode lasers from wafer 4261 as a function of injected current for 800 and 900 μm long laser bars with 3 μm ridge widths. A careful look at the output power profile for this AMQW ridge laser reveals clearly that heating effects limit the power output as shown by the power roll off at high current. The output power clearly peaks at an injection current > 180 mA. Also, one might expect slightly different power output for longer cavities while maintaining a similar light current profile. The output power profile seems to be altered by the laser length. However, the 900 μm long laser showed higher power, at least in the injected current range of 100-250 mA, than the 800 μm long laser.

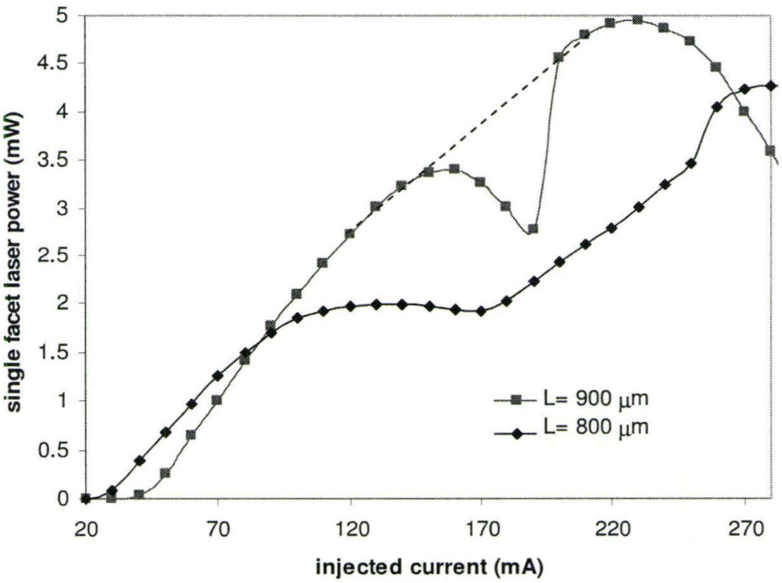

Figure 1.7: *Measured output power for uncoated 4261 lasers as a function of injected current (LI curve) for L=800 and L= 900 μm long lasers with W=3 μm ridge widths.*

A close examination of Figure 1.7 shows a second threshold around 180 mA. It is known that a single spatial mode QW laser has one threshold and an almost linear increase in power with current until a period of saturation before the roll off because of heating. However, this single QW laser power profile is present in our AMQW laser power output; but to see that we need to imagine extending the line after the first threshold with the same slope until it touches the second rise (see the dashed line in Figure 1.7). Now, several questions arise from the discussion so far. One can speculate as to why the AMQW lasers have that low output power. Also, why do AMQW ridge waveguide lasers have poor thermal management? What is the explanation behind this alteration of the output power profile? And finally, can one design AMQW lasers with better efficiency while preserving the wide tunable range? After all, the main purpose of AMQW lasers is to obtain wide tunable ranges.

The net gain curve for this laser calculated from the measured high resolution OSA spectrum using the method[21] reported by Wang is shown in Figure1.8. The net gain calculated at different current injection levels showed flat gain characteristics at injected current greater than 160 mA. To achieve broad tuning range we would like to operate the laser at the flattest gain possible, which is around 180 mA for this laser. However the output power profile in Figure 1.7 shows that the laser power suffers from a significant dip that reduces the power to almost one half. So, for this AMQW laser not only the maximum power is low but the useful operating point is at a point where almost half the maximum power of the laser is not available.

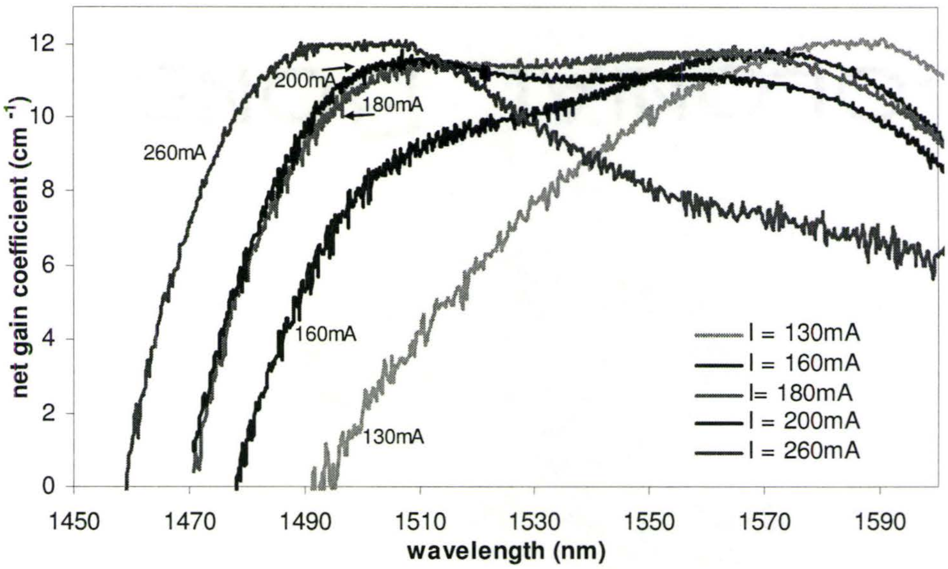

Figure1.8: *Net gain coefficient calculated from the measured OSA spectrum at different current injection levels.*

1.3. Thesis objective and layout:

The major goals of this thesis are: (i) to provide an understanding of the reasons for the lack of power of the AMQW ridge waveguide lasers; (ii) to find solutions to improve the laser power while maintaining the broad tunable range; and, (iii) to use this AMQW laser diode in useful applications that benefit from the wide tuning range as a first step for commercializing this laser.

In order to understand the power issue, a simple two dimensional electrical model is needed. Such a model can predict the carrier flow inside the laser to account for any leakages inside the device. Also, a two dimensional thermal model that is coupled to the electrical one will help in understanding the heating issue inside the device. Visualizing the thermal map of the device in two dimensions can help in understanding the problem and finding solutions for it. Thermal maps will help in the design for reduced heating of devices and consequently for higher power AMQW ridge waveguide laser diodes.

Another outcome of this work would be to assess the ability of FlexPDE[22] on handling such semiconductor problems. FlexPDE is a general purpose finite element method solver, and it can be used as a platform to solve systems of partial differential equations.

This thesis is divided into seven chapters. Chapter 1 is an introduction to AMQW diode lasers. In this chapter I talk about the history of these lasers and how these lasers evolved over time. Also, a brief description of the output power problem of AMQW ridge waveguide laser diodes is given. Chapter 2 is a description of the theoretical model that was used to simulate these lasers. The electrical model and the coupled thermal model equations that were used and the approximations used to simplify the model as much as possible will be discussed. In Chapter 3, the simulation results for the diode lasers will be discussed and analyzed. Information about the leakage problem in the 4261 laser diodes will be extracted from the simulation results and solutions will be proposed and studied theoretically. The effect of the doping profile on the laser performance is a part of these solutions together with forced electrical isolation on the device. Chapter 4 summarizes the experimental results from the optimized devices that was designed and processed to test the simulation results. Chapter 5 will be dedicated for using external cavity AMQW lasers in measuring distances with submicrometer resolution. It will be shown how the wide tuning range made it possible to achieve high resolution in this type of measurement. A unique method to extract the useful information from the raw data even in the presence of noise will be presented. Chapter 6 describes the fabrication process of the ridge waveguide AMQW laser diodes. In this chapter, it will be shown step by step how these devices were fabricated. Chapter 7 contains a summary of all the important results from this study; also a section devoted to a discussion regarding suggestions and future work is included in Chapter 7. Appendix A gives a comparison between the FlexPDE simulation results and published data for validation purposes and Appendix B lists all grown laser structures for this work.

Chapter 2

Theoretical Model

2.1. Introduction:

The problem of low output power, as we saw in the previous chapter, is an attribute associated with widely tunable asymmetric multiple quantum well (AMQW) laser diodes (LDs). Power losses can be related to poor current injection efficiency due to many factors. Current injection efficiency simply can be defined as the ratio of current passing through the active area under the ridge to the current injected into the laser diode. Current injection efficiency is one of the important parameters researchers have to examine when they work to improve the performance of widely tunable AMQW LDs. Many researchers use 1D[23, 24, 25] solutions of electrical and thermal models to understand the operation of laser diodes and hence improve the performance of semiconductor lasers. Through this work I found that 1D solutions are not sufficient to see all the required information. Instead, self consistent 2D solutions of coupled electrical and thermal models are required to visualize the current and temperature map of the device. Numerical solutions of the complete set of laser diode equations, which would include Poisson's equation, Schrödinger's equation, the current continuity equations, and the heat flow equation, are very complex because of the presence of Schrödinger's equation[23]. Simplicity is key to accommodate the finite size of devices and to give results in a reasonable time frame with reasonable amounts of computing power. This chapter gives details to the theory and physics behind calculations for the 2D model used to simulate and improve the design of AMQW LDs. To reduce the complexity of the calculation, a number of assumptions were made without affecting the main physics that describes semiconductor diode devices.

2.2. Electrical Model Overview:

The basic equations that describe the steady state carrier distributions in bulk semiconductors are actually derived from Maxwell's equations and the charge continuity equations[24]. These main three equations are Poisson's equation

$$\nabla \cdot (\varepsilon \nabla V) = \rho \qquad \text{Eq. 2.1}$$

and the electron and hole continuity equations

$$\nabla \cdot J_n - q\frac{\partial n}{\partial t} = qR\left(V, \phi_n, \phi_p\right) \qquad \text{Eq. 2.2}$$

$$\nabla \cdot J_p + q\frac{\partial p}{\partial t} = -qR\left(V, \phi_n, \phi_p\right) \qquad \text{Eq. 2.3}$$

where V is the electrostatic potential, ε is the dielectric constant, p and n are the hole and electron densities respectively, R is the recombination rate, q is the electron charge, J_n and J_p are the current densities for the electron and holes, and ρ is the charge density, which can be written as

$$\rho = q\left(p - n + N_d^+ - N_a^-\right) \qquad \text{Eq. 2.4}$$

In Eq. 2.4 N_d^+ is the density of ionized donors and N_a^- is the density of ionized acceptors. These quantities are explained in detail in Sec. (2.2.3).

In steady state conditions, the derivatives with respect to time equal zero. Thus Eq. 2.2 and Eq. 2.3 can be written in steady state as

$$\nabla \cdot J_n = qR\left(V, \phi_n, \phi_p\right) \tag{Eq. 2.5}$$

$$\nabla \cdot J_p = -qR\left(V, \phi_n, \phi_p\right) \tag{Eq. 2.6}$$

For current densities in this work the thermodynamic current densities were used. The thermodynamic current density relates the current densities to the gradient of the quasi-Fermi potentials. This form is good to model heterostructures and degenerate cases because it includes the general Einstein relation that deals with degenerate cases. Furthermore, the gradient of the quasi-Fermi potentials takes into account the current in heterostructure devices[25,26,27]. The thermodynamic current densities are

$$J_n = -qn\mu_n \nabla \phi_n = J_n\{n(V, \phi_n), \phi_n\} \tag{Eq. 2.7}$$

$$J_p = -qp\mu_p \nabla \phi_p = J_p\{p(V, \phi_p), \phi_p\} \tag{Eq. 2.8}$$

where μ_n and μ_p are the electron and hole mobility; and, ϕ_n and ϕ_p are the quasi Fermi potentials of the electrons and holes. In the next section the carrier densities will be shown but for now it will be left as a function of the quasi Fermi levels and the electrostatic potential. The benefit of the thermodynamic form is the inclusion of the general Einstein relations that deals with the degenerate cases[28], and the quasi-Fermi potential gradients that deal with the heterostructure devices[29]. By substituting Eq. 2.7, and Eq. 2.8 in Eq. 2.6 I get

$$\nabla \cdot J_n \{ n(V, \phi_n), \phi_n \} = qR(V, \phi_n, \phi_p) \qquad \text{Eq. 2.9}$$

$$\nabla \cdot J_p \{ p(V, \phi_p), \phi_p \} = -qR(V, \phi_n, \phi_p) \qquad \text{Eq. 2.10}$$

An examination of Eq. 2.9, Eq. 1.10, and Eq. 2.1 reveals three equations with three variables: the quasi Fermi levels for the electrons and holes, ϕ_n and ϕ_p; and, the electrostatic potential, V. By solving these three equations for the three variables one can solve for the current flowing in the device under study at zero or at different bias voltages. In this work a commercial finite element method (FEM) solver, FlexPDE, was used to solve these three equations and generate 2D solutions for this model that can be extended to 3D solutions. FlexPDE software is a general, script driven solution system for partial differential equations. One of the main outcomes of this thesis is to find out if FlexPDE software can handle solving semiconductor problems and can give useful solutions that can aid the design and improvement of device performance. Chapters 3 and 4 will shed some light in answering these questions.

2.2.1. Carrier densities *n* and *p*:

Carrier densities can be calculated with two approaches, i.e., one uses the Boltzmann statistics, which is good for non-degenerate cases, and the other one uses Fermi-Dirac statistics, which is a more general case. The intrinsic carrier density approach works very well with non-degenerate cases but for degenerate cases this approach leads to non physical bandgap narrowing[24,30, 31,32] with an effective intrinsic concentration modification. According to Marshak[33], this effective intrinsic approach works for degenerate cases when a little care is taken in the calculation.

2.2.1.1. Boltzmann statistics approach:

The electron and hole densities *n* and *p* are related to the corresponding quasi Fermi levels by the following auxiliary relations[24,25]

$$n = n_i e^{(\phi_n - E_i)/k_B T} \qquad \text{Eq. 2.11}$$

$$p = n_i e^{(E_i - \phi_p)/k_B T} \qquad \text{Eq. 2.12}$$

where n_i is the intrinsic carrier density, which is written as

$$n_i^2 = N_c N_v e^{-E_g/k_B T} \qquad \text{Eq. 2.13}$$

and E_i is the intrinsic energy level given by:

$$E_i = \frac{E_c + E_v}{2} + \frac{k_B T}{2} \ln\left(\frac{N_v}{N_c}\right) \qquad \text{Eq. 2.14}$$

In the above equations, k_B represents Boltzmann's constant; T is the device temperature in Kelvin; E_g represents the band-gap; E_c and E_v are the energy at the bottom of the conduction band and the top of the valence band respectively; and, N_c and N_v are the effective density of states in a parabolic conduction and valence bands approximation. N_c and N_v take the forms

$$N_c = 2\left(\frac{m_e^* k_B T}{2\pi\hbar^2}\right)^{3/2} \quad , \quad N_v = 2\left(\frac{m_h^* k_B T}{2\pi\hbar^2}\right)^{3/2} \qquad \text{Eq. 2.15}$$

By substituting Eq. 2.13 and Eq. 2.14 into Eq. 2.11 and Eq. 2.12 I get:

$$n = N_c e^{(E_c - \phi_n)/k_B T} = N_c e^{(\eta_n)} \qquad \text{Eq. 2.16}$$

$$p = N_v e^{(\phi_p - E_v)/k_B T} = N_v e^{(\eta_p)} \qquad \text{Eq. 2.17}$$

where η is the difference between the quasi-Fermi potential and the respective energy band edge.

In the case of a degenerate semiconductor one needs to use the effective intrinsic carrier density n_{ie} which is defined as follows

$$n_{ie} = n_i^2 e^{\Delta E_g / k_B T} \qquad \text{Eq. 2.18}$$

where ΔE_g takes into account the unphysical bandgap narrowing, which is needed to make the simple model fit, and it is a function of donor (N_d) and acceptor (N_a) concentrations[29].

2.2.1.2. Fermi-Dirac statistics approach:

The density of states approach is used to describe degenerate materials. In this approach, Fermi-Dirac statistics together with the electron or hole density of states are used to write the carrier densities as[24, 34]

$$n = \int_{-\infty}^{\infty} N_e(E) f(E) dE \qquad \text{Eq. 2.19}$$

$$p = \int_{-\infty}^{\infty} N_h(E)(1 - f(E)) dE \qquad \text{Eq. 2.20}$$

where $f(E)$ is the Fermi-Dirac distribution

$$f(E) = \left(1 + e^{\frac{E - E_f}{k_B T}}\right)^{-1} \qquad \text{Eq. 2.21}$$

A common assumption is made that $f(E)$ applies to non-equilibrium conditions where the carriers in each band are considered to be in equilibrium but the bands are not in equilibrium. Under this assumption, the Fermi energy is split into quasi Fermi levels ϕ_n for electrons and ϕ_p for holes. $N_x(E)dE$ is the total number of states with energy between E and $E+dE$ and is known as the density of states function for $x = e$ for electrons or $x = h$ for holes.

If a parabolic band minima model is used then the density of states for electrons and holes can be written as[24,26,35]

$$N_e(E) = \begin{cases} \frac{1}{2\pi^2}\left(\frac{2m_e^*}{\hbar^2}\right)^{3/2}(E-E_c)^{1/2} & E \rangle E_c \\ 0 & E \langle E_c \end{cases} \qquad \text{Eq. 2.22}$$

$$N_h(E) = \begin{cases} \frac{1}{2\pi^2}\left(\frac{2m_h^*}{\hbar^2}\right)^{3/2}(E_v-E)^{1/2} & E \langle E_v \\ 0 & E \rangle E_v \end{cases} \qquad \text{Eq. 2.23}$$

where $m_e^*(m_h^*)$ is the effective mass for electrons (holes).

Using the above approximations, the carrier densities in Eq. 2.19 and Eq. 2.20 can be written as:

$$n = N_c F_b(\eta_n) \qquad \text{Eq. 2.24}$$

and $$P = N_v F_b(\eta_p) \qquad \text{Eq. 2.25}$$

where N_c and N_v are the effective density of states described in Sec. 2.2.1.1; η_n and η_p are the degeneracy levels, which take the forms

$$\eta_n = (\phi_n - E_c)/k_B T \quad , \quad \eta_p = (E_v - \phi_p)/k_B T \qquad \text{Eq. 2.26}$$

and the term $F_b(\eta)$ is the Fermi-Dirac integral of order b which can be written as

$$F_b(\eta) = \frac{1}{\Gamma(b+1)}\int_0^{\infty}\frac{x^b dx}{1+e^{(x-\eta)}} \qquad \text{Eq. 2.27}$$

Many researchers[36, 37, 38, 39, 40] put forward an approximate analytical formula for the Fermi-Dirac integral. In this study I am using the form

$$F_b(\eta) = \left(e^{-\eta} + C_b(\eta)\right)^{-1} \qquad \text{Eq. 2.28}$$

where b=1/2 is used in this work, and

$$C_{1/2}(\eta) = \frac{3(\pi/2)^{1/2}}{\left(\eta + 2.13 + \left(|\eta - 2.13|^{12/5} + 9.6\right)^{5/12}\right)^{3/2}} \qquad \text{Eq. 2.29}$$

according to Humett[39].

It is useful to know that when the degeneracy level $\eta << 0$, the Fermi-Dirac integral $F_{1/2}(\eta) \sim e^{\eta}$ which means that carrier densities go back to Boltzmann statistics that were discussed in the previous section.

2.2.2. Recombination:

Recombination is the term on the right hand side of the current continuity equations, Eq. 2.9 and Eq. 2. 10, which accounts for the generation and recombination of carriers. This recombination term is a total of three recombination mechanisms such as Auger (R_{Au}), radiative recombination (R_B), and Shockley-Read-Hall (R_{SRH}). Auger recombination is an electron or hole capture or emission while the energy released is taken by a third party electron or hole. Radiative recombination is the recombination that results from spontaneous and stimulated emission, where an electron from the conduction band recombines with a hole from the valence band and the energy is emitted as light.

Shockley-Read-Hall is a general recombination process that uses deep level impurities in the bandgap of the device.

2.2.2.1. Auger recombination:

Auger recombination is a three carrier interaction; thus it is proportional to the cube of the carrier concentration. This proportionality means that Auger recombination is more important in the high injection regime than any other regimes. The total Auger recombination rate can be expressed as[24]:

$$R_{Au} = \left(C_n n + C_p p\right) \left[np - n_i^2\right] \qquad \text{Eq. 2.30}$$

where C_n and C_p are Auger coefficients for electron-electron-hole and electron-hole-hole interaction. The term $[np\text{-}n_i^2]$ in Eq. 2.30 ensures that the net recombination rate vanishes at thermal equilibrium.

2.2.2.2. Radiative recombination:

The radiative recombination was assumed to be due to spontaneous emission – ignoring the stimulated emission part – where the rate of recombination takes the form[41,42,43]

$$R_{rad} = B(np - n_i^2) \qquad \text{Eq. 2.31}$$

where B is the radiative coefficient, which is related to the material properties[43] of the semiconductor. As in Auger recombination the term $[np\text{-}n_i^2]$ in Eq. 2.32 ensures that the rate of emission and absorption are equal at equilibrium. Ignoring the stimulated emission part from the radiative recombination was to simplify the model. Since I am optimizing the electrical and thermal properties of the device, stimulated emission will not add significant contributions to my study. Instead the addition of the stimulated emission will require solving a new equation which will add more complexity to the model. Furthermore, in my model the level of carrier injection can be controlled by fixing the injected current at a certain level, so there is no need for the stimulated emission term to clamp the carrier concentrations at a certain level.

2.2.2.3. Shockley-Read-Hall recombination:

Shockley-Read-Hall recombination is a thermal recombination that uses impurities in the bandgap as recombination centers to capture and emit carriers. For simplicity it is common practice in semiconductor modeling to use a Shockley-Read-Hall recombination term in the continuity equation[42,44,45]. The Shockley-Read-Hall recombination can be expressed in the form

$$R_{SRH} = \frac{np - n_i^2}{\tau_n\left(p + p_T\right) + \tau_p\left(n + n_T\right)} \qquad \text{Eq. 2.32}$$

where τ_n and τ_p are the electron and hole life time, and p_T , and n_T are the electron and hole trap or impurity densities. If the trap level is assumed to be in the middle of the bandgap[41], then p_T and n_T can be replaced with n_i. In Shockley-Read-Hall recombination, as in Auger and radiative recombination, the term $[np-n_i^2]$ in Eq. 2.32 ensures the disappearance of the recombination term at thermal equilibrium.

For degenerate semiconductors, Shockley-Read-Hall recombination can be used if the intrinsic carrier density is replaced by the effective intrinsic carrier density[24], as discussed in Sec. (2.2.1.1). Otherwise, the degenerate model of the thermal recombination presented by Roos[46]

$$R(V,\phi_n,\phi_p)=\frac{N_cF_b(\eta_n)N_vF_b(\eta_p)\left(1-e^{\eta_n+E_g+\eta_p}\right)}{\tau_nN_vF_b(\eta_p)e^{\eta_p-E_t+E_g}+\tau_pN_cF_b(\eta_n)e^{\eta_n+E_t}} \qquad \text{Eq. 2.33}$$

can be used. The thermal recombination form presented in Eq. 2.33, which has been used in this work, follows the same analogy as Shockley-Read-Hall recombination but it uses the degenerate approach discussed in Sec. (2.2.1.2).

2.2.3. Ionized donors (N_d^+) and acceptors (N_a^-) densities:

The ionized donors and acceptors densities that are present on the right hand side of Poisson's Eq. 2.4 depend on the ionization energy[47]. These ionized densities can take the forms

$$N_d^+=N_d\left(1-\left(1+\frac{1}{C_d}e^{\eta_n-\frac{E_d}{k_BT}}\right)^{-1}\right) \qquad \text{Eq. 2.34}$$

$$N_a^{-} = \frac{N_a}{1 + C_a e^{\eta_p + \frac{E_a}{k_B T}}} \qquad \text{Eq. 2.35}$$

where C_d is the ground state degeneracy factor of the donor levels and equals 2 and C_a is the ground state degeneracy factor of the acceptors level and equals 4 in the case of InGaAsP materials[24]. E_a and E_d are small positive and negative fractions of the band gap.

2.2.4. Band gap and energy bands structure:

Band gaps for ternary and quaternary materials of the binary materials InP, GaAs, InAs, and GaP depend on the composition. The lattice constant and band gap of materials are set by controlling the mole fraction of the binary constituents. For example, for ternary compounds such as $In_{1-x}Ga_xAs$ a range of band gaps spanning from 0.354 eV (for InAs) to 1.424 eV (for GaAs) can be realized by changing the mole fraction of Ga from 0 to 1.

In general one uses a general interpolation formula, Vegard's Law, to find the physical parameters of the ternary and quaternary compounds. For quaternary compounds the general interpolation formula follows the relation[48]:

$$\begin{aligned} P(A_x B_{1-x} C_y D_{1-y}) = {} & xyP(AC) + (1-x)(1-y)P(BD) \\ & + (1-x)yP(BC) + x(1-y)P(AD) \end{aligned} \qquad \text{Eq. 2.36}$$

where $P(AC)$, $P(BC)$, $P(AD)$, and $P(BD)$ are the physical parameters for the binary materials taken from experiment. Table 2.1 gives some of the important binary material data that was used in the model. Consequently the lattice constant of quaternary materials such as $In_{1-x}Ga_xAs_yP_{1-y}$ follow the formula

$$a(x,y) = 5.8688 - 0.4176\,x + 0.1896\,y + 0.0125\,xy\ \text{Å} \qquad \text{Eq. 2.37}$$

where x and y are the Ga and As mole fraction respectively. For $In_{1-x}Ga_xAs_yP_{1-y}$ quaternary materials that are lattice matched to InP the mole fraction is obtained by using the following formula

$$x = \frac{0.189y}{0.4184 - 0.013y} \qquad \text{Eq. 2.38}$$

Table 2.1: Physical properties of binary materials that were used in the model[24,54,55,56]

Physical properties @ 300 K	InP	GaP	GaAs	InAs
Lattice constant a (Å)	5.869	5.451	5.653	6.058
Band gap Eg (eV)	1.35	2.74	1.42	0.36
Thermal conductivity k (W cm^{-1} K^{-1})	0.68	0.77	0.44	0.27
m_e^*/m_0	0.077	0.254	0.0665	0.023
m_{hh}^*/m_0	0.6	0.67	0.5	0.4
M_{lh}^*/m_0	0.12	0.17	0.087	0.026
Elect. mobility μ_n(cm^2/Vs)	5370	160	9200	3300/2000
Hole mobility μ_p (cm^2/Vs)	150	135	400	100/450
Dielectric constant ε (F/m)	12.56 ε_0	11.11 ε_0	13.1 ε_0	15.15 ε_0
Intrinsic carrier concentration n_i (cm^{-3})	1.2×10^8		2.1×10^6	1.3×10^{15}

The band-gap of $In_{1-x}Ga_xAs_yP_{1-y}$ quaternary materials has been found to fit the following equation[24,49,50] at room temperature (300K):

$$E_g = 1.344 + 0.668\ x - 1.068\ y + 0.758\ x^2 + 0.078\ y^2 - 0.069\ xy - 0.322\ x^2 y + 0.03\ x y^2 \qquad \text{Eq. 2.39}$$

To plot the band structure of the laser diode devices simulated in this study, the conduction band energy (E_c) and the valence band energy (E_v) were written as

$$E_c = E_0 + 0.5\ E_g - qV - \chi \qquad \text{Eq. 2.40}$$

$$E_v = E_0 - 0.5\ E_g - qV + \chi \qquad \text{Eq. 2.41}$$

where χ is the electron affinity and E_0 is the vacuum energy. There are different ways to define the vacuum level, however in this study the vacuum energy (E_0) is defined as zero energy. In this way the Fermi energy will be at zero energy at equilibrium with no bias voltage.

A typical band structure for a simple laser diode device as an example for devices under study is shown in Figure 2.1. The figure shows the device assuming no interaction Figure 2.1(a): after equilibrium Figure 2.1(b): and, with a forward bias of ~ 0.6 V Figure 2.1(c). It is clear that at equilibrium, the drift and diffusion forces work to line-up Fermi levels which cause the famous band structure bending because of the formation of the electrostatic potential. When a small forward bias is applied, this bias works against the built-in electrostatic potential. As a result, the band bending reduces and a splitting of the electron and hole quasi Fermi levels occurs as shown in Figure 2.1(c).

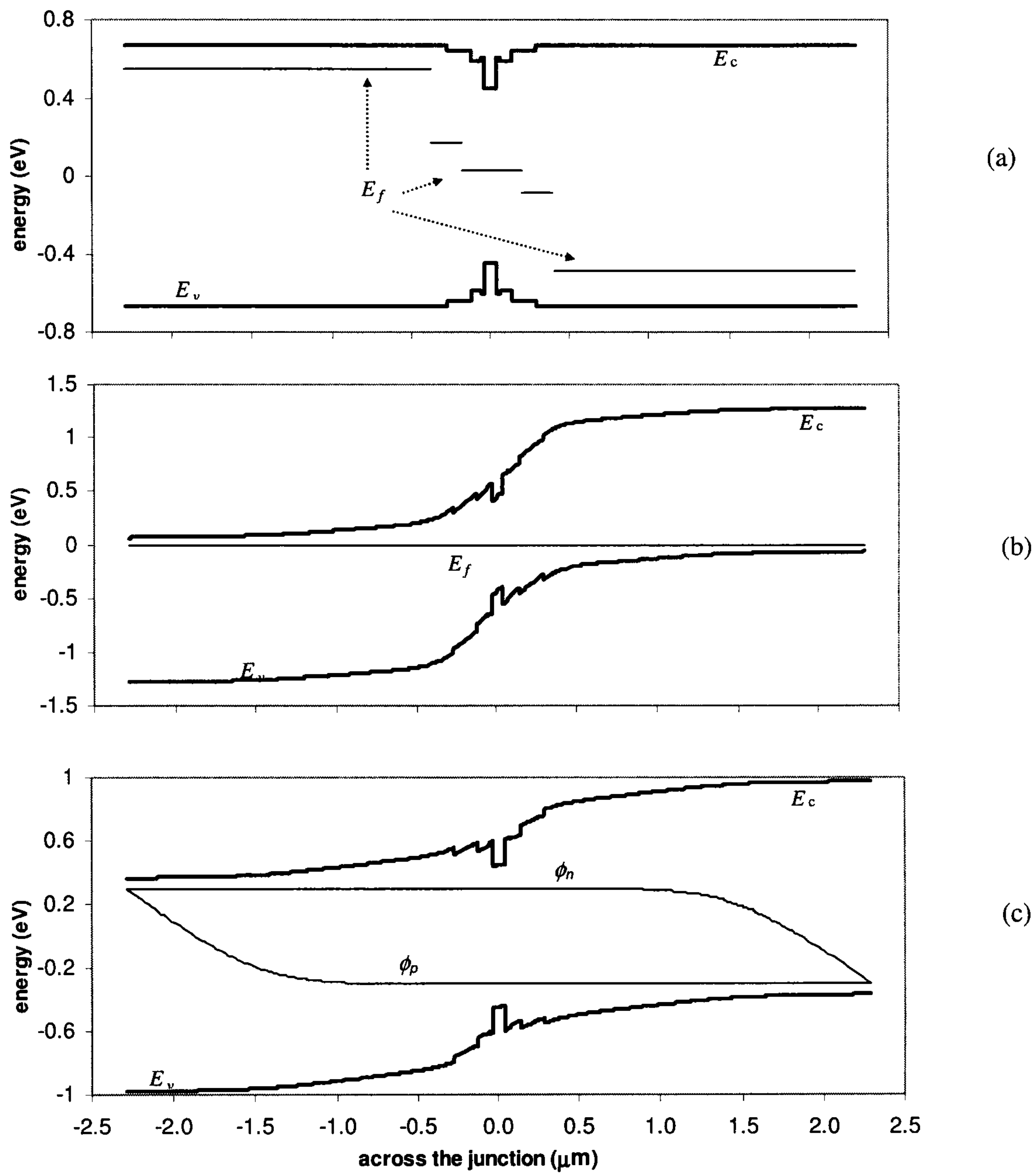

Figure 2.1: *Band structures for a simple laser diode. (a) Band structures of the materials assuming no interaction (b) Device after equilibrium drift and diffusion forces lineup the Fermi levels creating an electrostatic potential that causes bending of the bands. (c) Device at forward bias where the applied voltage reduces the electrostatic potential and the electron and hole quasi Fermi level separate.*

2.3. Coupled Thermal Model Overview:

Thermal management in laser diode devices is a key for a successful high power laser design. Convection, radiation, and conduction are the three mechanisms by which semiconductor devices can exchange heat energy with the surrounding environment[51]. Convection is a result of the transfer of heat energy by the motion of particles when there is a temperature gradient. In our study the air flow on top and around the laser transfers energy between the laser device and the environment. Radiation occurs when electromagnetic waves are transmitted from the device. Electromagnetic waves can be transmitted from the laser diodes as blackbody radiation (which is small and neglected in this study) or as radiated power through electrical pumping and spontaneous and stimulated emission. My concern is of the non-radiative energy that increases the heat inside the laser device. Conduction is the result of atomic vibrations and collisions where there is no translational motion involved, which is typical for solid devices. The heat continuity (conduction) equation is used to model the heat flow through a semiconductor device[52, 53]. By solving the heat continuity equation, a temperature profile for the device can be obtained. The heat continuity equation takes the form

$$\nabla \cdot k \nabla T = -g \qquad \text{Eq. 2.42}$$

where k is the thermal conductivity of the material, g is the heat power generated by heat sources inside the device layers per unit volume, and T is the temperature. It is important to note that all three variables in Eq. 2.42 are position dependent so the thermal conductivity can not be taken out of the divergence in this case.

Thermal conductivity is a physical parameter that depends on the mole fraction of the ternary or quaternary materials. As discussed earlier in Sec. (2.2.4) the parameters that depends on the mole fraction can be estimated by an interpolation method following Vegard's Law from the known binary alloy data. This is correct to some degree especially with material parameters of III-V compound alloys for experimental data that show a linear behavior such as the lattice and the dielectric constant. However Adachi[54], Nakwaski[55], and Gudent[56] discuss the nonlinearity of the relation for thermal conductivity. They present simple formulas to estimate the thermal conductivity of ternary and quaternary III-V compounds with bowing (nonlinearity) through strain and mass point defects to compensate for the deviation in experimental data. For ternary material the thermal conductivity formula takes the form

$$k_{A_xB_{1-x}C}(x) = xk_{AC} + (1-x)k_{BC} + \lambda_{A-C}x(1-x) \qquad \text{Eq. 2. 43}$$

whereas for quaternary material it takes the form

$$\begin{aligned} k_{A_xB_{1-x}C_yD_{1-y}}(x,y) &= (1-x)yk_{AC} + (1-x)(1-y)k_{AD} + xyk_{BC} \\ &\quad + x(1-y)k_{BD} + \lambda_{A-B}x(1-x) + \lambda_{C-D}(1-y) \end{aligned} \qquad \text{Eq. 2. 44}$$

where k_{AC}, k_{BC}, k_{AD}, and k_{BD} are the thermal conductivity for the binary materials. For experimental data see Table 2.1. λ_{A-C}, λ_{A-B}, and λ_{C-D} are the contributions arising from the lattice disorder generated by the random distribution of A and C, A and B, and C and D atoms in the cationic and anionic sub-lattice. The best fitting values[54] of λ_{A-C}, λ_{A-B}, and λ_{C-D} are 20, 70, and 30 W^{-1} *deg cm* respectively.

The heat is generated inside the device volume in the different layers according to the following processes:

1- In all layers heat is generated by Joule heating[53].

2- In p cap and SCH layers heat is generated by Joule heating, by the absorbed fraction f of spontaneous emission from the active region, and by energy decreases due to band gap changes[57].

3- In the active layer heat is produced by non-radiative recombination, re-absorption of the radiation[58], and energy decreases due to band gap changes. So below threshold ($I \leq I_{th}$) the heat generated in the different layers take the form:

$$\begin{aligned} g_{active} &= V_j I (1 - \eta_{spon}) + V_j I \eta_{spon} (1 - f) + \Delta E_{c,v} \\ g_{(cap, sub, SCH)} &= V_j I \eta_{spon} (f/2) + \Delta E_{c,v} + I^2 R_s \end{aligned} \qquad \text{Eq. 2.45}$$

where V_j is the junction voltage; η_{spon} and η_{ext} are the internal quantum efficiency of the spontaneous emission and the external differential quantum efficiency respectively; η_i is the internal efficiency of the lasing; and, R is the series resistance of the layer. f is the fraction of the absorbed power passing through the SCH and cap layers and it can be determined as[58]:

$$f = 1 - \sqrt{1 - \left(\frac{n_{clad}}{n_{active}}\right)^2} \qquad \text{Eq. 2.46}$$

where n_{clad} and n_{active} are the cladding layer and active layer refractive indices.

To couple the thermal model to the electrical model, the FlexPDE solver solves Eq. 2.1, Eq. 2.9, Eq. 2.10, and Eq. 2.42 simultaneously where the temperature term (T) in the equations in Sec. 2.2 is a feedback from the solution of Eq. 2.42. In this way we can achieve coupled 2D solutions to all four variables (V, ϕ_n, ϕ_p, T) needed to characterize, to study, and to optimize the electrical and thermal design of AMQW InGaAsP widely tunable semiconductor diode lasers.

In the next chapter, the simulation results achieved by using this model will be discussed.

Chapter 3

AMQW Ridge Waveguide Laser Diode Simulations

In this chapter, the results from simulations of laser diodes are presented. A commercially available partial differential equation solver, Flex PDE, was used to solve the main four equations presented in Chapter 2 (Poisson's equation, current continuity equations, and heat flow equation). The theoretical work presented in the previous chapter was used to create the simulator and to find the design optimizations and improvements on the device structure. The model presented in Chapter 2 is validated against published data in Appendix A.

In this work three assumptions were considered to ensure a reasonable amount of time was used to obtain convergence of the solutions and accurate simulation results. Since the interest was in a tuning range of > 100 nm, I was not interested in modifying the active area. The whole active region was considered as an average single quantum well to reduce the calculation time. A simple way to define an average active region is to multiply the thickness of each layer in the active region with the composition, add all results, and then divide by the total thickness of the active region. A second consideration in the simulations was to set the n-side (bottom) of the device on a heat sink and to keep the temperature of the heat sink fixed at 16°C. This was done because in operation lasers need to be cooled down to keep running otherwise they will turn off from the accumulation of the generated heat. A goal of work such as this is to reach the point where a widely tunable laser will work at room temperature without any cooling devices attached.

The third consideration is how the air flow on top of the device is taken into account when solving the heat flow equation. Since we are working with ridge waveguide laser diodes, the air flow on top and around the sides of the ridge was considered. The simulations were in two dimensions. At the cost of a significant increase in execution time and required memory, the simulations can be extended to three dimensions.

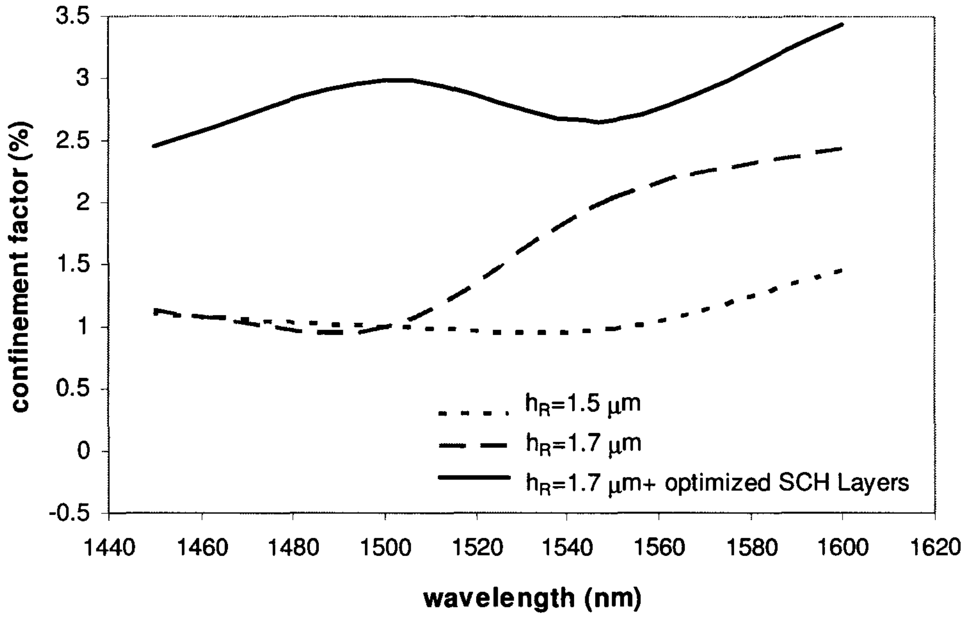

Figure 3.1: *Confinement factor optimization using BPM software. The dotted line is for wafer 4261 structure. The dashed line is for wafer 4261structure after optimizing the ridge height (h_R). The solid line is for the wafer 4261structure after optimizing both the ridge height (h_R) and the SCH layers.*

Before starting any of the simulations I did an optical confinement factor optimization using beam propagation method software (BPM). It turned out that the optical mode was not centered at the center of the active region for wafer 4261. Figure 3.1 shows the confinement factor results of this optimization study. The dotted line represents wafer 4261 before any optimization. I found that increasing the ridge height from 1.5 μm to 1.7 μm centers the optical mode on the active region represented in Figure 3.1 with the dashed line. The confinement factor improved for wavelengths between 1500 to 1600 nm only. After improving the SCH layers together with the ridge height this improvement was extended to about 1450 nm represented by the solid line in Figure 3.1. All results now will use the optimized confinement factor, represented by the solid line in the figure. See Section 1 of Chapter 4 for the experimental results of this optimization.

3.1. Ridge waveguide laser diode simulations:

The layer structure of the ridge waveguide laser diode used in the simulations is shown schematically and not to scale in Figure 3.2. The figure shows the AMQW layers as one average active region and the thicknesses of the layers used in the simulation. The contact layer is a heavily p-doped layer (1×10^{19} cm^{-3}). It turned out that using a continuous function for the doping profile helps to reduce the time taken to converge. A continuous function is probably closer to the physical situation, where diffusion and growth dynamics will smooth the transitions. Thus Fermi-Dirac functions were chosen to model the doping profile. The functions used in the simulations are as follows:

$$N_{\phi} = \frac{t_{\phi}}{1 + e^{\frac{(y_{\phi} - i_{\phi})}{S_{\phi}}}} + b_{\phi} \qquad \text{Eq. 3.1}$$

where t and b are the upper and lower limits of the doping profile, y is the growth direction as shown in Figure 3.2, i is the interface position in the y direction where the doping switches from the upper to the lower value, S is the slope of the transition region, and b represents a constant doping level. The subscript ϕ represents either the donor or acceptor variable value.

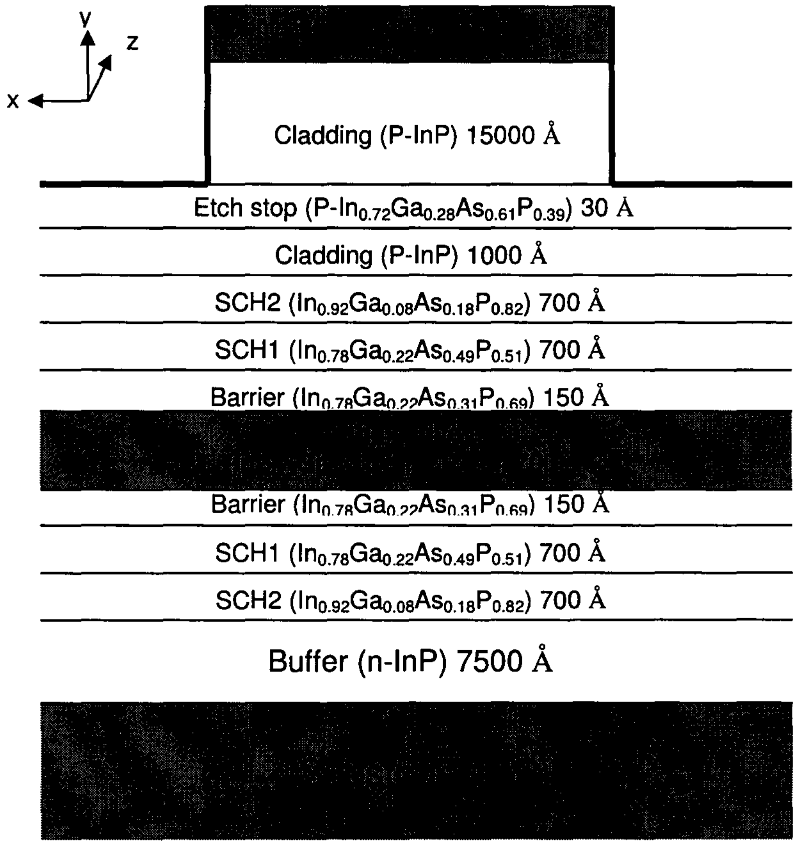

Figure 3.2: *The layer structure of the ridge waveguide laser diode (wafer 4261) used in the simulations. The active region is represented by single average layer. The y - direction is the growth direction.*

Plots of the band edges and quasi-Fermi levels of this laser from the simulation are shown in Figure 3.3 at different bias voltages. A built-in voltage of about ~1.3 V is shown for this laser at 0 V bias.

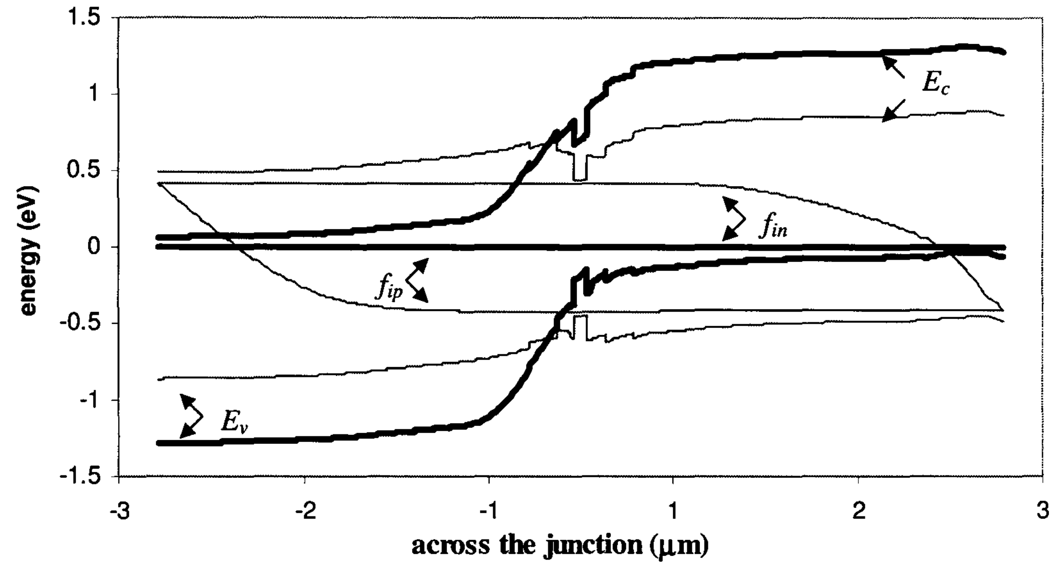

Figure 3.3: *Plots of the band edges and quasi Fermi levels from simulation of laser 4261 at bias voltages 0 volt (thick lines) and 0.84 volt (thin lines).*

The calculated current density versus applied voltage (J-V) curve for this laser (4261) is shown in Figure 3.4. The J-V curve shows that the current density is large at the top where the current injection starts and then goes lower in the center of the device (center of the active region) and then it is the lowest at the bottom of the device. This result tells us that the current is spreading as the current travels from the p-contact to the n-contact.

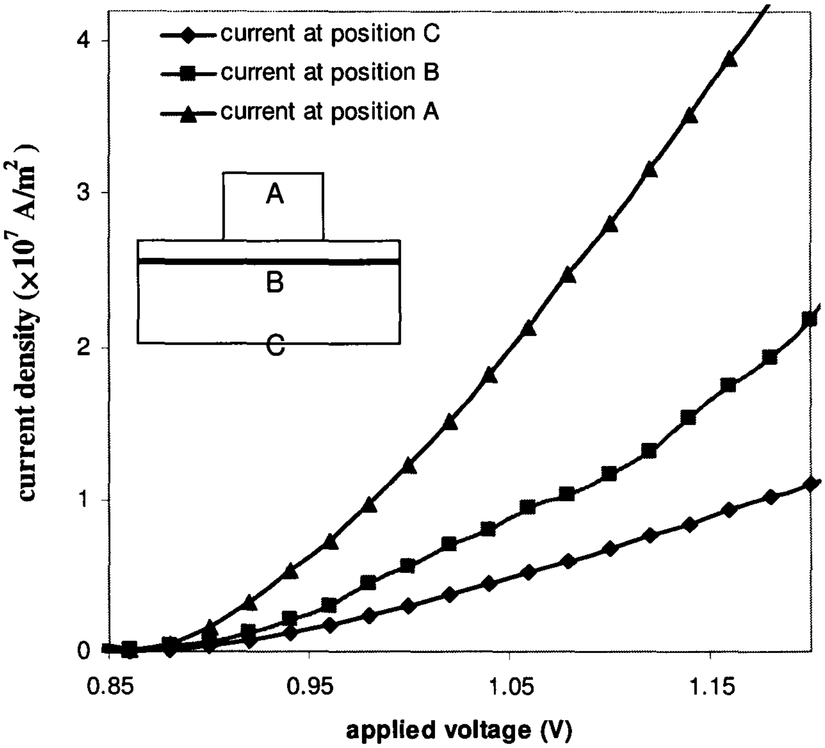

Figure 3.4: *J-V curves of a laser from structure 4261 from the simulation data near the top of the laser (A), at the center of the active region (B), and near the bottom of the laser (C).*

A two dimensional current density plot might help to understand how the current moves through the ridge area and it might shed some light on the change in current density presented in the previous figure. Figure 3.5 shows two dimensional simulation results of the current density over a cross section of ridge waveguide laser diode from structure 4261.

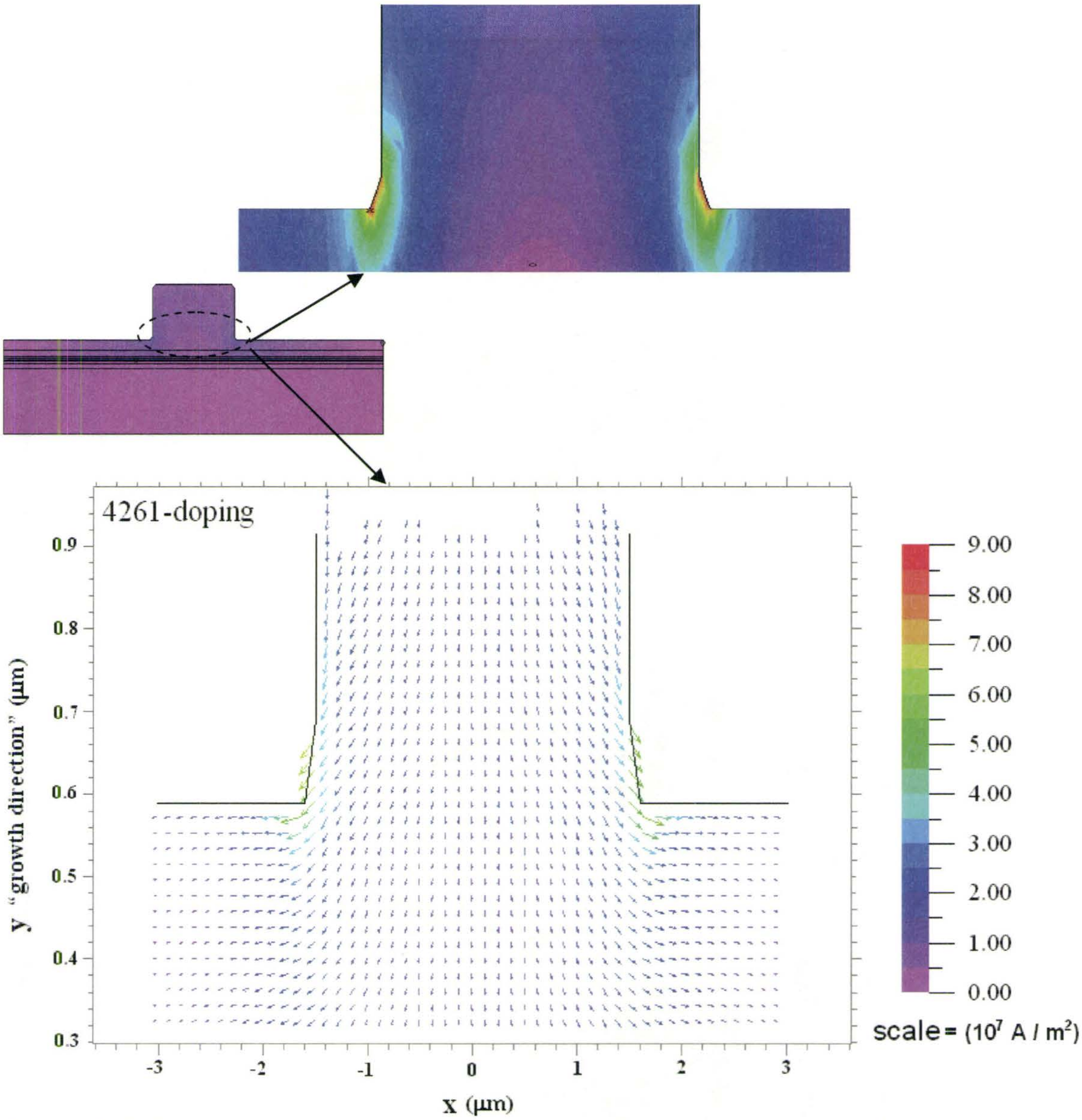

Figure 3.5: *Two dimensional simulation results of the current density of ridge waveguide laser from structure 4261. A zoomed contour (top), a vector (bottom) plot, and a whole device (center) plot are shown. The 2D vector plot shows that carriers leak around the ridge area away from the centre of the active region leaving the center area with a low current density. The length (or colour) of the arrow represent the magnitude of the current density.*

The current density contour plot (top) shows that the current density is concentrated around the bottom corners of the ridge far from the center of the ridge. The current density vector plot – the bottom plot in Figure 3.5 – gives a clearer picture of the direction of carrier movement inside the ridge area and just above the active region. This plot shows that the carriers leak around the ridge corners leaving the center of the active region deprived of carriers. This phenomenon happens because of the singularity of the electric field around narrow edges[59]. It is well known that the electric field is enhanced around so called sharp corners of a conductor or conductor-insulator interface[60]. As a result the current density will be significantly higher around the edges than in the middle of the ridge[61]. The current vector plot shows clearly poor current injection efficiency to the center of the device close to the active area. It is safe to say that the main reason for this current non-uniformity is the ridge structure.

Figure 3.6 shows the simulated two dimensional temperature profile of laser 4261 at an active region injected current density of ~ 1.17×10^7 A/m^2. The bottom temperature of the device was fixed at 16℃ to simulate operation. The figure shows that using cooling at the bottom helps to cool the device and that the area from the center of the active region to the top of the ridge endures the highest temperature. The figure also shows that the current that leaks around the ridge contributes to heating of the device. These results stimulated me to find the current injection efficiency of this laser. I found from the simulations that the current injection efficiency for 4261devices is around 17 %. I calculated the current injection efficiency as the ratio between the current injected to the active region under the ridge and the current injected across the whole device active region.

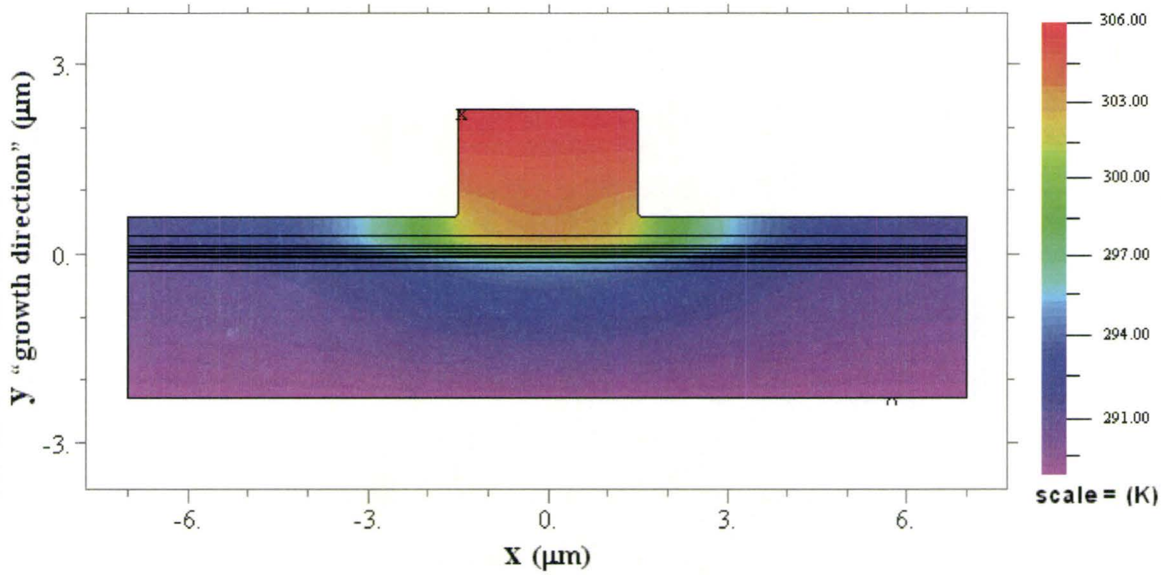

Figure 3.6: *Two dimensional temperature profile for a laser from structure 4261. The bottom temperature was fixed at 16°C. The leakage current around the ridge contributed to heating the device.*

Figure 3.7 shows the current injection efficiency from the simulation. The figure shows that the current injection efficiency starts at 27% at very low currents and then decreases very quickly to ~18% as the current increases. This result indicates that almost 82% of the current injected to the laser diode leaks away and participates in heating the device and increasing the device current threshold. This result is a very important result because it gives some explanation on the power problem of this type of laser that was presented in Chapter 1 and was central to my thesis research.

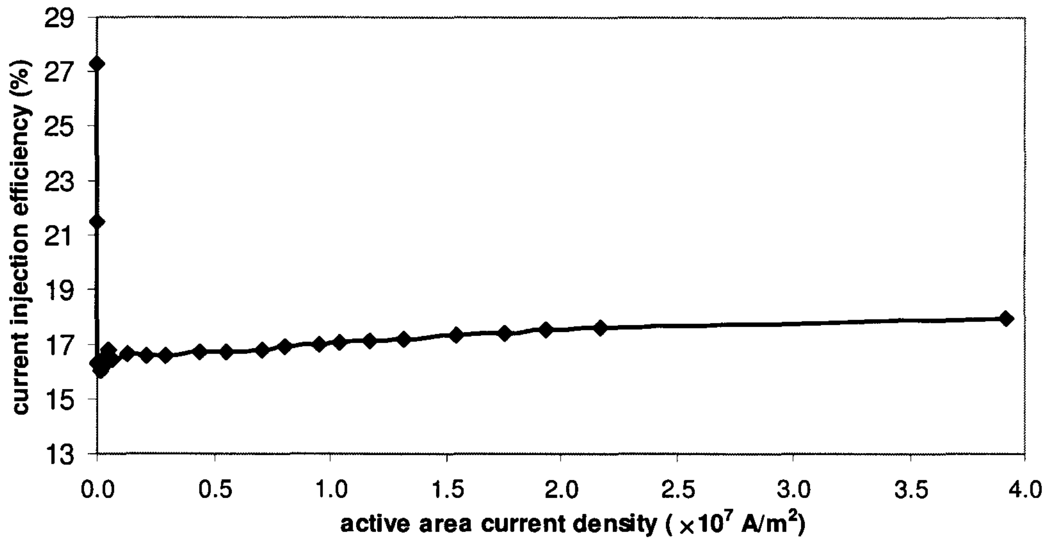

Figure 3.7: *Calculated current injection efficiency for a laser from structure 4261 at different active region currents.*

Since it is well known that the optical output power is almost linearly proportional to the injection current after subtracting the threshold current up to certain injection levels[62], it is safe to relate part of the AMQW ridge waveguide laser power problem to the poor injection efficiency of the ridge waveguide laser. I used the words "part of the problem" because the other part can be related to non-radiatve Auger recombination[63,64,65,66], and intervalence band absorption[67,68]. In more general terms, the other part of the AMQW ridge waveguide laser power problem can be related to hetero-structure leakage[69,70], barrier carrier interaction[71,72,73] and the nature of the multiple quantum wells[74,75]. Sweeney *et al.*[64] attributed 80 % of threshold current to non-radiatve Auger recombination. Since I am interested in keeping the broad tuning range of this laser the current injection efficiency was optimized without changing the design of the active area. The doping profile was optimized as first step then the ridge waveguide electrical confinement was optimized as a second step in an effort to reduce the effect of high leakage current at the corners.

I focused on current injection efficiency as the parameter to be optimized because, as can be observed from Figure 3.5 – Figure 3.7, that there is no meaning to optimize the J-V curve when there is no measure of how much of that current is injected to the active region.

3.2. Doping profile optimization:

The effect of the doping profile on laser diode performance shows a great deal of confusion in the literature. Mixed reports have been published about extending or shortening[71-76,78] the doping profile in or away from the SCH and active area. Seki *et al*[77] reported that the deterioration of laser power at higher temperatures is due to the increase of internal losses because of the pileup of carriers in the SCH layer. Piprek *et. al.* intentionally un-doped not only the SCH layer but part of the cladding layer to reduce absorption losses[78]. They claimed that the interaction between the optical field and the p-type carriers are responsible for the increase of internal losses. Another report claimed that p-doping of the QW region is ineffective for speeding up the inter-well carrier transport[79]. Heo *et al.*[80] proposed an asymmetric SCH layer to shift the optical field away from the highly doped p-SCH layer. On the other hand experimental data reported by Belenky[76,81] showed that moderately doped p-cladding and SCH layers improved the threshold current, the efficiency, and the leakage current over un-doped SCH layers when running the devices between 20 and 80 °C. The thickness of the SCH layer of Belenky was nearly a quarter of the thickness of the SCH layer for lasers from structure 4261, yet he recommended moderately doping up to the active area where he had Zn concentration around 10^{17} cm^{-3} at the SCH/active region interface. In other words Belenky believes that extending the doping to the SCH helps improve the laser performance.

Another paper reported confusing results in the same paper[82]. The authors claimed that the threshold current density almost doubled when increasing the p-doping level in the cladding layer from 4×10^{17} to 6.5×10^{18} cm^{-3} and introducing a setback layer, while it claimed that efficiency and thermal performance improved significantly with that process.

The theme of laser designers and laser growers appears to be to keep dopants away from the optical mode; designers appear to believe that this reduces the losses by reducing the interaction between the p-carriers and the optical field [71,76,77].

Delta doping[83] is another technique used in doping laser diodes. Reports showed that Si delta doping of barriers of III-V materials improved dramatically the PL intensity[84] and dark current[85]. Different authors reported that delta doping the heterostructure interface and moderately doping the SCH improved the light output and the thermal performance of laser diodes [80-86]. These delta doping reports contradict what designers are doing to keep dopants away from optical field, which adds more controversy to the doping issue. Furthermore, Hatori *et. al* [87] showed that delta p-doping of all the barriers in the quantum wells reduced the threshold current and carrier life time. In the coming section I present some simulation results of delta doping to investigate the effects of delta doping on laser performance. However the delta doping was limited to the SCH layer since some designers fear the interaction between the carriers and the optical field.

From what I found in the literature so far I can not favor extending or limiting the doping profile to the SCH layers. This issue needs to be further investigated. The purpose of this section is, first, to simulate different doping profiles and to find out through simulation if limiting or extending the doping to the SCH layer will improve the performance of the AWQW laser diodes that have been developed in the research group that I joined to perform my Ph.D. research. Second is to find out if delta doping helps to improve AMQW laser diode performance. An examination of the effect of the interaction between the optical field and the p-type carriers –the theme of many laser designers and growers– will be left to the experimental work, Chapter 4, since my simulations do not include a solution of the optical modes.

3.2.1. Optimized cutoff of doping profile:

In the previous section I talked about the confusion found in the literature in adopting certain doping profiles. In this section, the performance of three doping profiles was compared. Three doping profiles are used in the simulations: one profile represents the doping profile in wafer 4261 (type 1); the second profile is an optimized profile, where the doping was extended past the SCH layers up to the interfaces with the first barriers (type 2); and, the last profile has the dopants reset back in the cladding layer (type 3). Figure 3.8 show plots of these three doping profiles. The J-V curves for these three structures are shown in Figure 3.9. The curves on the right hand side show near the top of ridge current density and the curves on the left hand side show the current density at the center of the active region. Figure 3.9 clearly shows that the current density is improved by type 2 doping profile for both near the top and center of active regions. Yet, the J-V curves for the current density do not give clear indications of the improvement of the current injection efficiency to the active region. Figure 3.10 shows the two dimensional vector and contour plots of the current density for all three doping profile types at equal injected current densities of $J_0 = 2.2\times10^7$ A/m^2 at the active region.

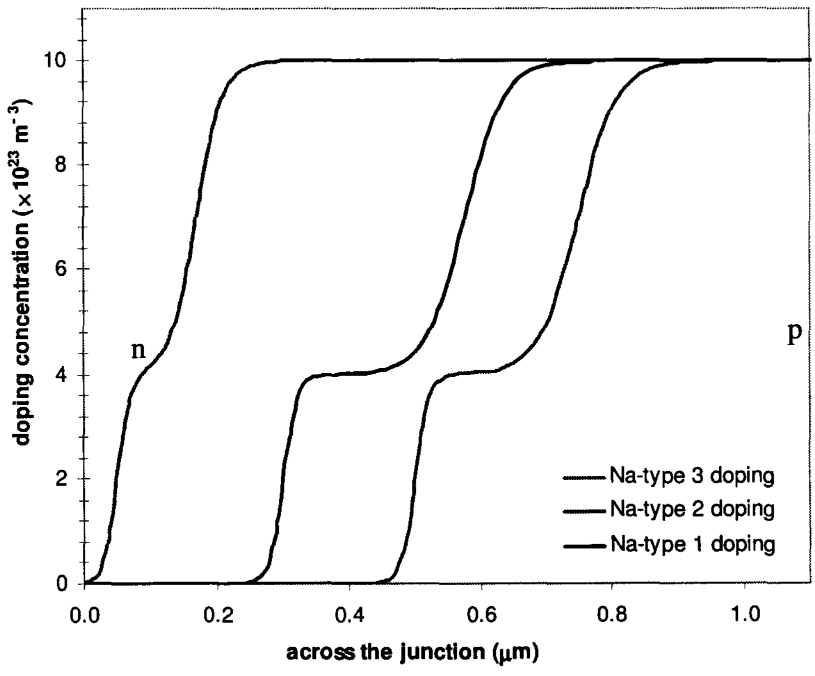

Figure 3.8: *Doping profile for the three structures used in the simulation. Acceptor concentration is shown for the three types. The donor concentration is a mirror image of this plot.*

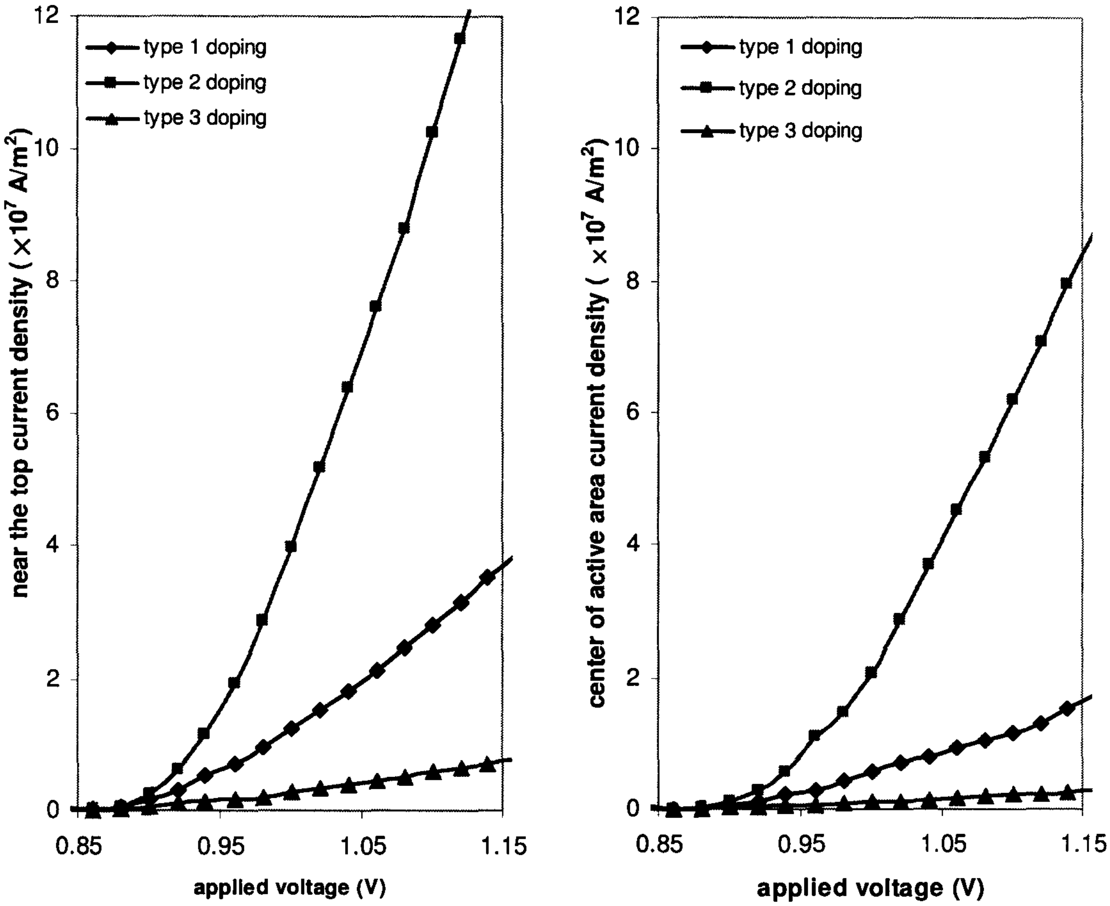

Figure 3.9: *J-V curves for three doping profiles. The diamond marked line represents wafer 4261. Near the top current density for the p-contact is shown on the left hand side and the active region current density is shown on the right hand side.*

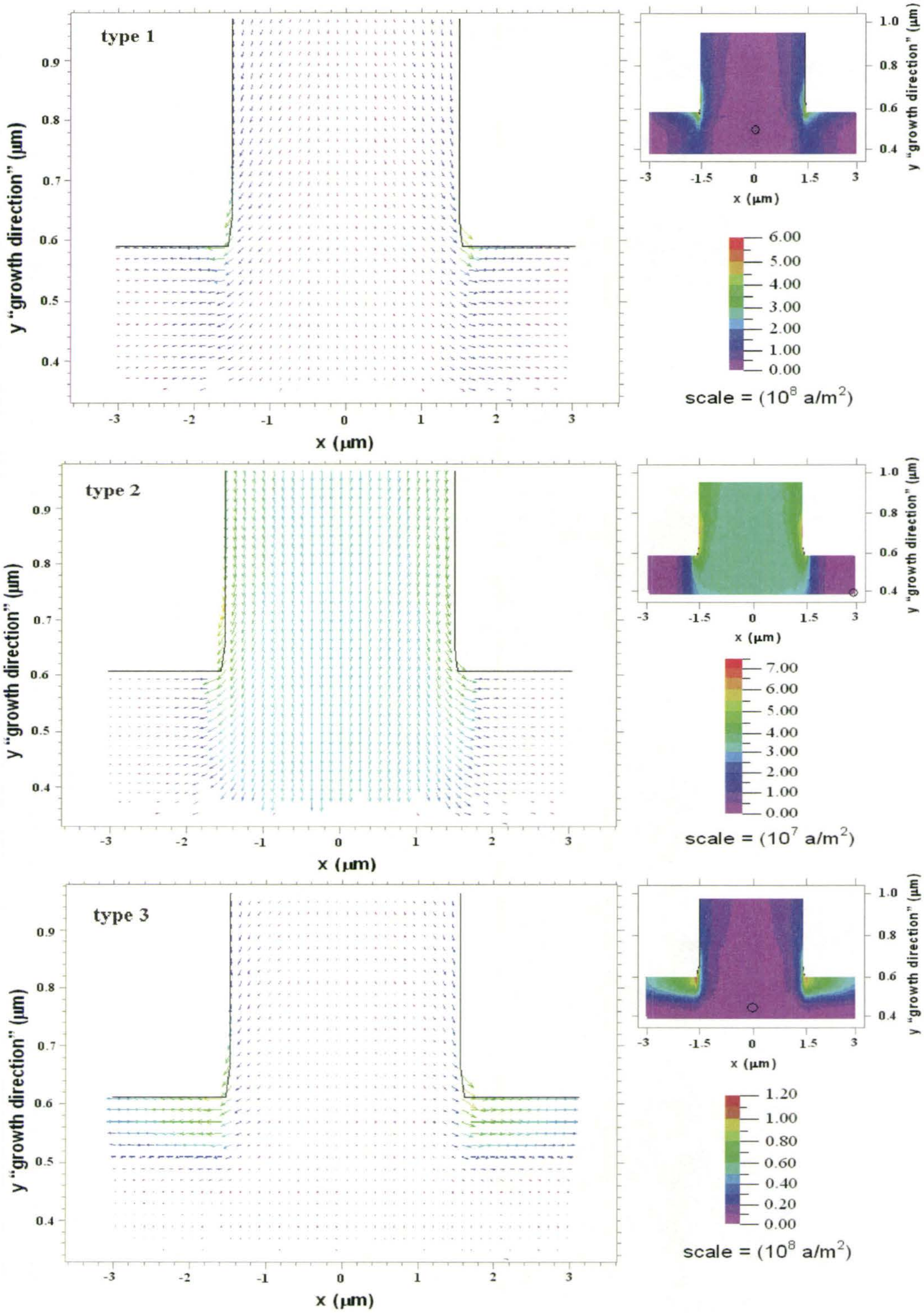

Figure 3.10: *Two dimensional vector and contour plots of the current density for the three doping types at equal current density injection to the active region.*

The vector plots for type 1 and type 3 show a strong lateral current from the center of the device towards the walls of the ridge. This lateral current is more severe in the type 3 doping profile than in the type 1 doping profile. Lasers from wafer 4261 are of the type 1 doping profile. The optimized doping profile, type 2, shows significant improvement in current injection to the active area. The type 2 vector plot in Figure 3.10 shows reduction of the leakage in lateral current from the center to the edges. This reduction of the lateral current density improves the uniformity of the current density in the active region. Because of the via type injection and ridge configuration in RWG lasers, there always will be current leakage at the bottom corners of the ridge. The purpose of the simulations in this chapter is to reduce this leakage as much as possible.

Another look at Figure 3.10 reveals that in type 1 and type 3 doping profiles, the smallest current density point is at the center of the ridge just slightly above the active area. This point is identified by a small circle in the contour plots. For the optimized doping profile, type 2, the smallest current density is away from the ridge centre and far from the active area at the right bottom corner of the laser. The trend that is obtained from Figure 3.10 is that the closer the doping is to the QW, the more uniform the flow of current and the less lateral current there is. Significant improvement of current injection to the active region is achieved by extending the doping closer to the QW.

The current injection efficiency from the simulations for all three doping profiles was calculated. Figure 3.11 show the current injection efficiency for the three doping profiles. The figure shows a significant improvement of the current injection efficiency of the optimized doping profile (type 2) over the doping profile of 4261 (type 1), and type 3. This result confirms the current density improvement shown in Figure 3.10.

Now, the question is how this current injection improvement affects the temperature profile and will this improvement reduce the device temperature while maintaining the same injection level to the active area?

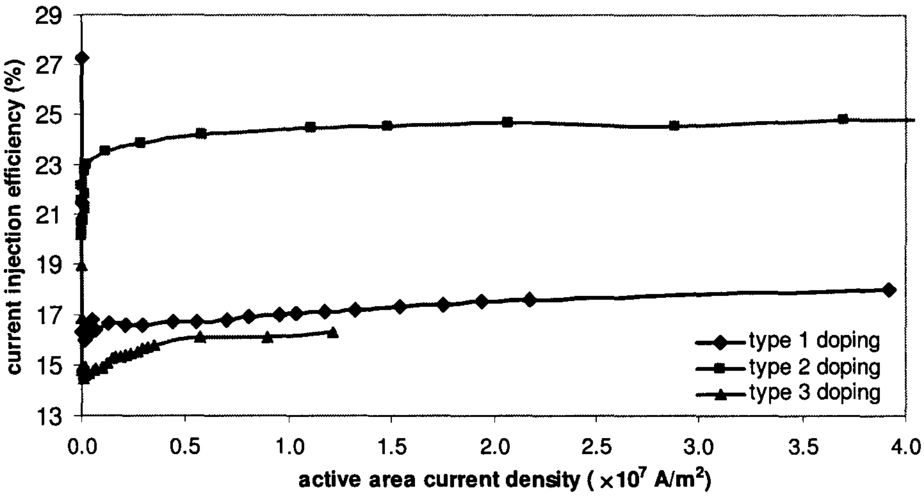

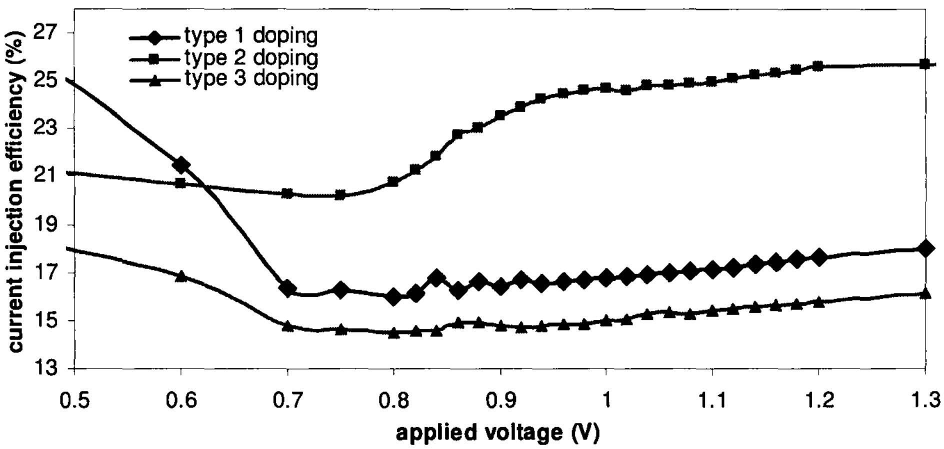

Figure 3.11: *Current injection efficiency for the three doping profiles as function of active area current density (top) and applied voltage (bottom).*

Figure 3.12 shows two dimensional contour solutions to the temperature profile for both type 1 and type 2 profiles. The figure shows a maximum temperature of 306 K for a type 1 doping profile while the optimized doping profile, type 2, shows a maximum temperature of 300.4 K for the same current density injected to the active area.

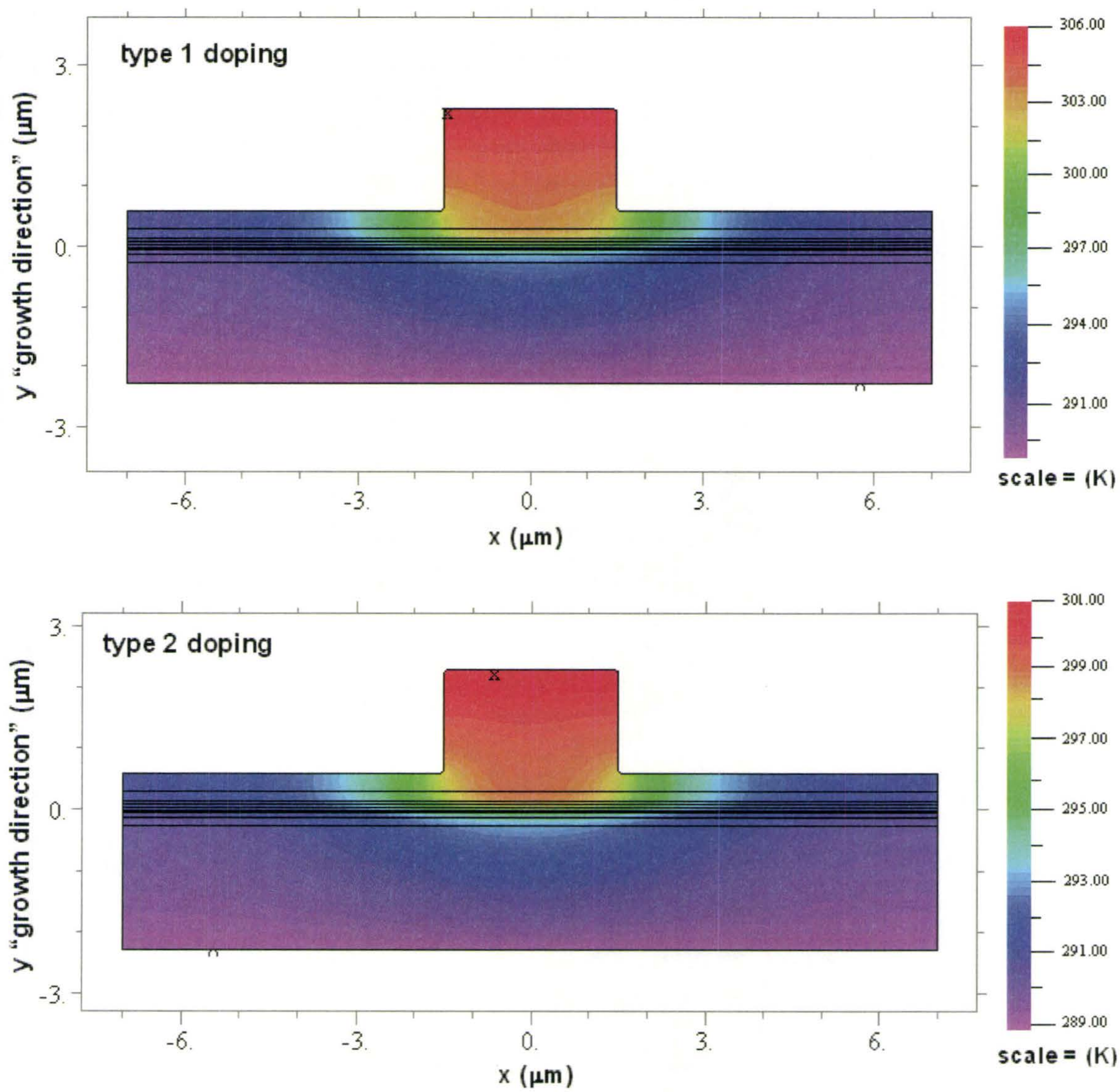

Figure 3.12: *Two dimensional temperature distribution for type 1 and type 2 doping profiles at the same active region current density level of* 1.17×10^{7} *A/m*^{2}.

The maximum laser temperature as a function of injected current density is shown in Figure 3.13. The figure shows that the maximum laser diode temperature for a type 2 doping profile is lower when more current is injected into the active region in comparison with type 1 and type 3 doping profiles. In a low current regime it seems that there is no significant difference between the three types. This can be explained from Figure 3.11. If the current injection efficiency for the three types is almost identical then one can expect no thermal advantage for any of the doping profiles.

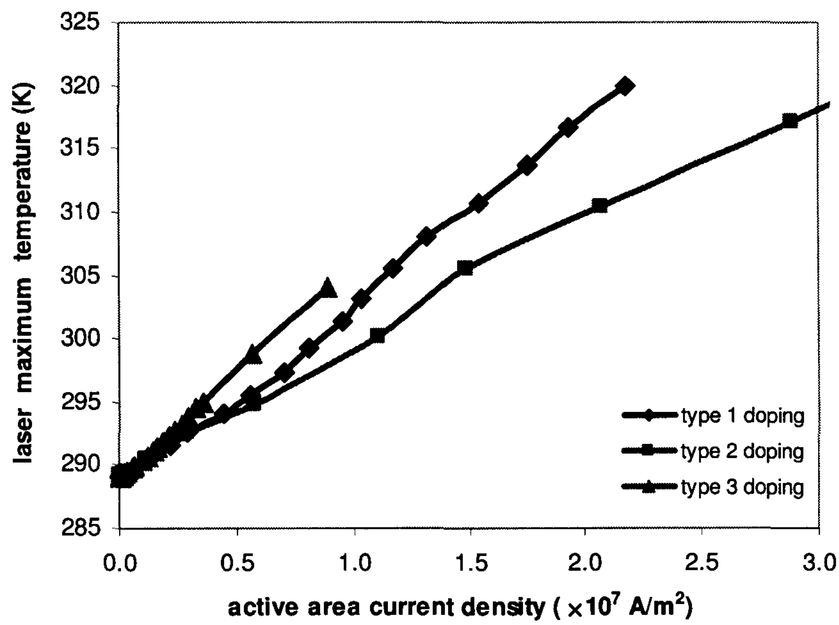

Figure 3.13: *Maximum laser diode temperature as a function of active region current density. Type 2 has the lowest maximum temperature compared to types 1 and 3 at high current levels.*

Extending the doping profile to the SCH layers will reduce the width of the space charge layer of the p-n junction in the active region of a laser diode. Reducing the width of the space charge layer reduces the resistance to the carriers that are injected to the active region. This can explain part of the improvement in electrical and thermal performance of the optimized profile, type 2, over the original profile, type 1.

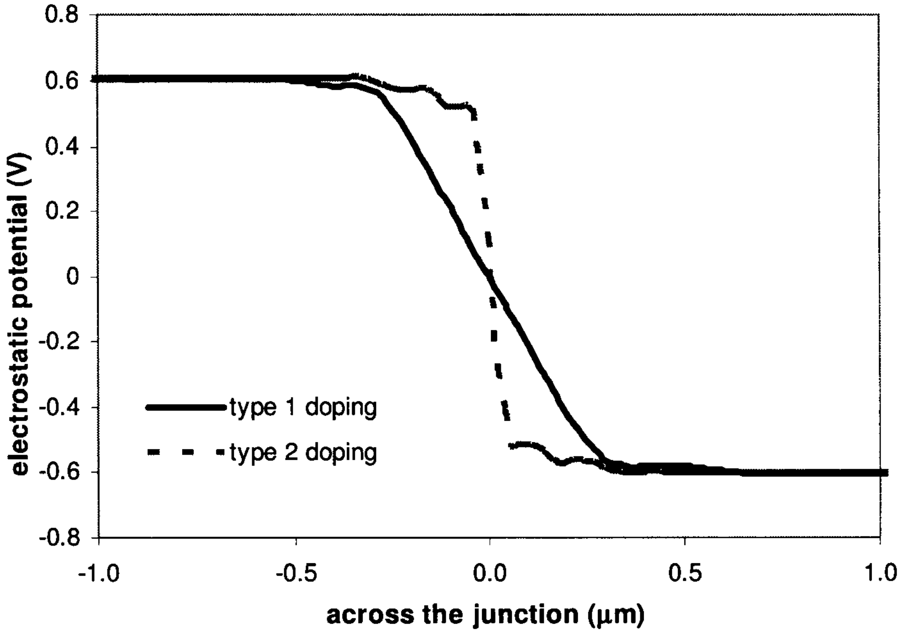

Figure 3.14: *Electrostatic potential for type 1 and type 2 doping profiles. Type 2 has a reduced width of the space charge layer as compared with type 1.*

Extending the doping profile also helps in reducing the lateral current leakage as shown in the previous section. The lateral current leakage seems to be partially controlled by the thicknesses of the cladding and the SCH layers under the ridge. Unfortunately these layers are optimized for optical confinement only and they are not necessarily optimized for electrical confinement. It may seem logical that thinning these layers would increase the current passing through the active area under the ridge. However, doing this will reduce the optical confinement; see Section 1 in Chapter 4. From the simulation results earlier it seems that extending the doping profile helps inject more current to the active region under the ridge even if the active region is buried under 0.25 μm thick cladding and SCH layers. In other words, optimizing the doping profile reduces the electronic problems caused by optimizing the optical confinement in the RWG diode lasers. In the next chapter the output power of a wafer with an extended doping profile is compared with the output power of wafer 4261. If the output power is more in the new wafer that will confirm the simulation results. If the power is lower, then the losses from the overlapping between the carriers and the optical field is stronger than the improvement in the output power because of the optimized doping profile.

3.2.2. Delta doping profile:

As discussed earlier, some publications[85, 79] showed that delta doping is thought to improve the performance of MQW ridge waveguide laser diodes by reducing the lateral leakage current. In this section I report on a simple doping profile with and without delta doping to demonstrate the effect of the delta doping on my laser diode structure. The doping profile is shown in Figure 3.15 where the solid line is a simple doping profile and the dashed line is the same doping profile with a delta function added. For comparison to the literature, I tried to maintain the doping at 3.5×10^{24} m^{-3} as in reference [85]. The J-V curve for these doping profiles is shown in Figure 3.16 at three different points – top (A), active region (B), and bottom (C) – on the device. The figure show a slight improvement in the J-V curves for the profile with delta doping over the profile without the delta doping.

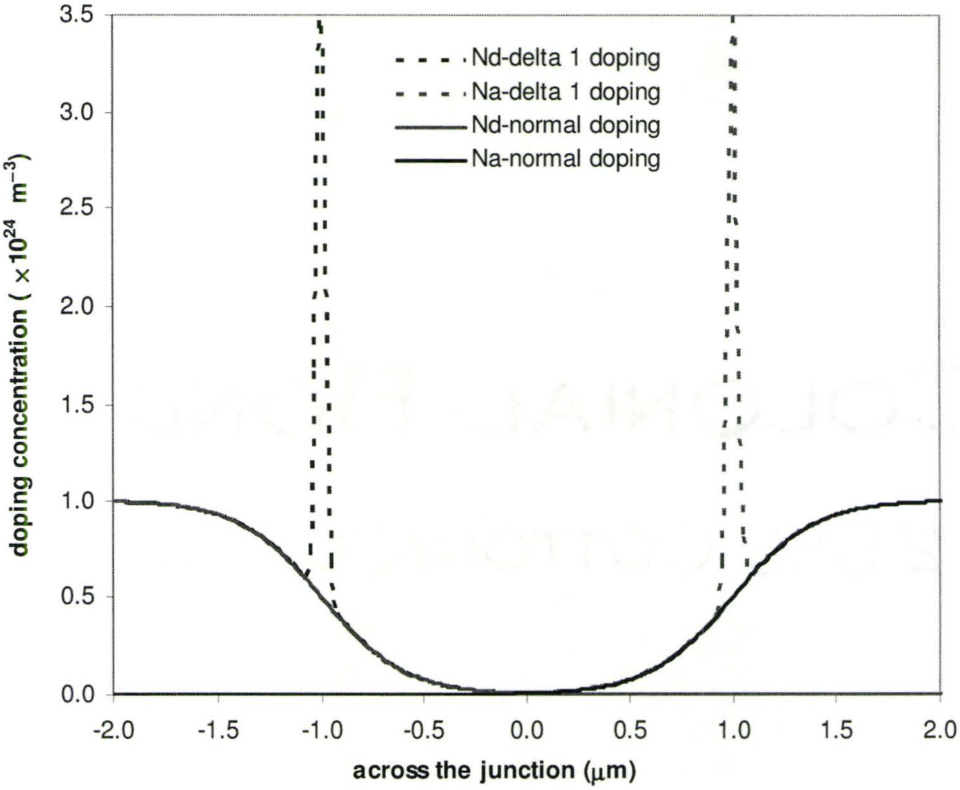

Figure 3.15: *Delta doping profile and the normal doping profile (simple doping profile) for comparison. A level of* $3.5\times10^{24}\ m^{-3}$ *is maintained for the delta doping as in [85].*

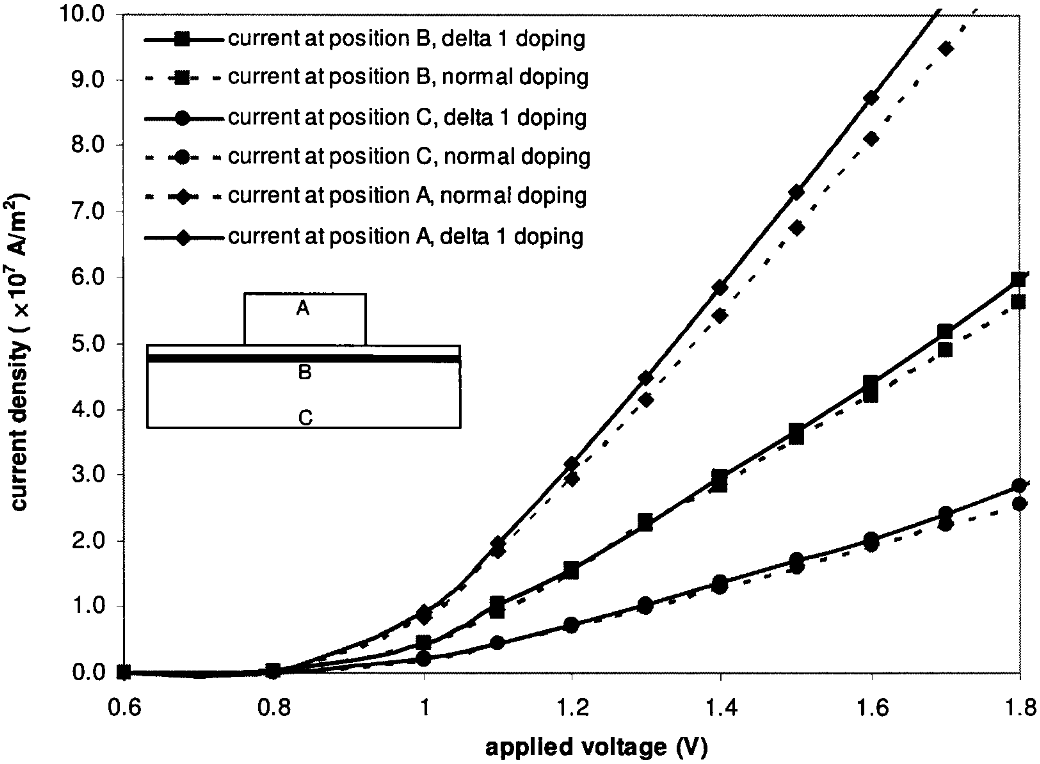

Figure 3.16: *J-V curve for the doping profiles with and without delta doping. A slight improvement can be seen in the J-V curve of the delta doping (solid lines) over the profile with no delta doping normal profile (dashed lines).*

There was no significant improvement in the current injection efficiency of the profile with delta doping over the base profile without delta doping. Now, one can question the slight improvement in the J-V curve: was the improvement because of the delta doping, or was the improvement because of the slight extension in the doping profile towards the active region as a result of the delta doping?

To answer this question a second doping profile (delta 2, shown in Figure 3.17) was simulated, which is close to the delta doping shown in Figure 3.15. In this new profile, the height of the delta doping was increased to 1×10^{25} m^{-3} level and the delta 2 doping profile was terminated much earlier than the base profile. If delta doping has any positive effects then one expects to see it more in this simulation than the previous one.

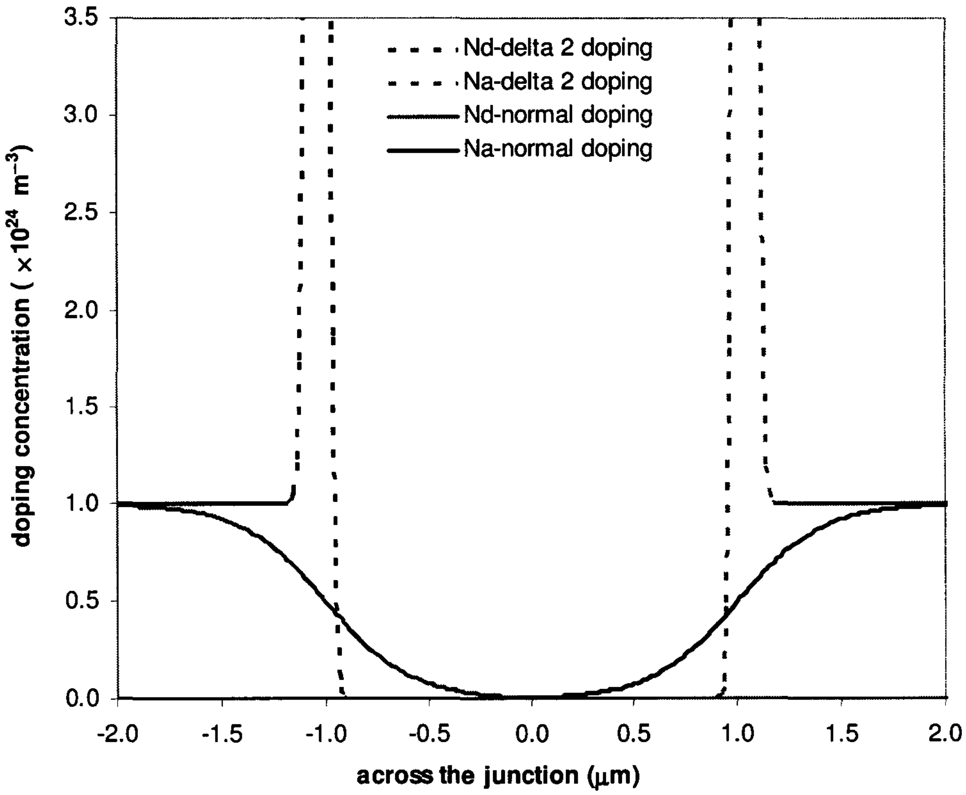

Figure 3.17: *Second delta doping profile (delta 2) where the doping is terminated earlier in the delta doping profile than in the normal doping and the delta doping spike was increased from 3.5×10^{24} m^{-3} to 1×10^{25} m^{-3}.*

Figure 3.18 show the J-V curves for the delta doping profile and the base profile. The figure shows very interesting results. The latest delta doping (delta 2) gives very poor J-V curves in comparison with the previous delta doping (delta 1) or the simple base doping profile. Figure 3.19 show vector plots of the current density for this new delta doping. The figures show that the delta doping acts like obstacles that divert the current flow more towards the ridge side walls. This result tells us that moderate delta doping does not help to improve the electrical performance of ridge waveguide diode lasers.

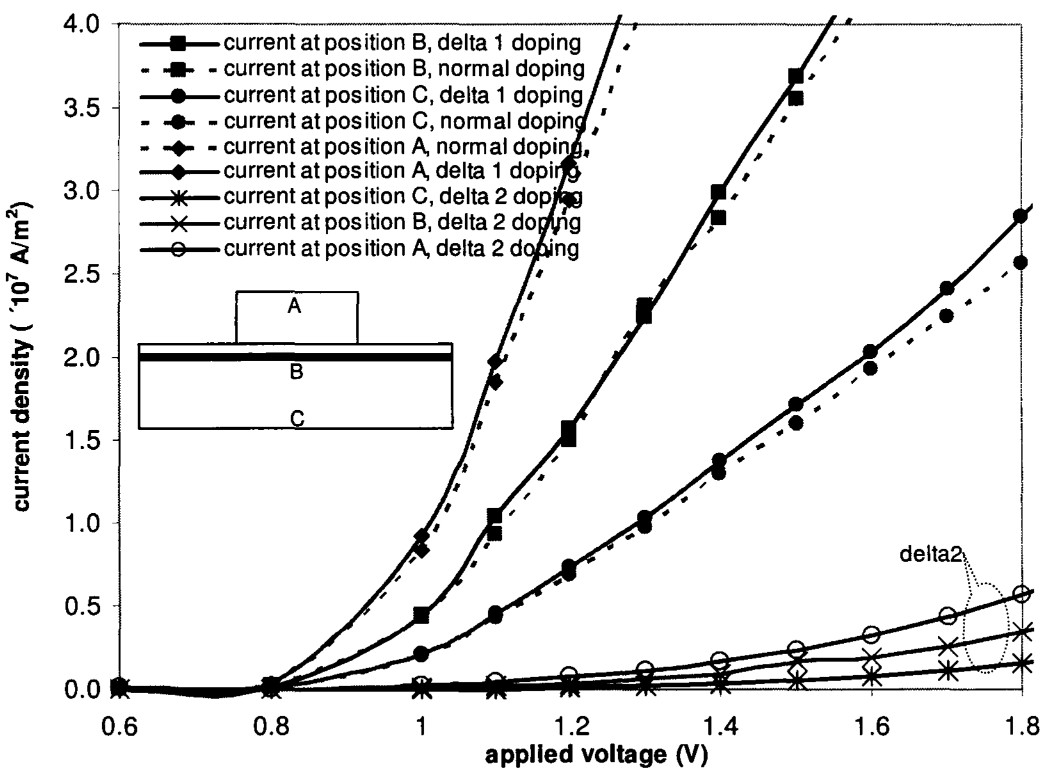

Figure 3.18: *J-V curves for both delta doping profiles and the normal doping profile. The low lines represent the latest delta doping (delta 2). The delta 2 doping profile gives poor J-V curves in comparison with the delta 1 doping profile.*

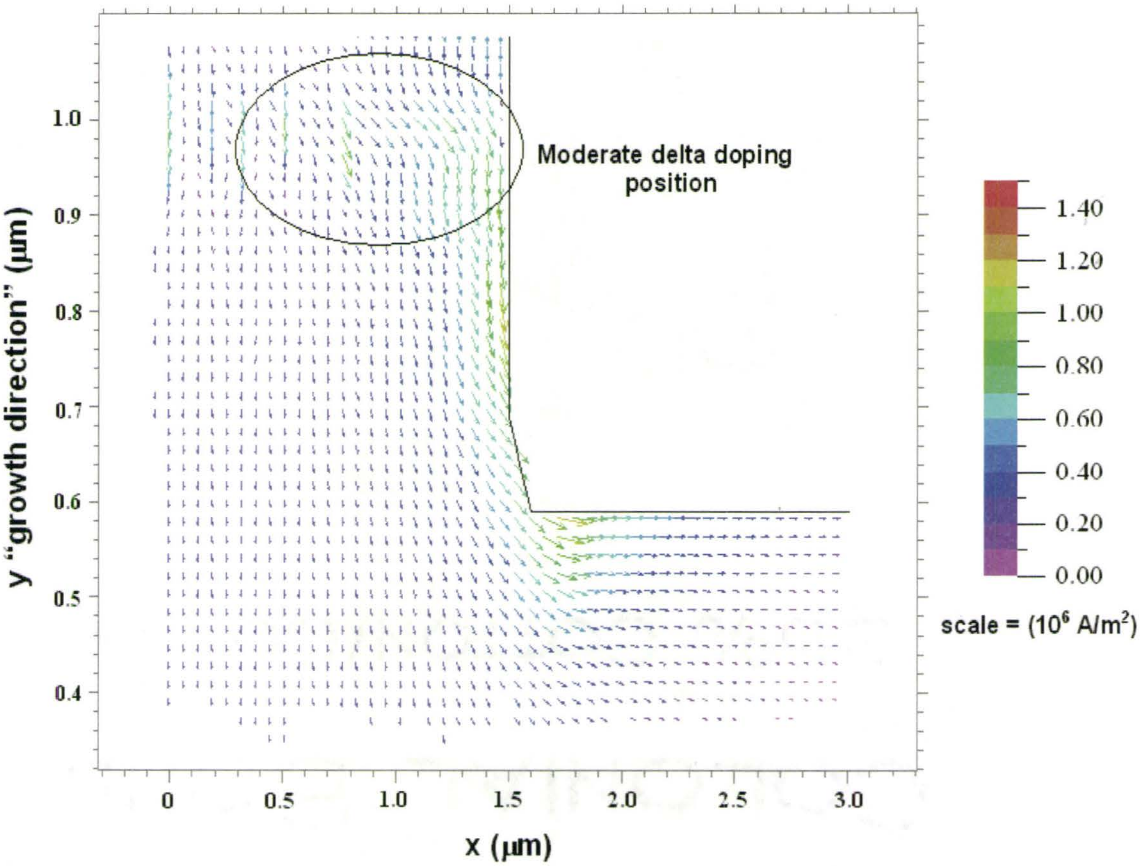

Figure 3.19: *Vector current density plot for a moderate delta doping profile. The circled area shows the effect of delta doping on the current density.*

To conclude this section it is safe to say that the moderate delta doping simulation did not show any significant improvement to the electrical performance of the ridge waveguide diode laser. Moderate delta doping did not help to reduce the leakage of carriers in the SCH layer or around the bottom of the ridge; on the contrary, moderate delta doping showed poor electrical performance in comparison with normal doping (i.e., with no delta spikes).

3.3. Forced electrical confinement simulations:

Ion implantation is used for making high resistive III-V materials[88]. Authors used ion implantation to improve the current confinement of lasers[89,90]. The damage as a result of ion bombardment can increase the resistivity of the III-V material ridge walls for example, which in turn can improve the electrical performance of ridge side walls and hence reduce the leakage current. It is reported that ion implantation at low temperature results in more stable damage formation[91]. One of the major problems of using this technique is generating stable defects. Generation of thermally stable defects can be quite difficult when dealing with laser diodes as lasers diodes generate heat continuously when operating. In this section I show simulations of another method that can be used to improve the current injected to the active region and to improve the over all laser performance.

3.3.1. Isolation etch method:

I called this method the isolation etch method (IEM). In the IEM trenches are etched around the ridge waveguide (see Figure 3.20). These trenches go through the active area to perform electrical isolation and in return force most of the carriers to go through the active region under the ridge. Figure 3.21 shows a two dimensional contour plot of the current density of 4261 devices with the isolation etch trenches. The figure shows that the current is blocked from spreading away from the active area; the current is forced through the active region. The figure also shows a small spreading of the current below the isolation etch trenches. However, the amount of current is not significant and should not affect the performance of the device since almost all the current passes through the active region. The calculated injection efficiency for this device was between 90 - 92%, which is a very high efficiency.

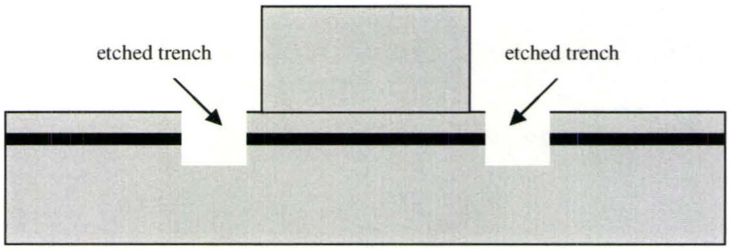

Figure 3.20: *Isolation etch method (IEM) where trenches are etched around the ridge area to force electrical confinement.*

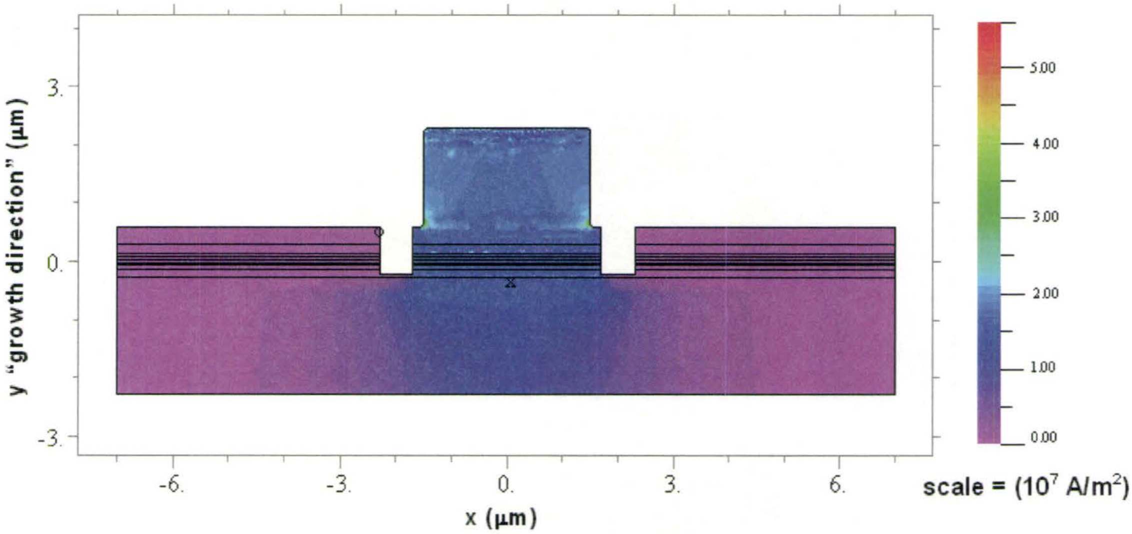

Figure 3.21: *Two dimensional contour plot of the current density for an isolation etched device.*

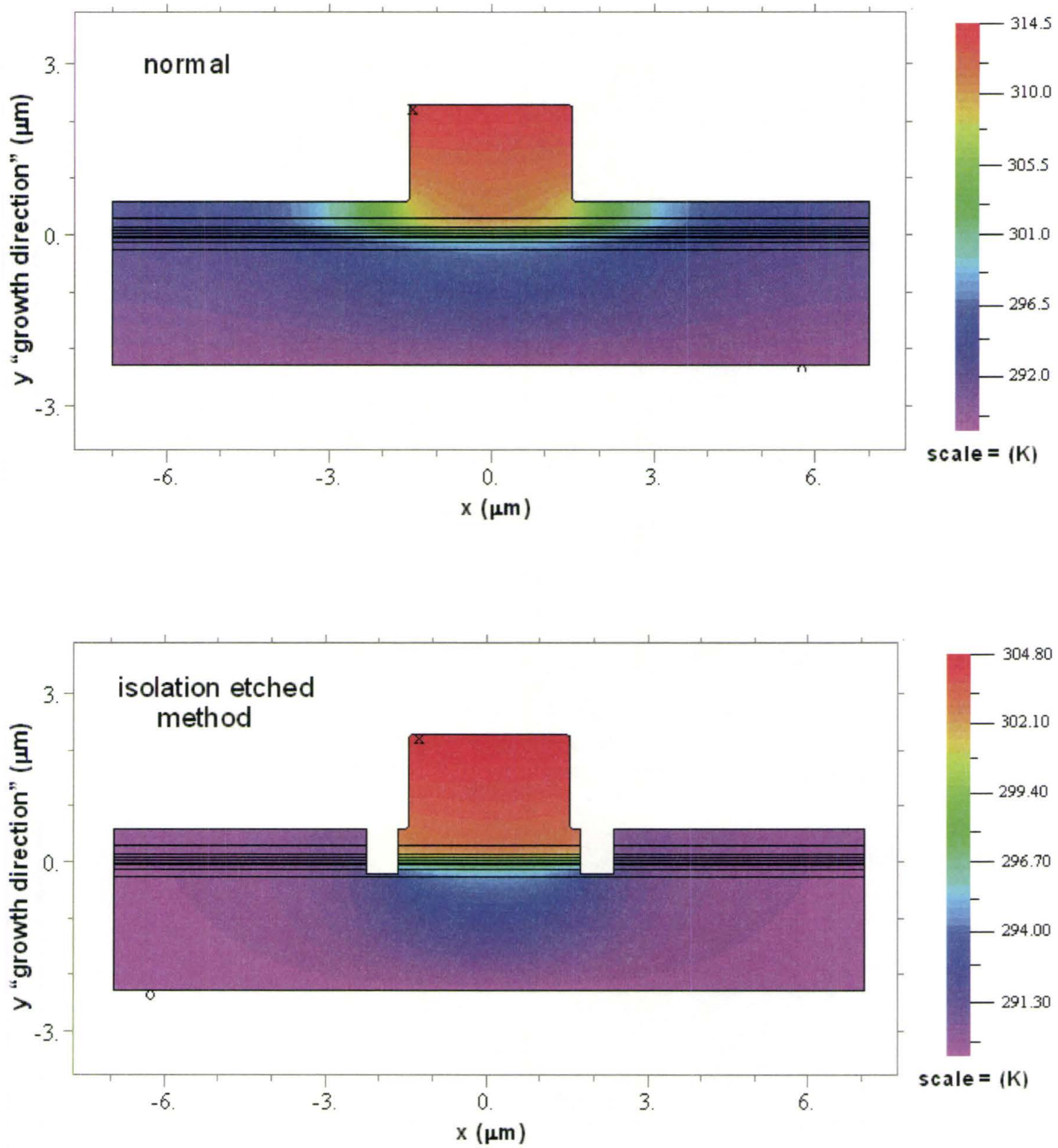

Figure 3.22: *Two dimensional temperature profile of normal device wafer 4261and an IEM device at the same active area current density of 1.7×10^7 A/m^2. An improvement of ~10 °C is achieved in the temperature profile using the IEM method.*

Figure 3.22 shows temperature profiles of the original laser (4261) together with the IEM device for the same injected active region current density. The figure shows a reduction of nearly 10 °C in the maximum temperature for the IEM devices as a result of current injection efficiency improvement. This temperature improvement is significant and can lead to a significant improvement of the laser output power. As I experienced from experimental measurements –see Sec. 1, Chapter 4– and, according to Okamoto[92] *et al.* and Makino[93] *et al.*, a reduction of 10 °C of the operating temperature of the active region can double the output power of III-V MQW ridge waveguide laser diodes.

Despite that the IEM device has a very high current injection efficiency and significant temperature reduction; it suffers from recombination centers because of the defects from the native oxides that are introduced at the exposed quantum well edges. The solution to this problem depends on the quality of the cleaning process that can take place and the passivation layers that can be deposited on the exposed active region edges. I included the effects of these recombination centers in the model where I added recombination centers along the exposed active region edges. These recombination centers should create an increase in the threshold current and an increase in the device temperature. Figure 3.23 shows a temperature profile of a 4261 device with an isolation etch 1 μm away from the ridge walls. The figure show hot spots at the exposed active area as a result of strong recombination that is taking place because of the recombination centers (RC) introduced at these edges.

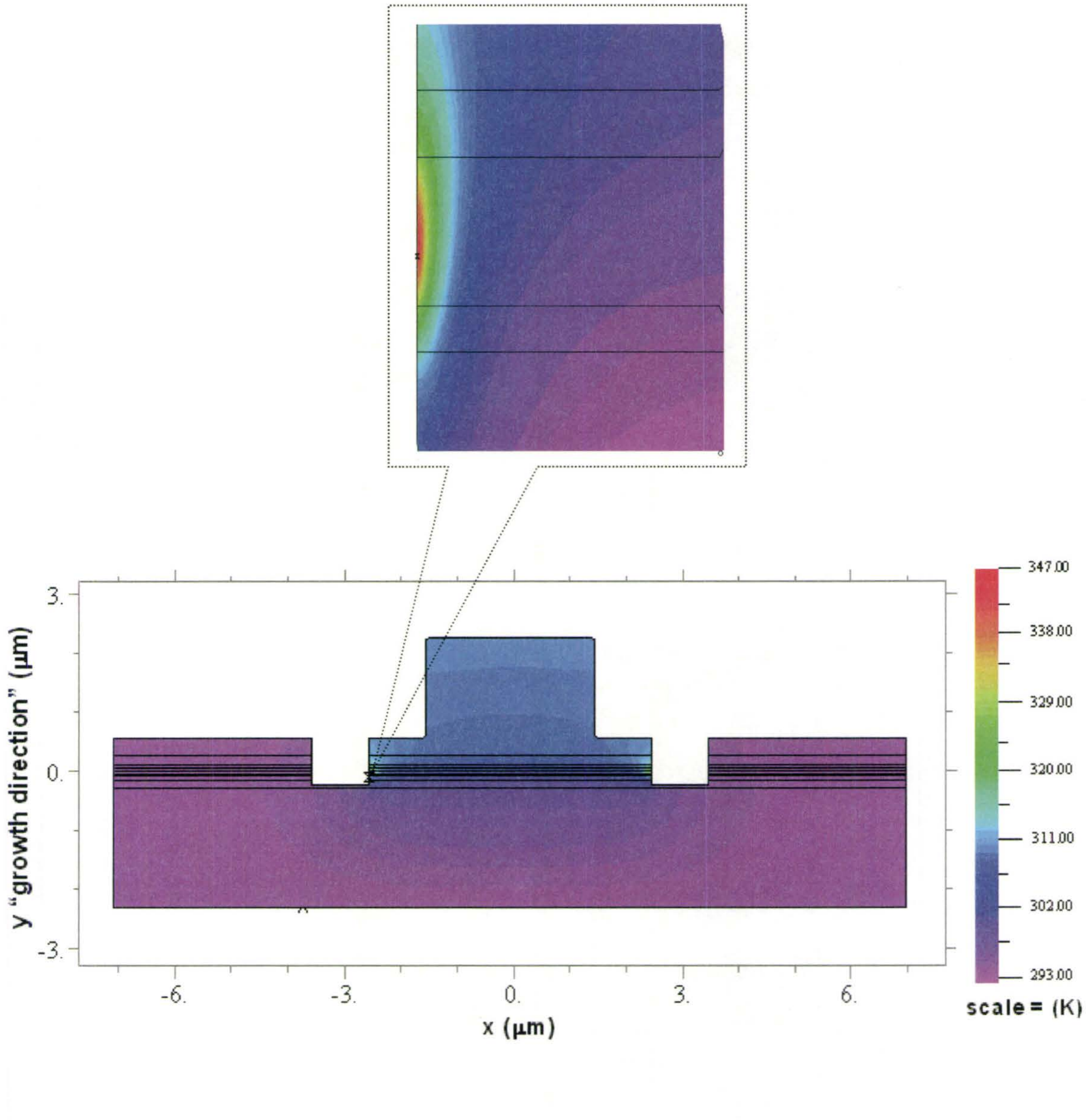

Figure 3.23: *Contour temperature profile of 4261 device with an isolation etch 1 μm away from the ridge walls. Notice the hot spots at the exposed active area as a result of a strong recombination process that takes place because of the recombination centers introduced at these edges.*

Figure 3.24 show the calculated J-V curves for this isolation etch with recombination centers (IEM-WRC) device compared with the original device 4261.

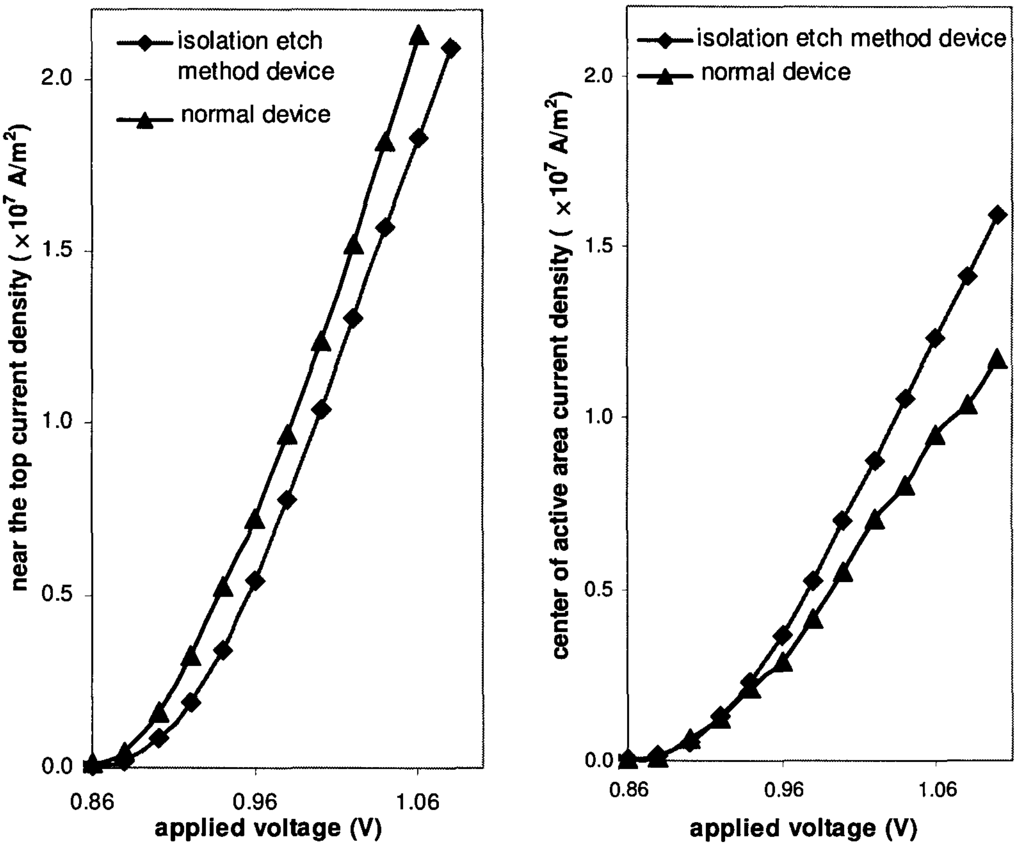

Figure 3.24: *J-V Curves for devices from structure 4261 in comparison with an isolation etched device (IEM) device with recombination centers (WRC) at the exposed active area. The increase of series resistance is responsible for the lower terminal current on the IEM device.*

The figure shows that the terminal current for the IEM device is worse than that of the 4261 device while the active region current density for the IEM device is improved over the 4261 device active region current density. The simple explanation to this interesting result is the following. Etching the trenches around the ridge increases the series resistance of the device and that is what we see in the top current curves. However, most of the IEM bias current goes through the active region as the efficiency is very high so the active region current must be better than that in the original device. In other words, the energy that is wasted by increasing the series resistance is much smaller than the energy that is saved by improving the injection efficiency. The current injection efficiency of these devices is considerably affected by the trench position relative to the ridge wall and also by the recombination centers at the exposed edges of the active area. For this device the current injection efficiency is in the 57 %, range which is still high compared with 17% for a 4261 device. In the next chapter (an experimental results chapter) I show how the trench position and the defects at the exposed active area affect the performance of AMQW laser diodes.

Chapter 4

AMQW Laser diode experimental results

In the previous chapter (Chapter 3) I tried to answer the main questions about the AMQW ridge waveguide laser output power problem. Laser diode simulation data was used to find out why the AMQW ridge waveguide laser has such low output power. The effect of doping profile on the current injection efficiency of the device was studied. Also, solutions to improve the current injection efficiency and consequently the laser output power while maintaining the broad tunable range were shown.

In this chapter the experimental results on AMQW ridge waveguide laser diodes are discussed. First, the experimental results from a new wafer, wafer 4381, which has an optimized confinement factor, are compared with an old wafer, wafer 4261. Second, the experimental results of a recent wafer, wafer 4693, which has an optimized doping profile, are compared with wafer 4261 and optimized confinement factor wafer 4381. Third, the effect of the laser transition cavity length (TCL) on the power output is studied. Finally, the results of the isolation etch method (IEM) for lasers fabricated from wafer 4693 are discussed.

4.1 Confinement factor optimization experimental results:

Earlier in Chapter 1, the output power problem of broadly tunable AMQW ridge waveguide laser diodes was discussed. Figure 4.1 shows the sensitivity of lasers from wafer 4261 to temperature. The figure shows the measured output power from a single facet of 900 μm long, 3 μm ridge width, uncoated 4261 lasers as a function of injected current at three different heat sink temperatures. Since all devices in this work are cleaved manually with the aid of a microscope, an error of ±10 μm in the cavity length should be assumed. The figure shows that the output power is reduced to almost half of its value when the heat sink temperature is increased by 4 °C. However, at a heat sink temperature of 28 °C the laser almost turns off. The figure also shows a roll-off of the power at injected currents > 220 mA, which can happen due to internal heating. Figure 4.1 also shows one of two odd shapes of the output power profile, which will be discussed in Sec. 4.3 of this chapter.

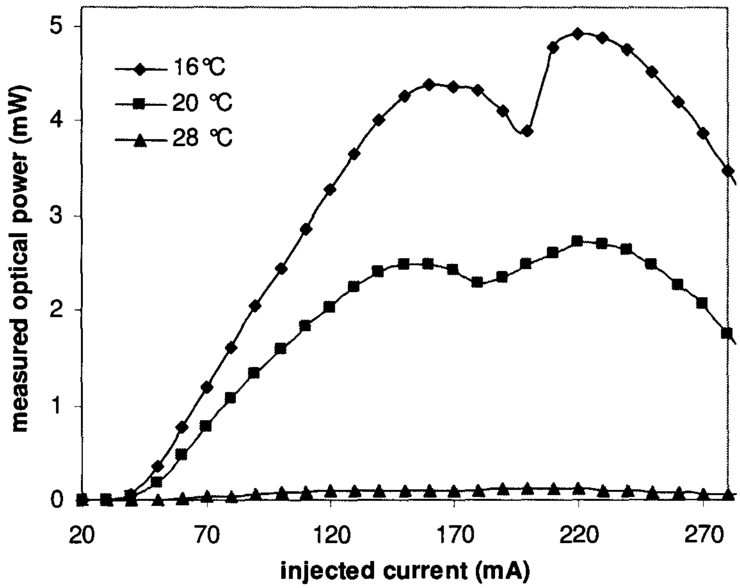

Figure 4.1: *Measured optical power of lasers from wafer 4261 as a function of injected current at three different temperatures. Output power degradation and thermal runaway are evident for currents above ~220 mA.*

As a starting point for my dissertation research, I thought of optimizing the optical confinement of the laser light. The reason for that is to see if the low output power and the odd power profile are related to a leaky optical confinement structure. At the beginning of Chapter 3 the simulation results of the optical confinement factor was presented. Using BPM optical simulation software, wafer 4261 showed a low optical confinement factor equal to ~ 1.5 % at a wavelength of 1600 nm and at lower wavelengths the confinement factor reaches ~1.1% with a dip around a wavelength of 1540 nm. See Figure 3.1 in Chapter 3. It was concluded from the simulations that the optical mode was not centered on the active region, which was the reason for such a low confinement factor value. It turned out that optimizing the cap layer in the ridge to a thickness of 1.7 μm helped to center the optical mode on the active region. The confinement factor improved to a value of 2.5 % but yet it still dipped down to a low value of ~ 1 % at a wavelength of 1500 nm. The next step was to optimize the SCH layer to reduce the optical leaks at the short wavelengths. The goal was to make the confinement factor as flat as it can be across the wavelength range of 1450 - 1600 nm. An improved confinement factor of 2.5–3.5 % was achieved for the proposed wavelength ranges (see Figure 3.1 in Chapter 3)

Experimentally, near field IR CCD camera images of AMQW laser diodes from wafer 4261 and optimized confinement factor 4381 wafer were taken to look at the output beam profile (see Appendix B for the structures). Figure 4.2 show the images at different current injection levels for both wafers. The images are normalized to the total intensity level. The figure shows that the intensity of 4381 laser is higher than that of 4261. Figure 4.2 also shows that both lasers are working as single spatial mode lasers even at 200 mA injection current where the dip in the power profile is observed.

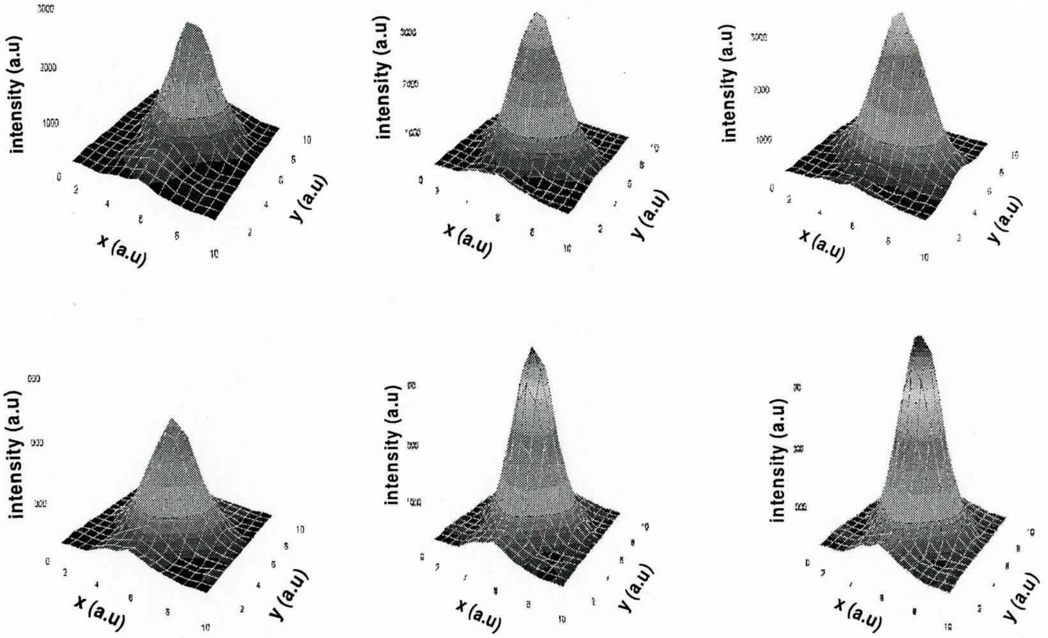

Figure 4.2: *Near field IR CCD camera images of old and optimized AMQW laser diodes at heat sink temperature of 16°C. All images are normalized to the total intensity level. The top row is for wafer 4261 and the bottom row is for optimized wafer 4381. The images were taken at injected currents of 100, 200, and 250 mA.*

The measured far field data for both wafers are shown in Figure 4.3. The figure shows the measured far field data at 100 mA (top curves) and at 200 mA (bottom curves) in both the *x*-direction (left curves) and *y*-directions (right curves). The y-direction is the growth direction (the perpendicular direction) while the *x*-direction (the lateral direction) is perpendicular to the growth direction and parallel to the facets. The far field data in Figure 4.3 show that the new wafer (4381) has a slightly tighter far field profile than the old wafer (4261), especially in the *x*-direction. Also, the figure show that the laser runs in a single spatial mode at both current levels, which confirms the data from the near field IR images. This result rules out the possibility that multi-spatial mode operation causes the dip in the output power profile in Figure 4.1 at 200 mA.

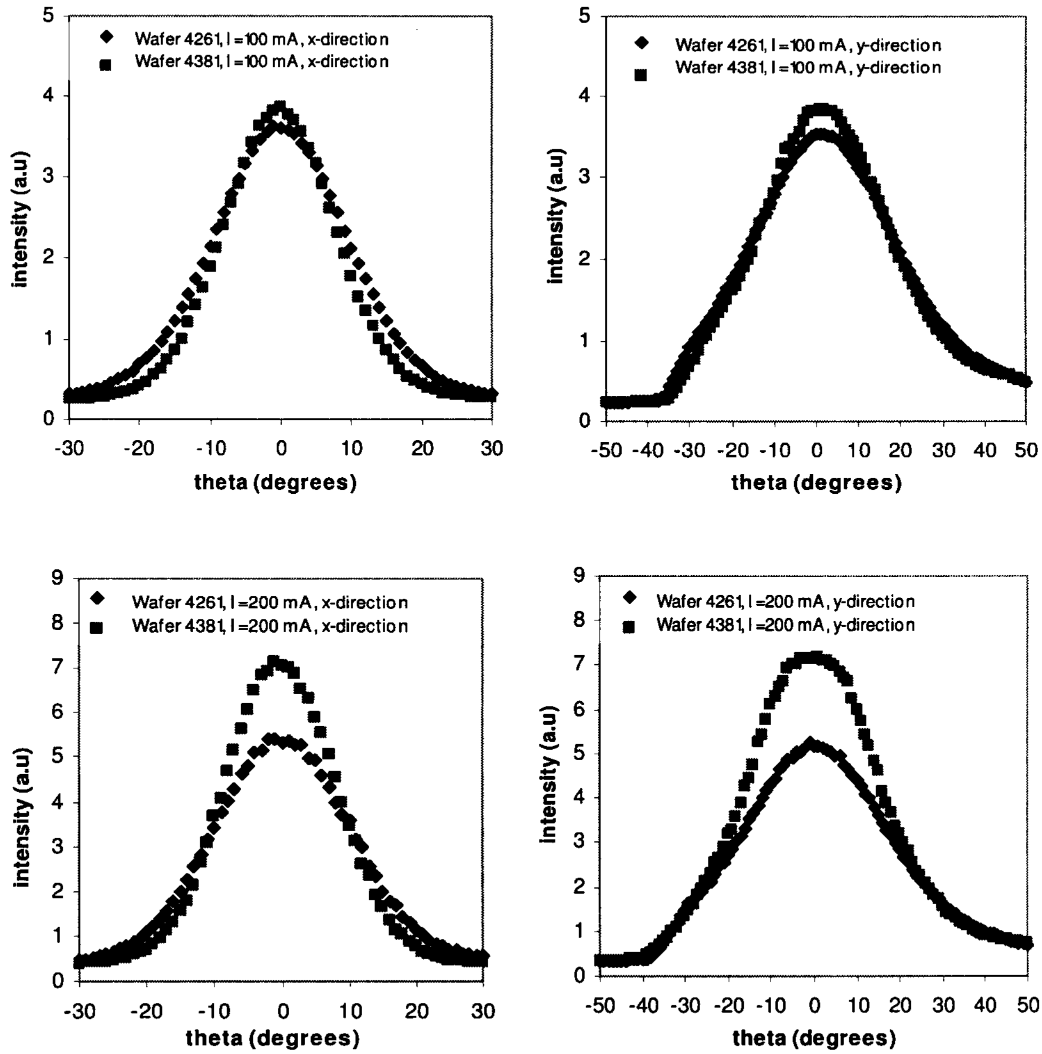

Figure 4.3: *A comparison of the measured far field data between wafer 4261 and wafer 4381, which has an optimized optical confinement, at 100 mA injected current (top curves) and 200 mA injected current (bottom curves). The x-direction data is on the left side and y-direction data on the right side. The y-direction is the growth direction while the x-direction is the lateral direction.*

Figure 4.4 shows a comparison of the output power of six devices for both the old and the optimized confinement factor wafers. The figure shows two output power profile types that are common with these AMQW wafers. Figure 4.4 also shows a significant improvement of the laser output power for the optimized confinement factor wafer 4381. The output power is almost doubled for the optimized wafer for the same current. All the measured devices through this work are uncoated facet devices. The curves on the left hand side are for 900 μm long devices and on the right hand side are for 800 μm long

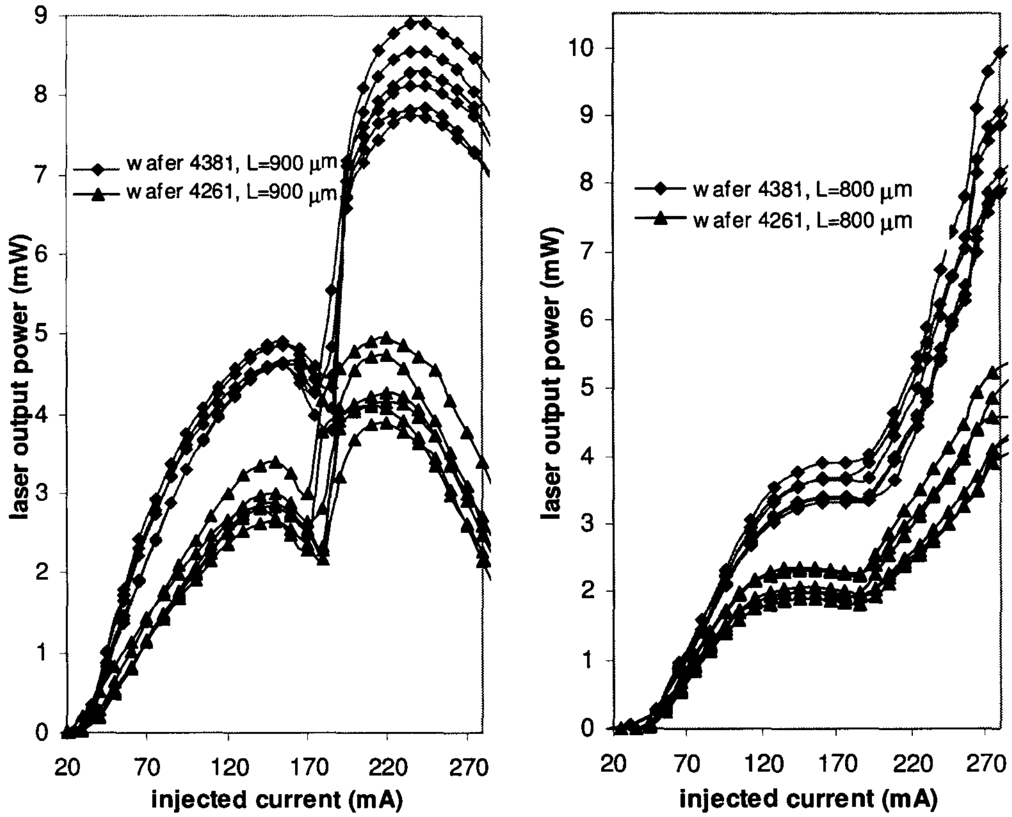

Figure 4.4: *Output power of 6 devices for lasers from both 4261 and 4381 at different current injection levels. The left hand plot for laser length L=900μm while the right hand plot for laser length L=800μm.*

devices. For this particular active region structure and doping profile, which both wafers share, usually devices with lengths roughly between 750 – 850 μm show output power profiles similar to the one on the right hand side whereas devices shorter or longer than this range have output power profiles similar to the one on the left. Figure 4.4 shows the importance of centering the optical field on the active area and optimizing the SCH layers to form optical confinement on the active area. Since the optical field was not centered on the active area in wafer (4261) and the confinement factor was not optimal, the efficiency of generating laser light is reduced. This process caused the degradation of the laser output power for lasers from wafer 4261 in comparison with lasers from wafer 4381. As for tunability, the optimized wafer 4381 devices gave a tuning range of ~106 nm[94], which is very close to the tuning range of 110 nm that was obtained from wafer 4261 and is reported in Chapter 1.

Since I was confident that the guiding properties were optimized, I could move forward and optimize the electrical and thermal properties of the laser. Let us not forget that one of the objectives of this work is to improve the optical performance and maintain the wide tunability of the AMQW ridge waveguide lasers.

4.2 Optimized doping profile – experimental results:

In Sec. 3.1, the effect of the doping profile on the laser electrical and thermal efficiency was studied theoretically. It turned out that extending the doping profile inside the SCH layers and close to the active region interfaces increases the current injection efficiency from 17 % to about 25 %, which is roughly a 50 % increase. At the same time the device temperature – in general – and the maximum temperature – in particular – for the optimized doping profile was predicted to be significantly lower than that of wafer 4381. The difference in the device maximum temperature between the two wafers was found to increase when more current was injected to the device (see Figure 3.13). In other words, the rate of heating of devices with doping that stopped at the SCH layers was predicted to be faster than that in the extended doping (ED) devices. At an active region current density of 1.17×10^{7} A/m^{2} the maximum temperature of an ED device was predicted to improve > 6 °C over 4381 devices. By comparing this temperature improvement to Figure 4.1 it is expected that the output power of an ED device will be more than twice the output power of a 4261 laser.

Keeping all of the above in mind, a new wafer, wafer 4693, was grown with a type 2 doping profile (see Sec. 3.2, Chapter 3 for more information about the type 2 doping profile). The new wafer, wafer 4693, has the same active region structure as wafers 4261 and 4381 (see Appendix B for lasers structure). After growth the new wafer was fabricated in the clean room according to the fabrication process detailed in Chapter 6. After fabrication, different length bars were cleaved and tested. Figure 4.5 show the IV curves for 900 μm long devices from wafers 4693 and 4381 at a heat sink temperature of 16 °C. The figure shows that the IV curves – for lasers of similar length and ridge width – vary from each other. Usually the IV curves vary according to the variation in the series resistance due to many issues, including the test setup. Most devices tested were in bar form and were not mounted as single devices on Cu blocks. The variation of the measured IV curves makes the process of tracking the improvement quite unrealistic.

Instead, the improvement was tracked with the measured output power and it was determined if the improvement agreed with the expectation derived from the simulation.

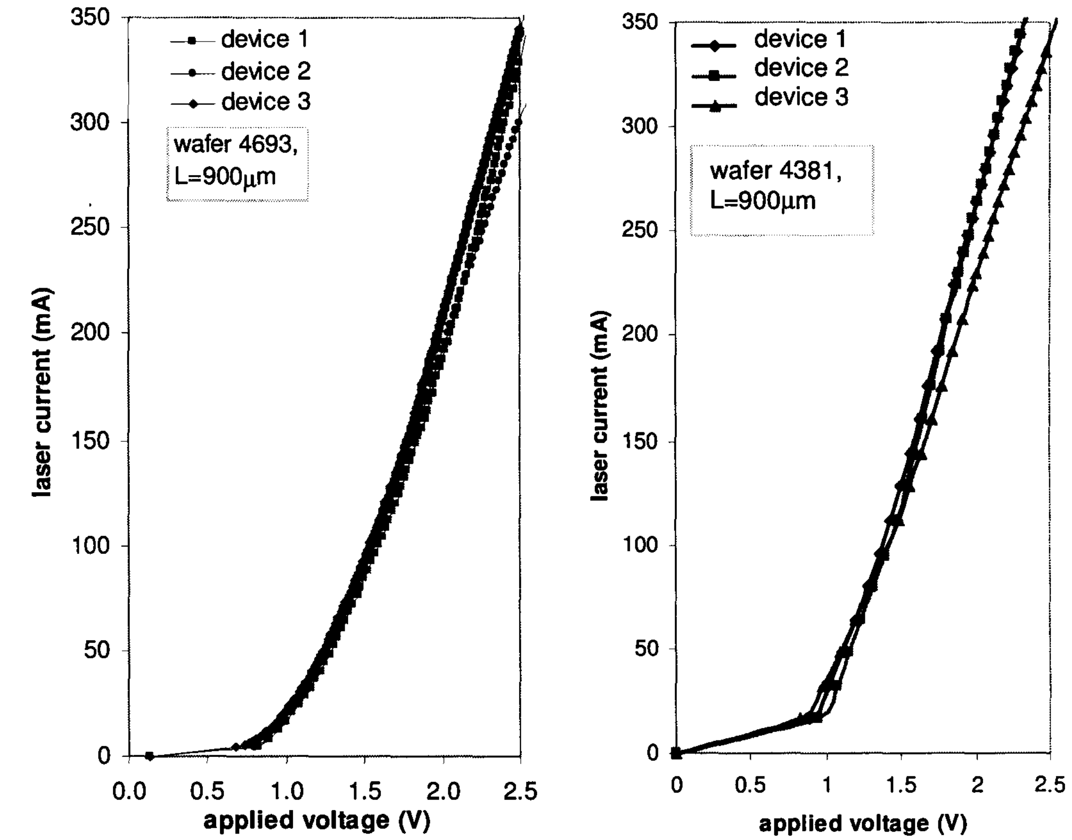

Figure 4.5: *Measured IV curves for three 900 μm long devices of wafer 4381 (right), and three 900 μm long devices of ED wafer 4693 (left). The IV curves vary for the same type devices. The left set of curves has more than double the data points in comparison with the right set of curves which cause the smooth turn on in the left curves.*

Figure 4.6 and Figure 4.7 show a comparison between measured laser output power of four devices from the ED wafer 4693 to the average of ten devices of previous wafers 4261 and 4381 (see Figure 4.4). The devices are 900 μm (Figure 4.6) and 800 μm (Figure 4.7) long with 3 μm ridge widths. All devices are measured at a heat sink temperature of 16 °C. Both figures show significant improvement of the laser output power of the ED devices over similar devices from 4381 and 4261 wafers. The figures show that the output power of ED devices improved almost four times than that of 4261 devices, and more than twice in comparison with 4381 devices. This improvement was predicted by the simulation results, which are shown in Chapter 3. The variation on the laser output power for the same length devices of the ED wafer 4693 depends on the different regions of the wafer from which these devices were cleaved.

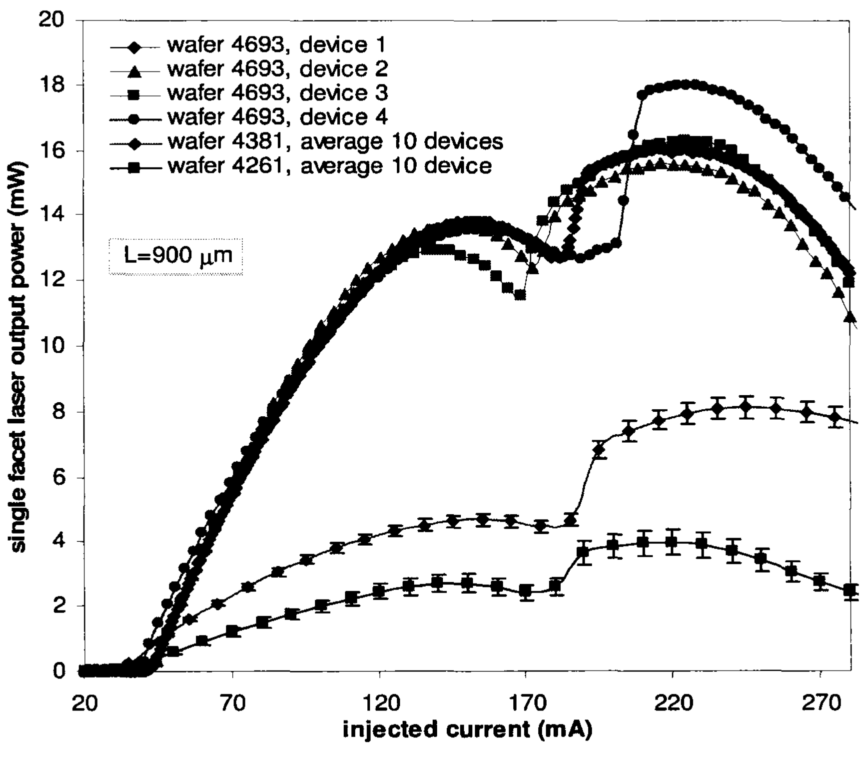

Figure 4.6: *A comparison of measured laser output power of four 900 μm long devices from the extended doping (ED) wafer 4693 (type 2 doping) to the average of ten similar devices of previous wafers (4261 and 4381). The error bars represent ±2σ from the mean value.*

Figure 4.6 and Figure 4.7 clearly indicate that extending the doping profile to the SCH layers improves significantly the laser output power. Now the question is why we did not see an increase in the internal losses due to extending the doping profile into the optical field as found by some researchers[77,78]. There is only one possible answer to this question. According to the results shown in both figures, it was concluded that the increase in optical power that was achieved by extending the doping very close to the SCH/active region interface is much more than the losses the laser suffers because of the interaction between the optical field and the carriers.

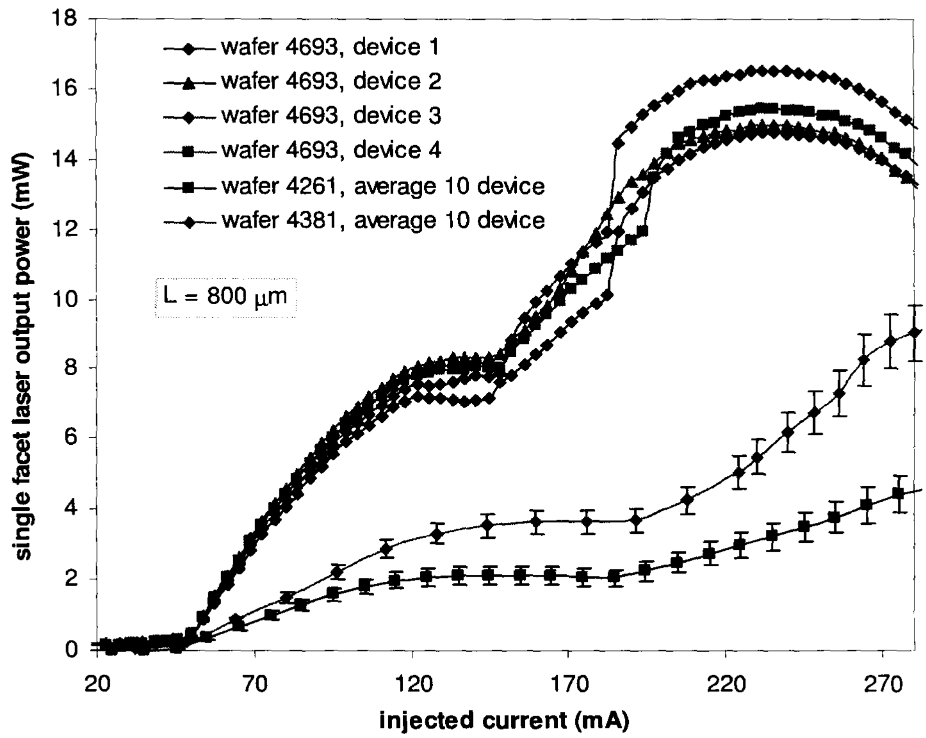

Figure 4.7: *A comparison of measured laser output power of four 800 μm long devices from the extended doping (ED) wafer 4693 (type 2 doping) to the average of ten similar devices of previous wafers (4261 and 4381). The error bars represent $\pm 2\sigma$ from the mean value.*

It is crucial that the ED (type 2 doping) laser switches operation between quantum wells with current. Figure 4.8 shows measured spectra for 700 μm device at different injected currents. The figure shows that the laser clearly switches between the long wavelength and short wavelength quantum wells. For 700 μm long devices the laser switched from the long wavelength quantum wells to the short wavelength quantum wells at around 140 mA current. The net gain coefficient was calculated from the measured data at high resolution. High resolution spectrometer measurements enable resolution of the Fabry–Pérot modes, which is crucial for calculating the net gain coefficient[95]. Figure 4.9 shows the net gain coefficient as a function of wavelength measured at 150 mA injected current. The figure shows a positive gain coefficient for over 130 nm with nearly a flat gain top. A tuning range similar to wafers 4261 and 4381was achieved with these devices.

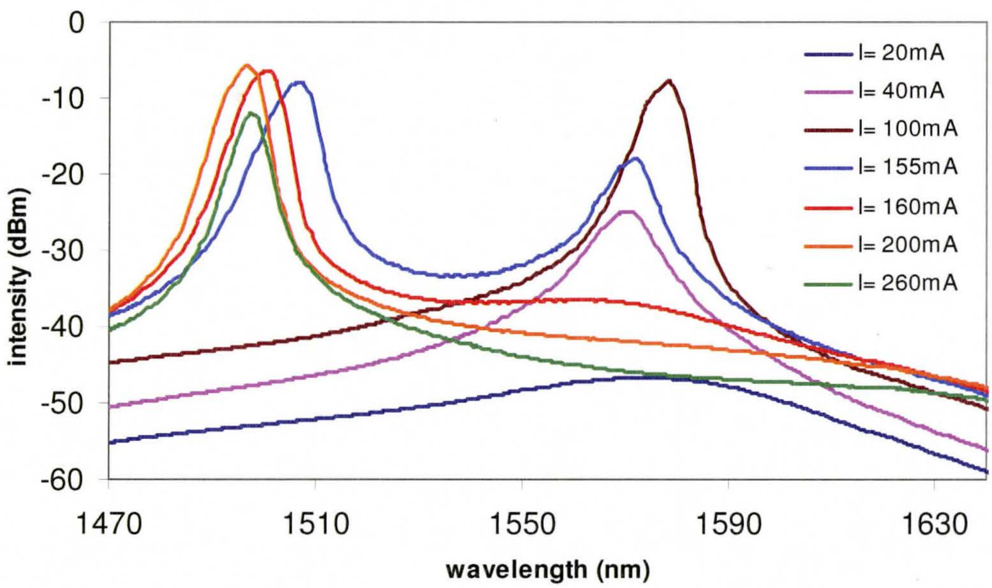

Figure 4.8: *Measured OSA data spectrum for the ED wafer 4693, the optimized doping profile, for 700μm length uncoated device.*

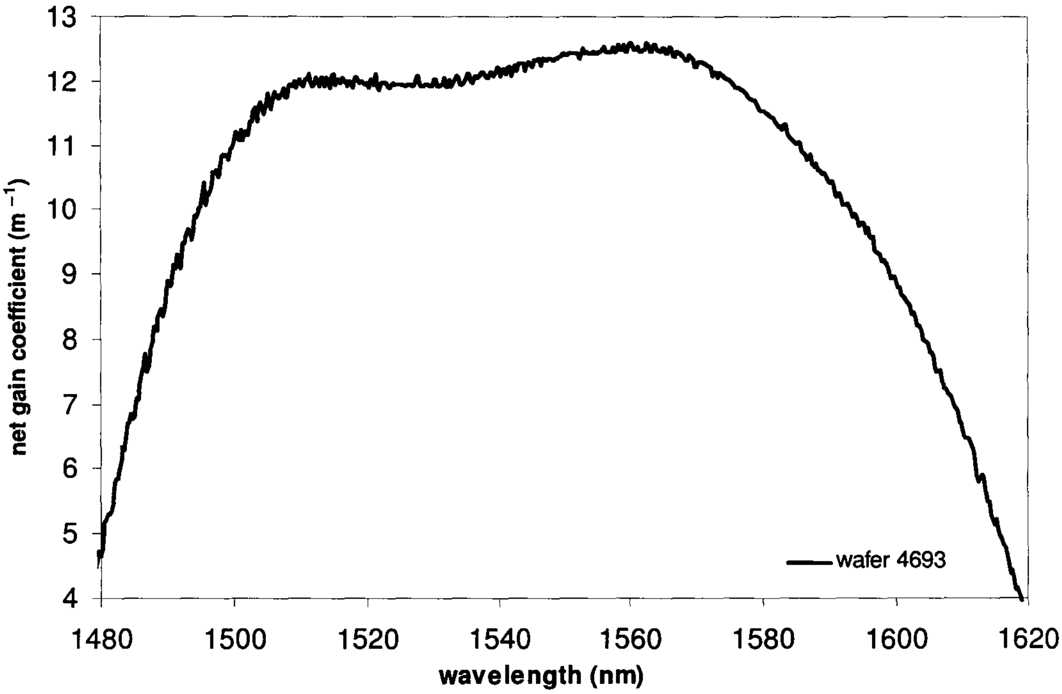

Figure 4.9: *The net gain coefficient calculated from the measured high resolution OSA data for type 2 doping (the extended doping) wafer 4693.*

Figure 4.10 show the sensitivity of an extended doping (type 2) laser to temperature. The figure shows the measured output power of a 900 μm long, 3 μm ridge width, uncoated laser as a function of injected current at three different heat sink temperatures. The figure shows that the output power lost on average ~22 % of its value when the heat sink temperature was increased by 4 °C. However, at a heat sink temperature of 28 °C the laser was still lasing with almost 40% of its original power when operating at 16 °C (compare Figure 4.10 with Figure 4.1). The characteristic temperature (T_0) was calculated from the experimental data in Figure 4.10 using the relation[96] $\frac{1}{T_0} = \frac{\partial \ln(I_{th})}{\partial T}$ and was found to be 59 K.

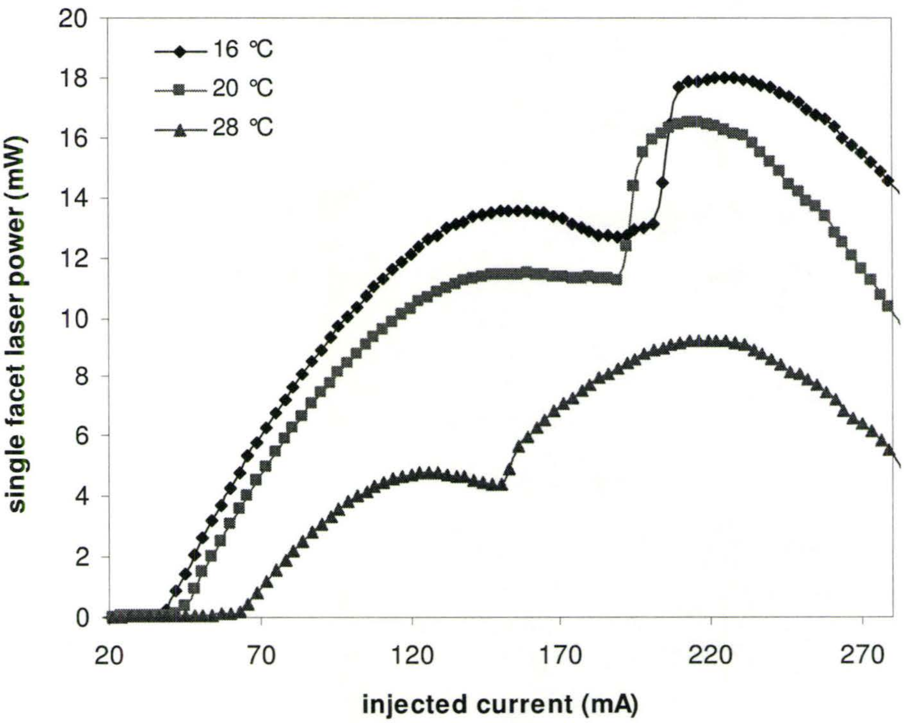

Figure 4.10: *Measured optical power of a laser from the ED (type 2) wafer, wafer 4693, as a function of injected current at three different temperatures (compare with Figure 4.1).*

One more interesting thing is shown in Figure 4.10. An increase of 12 °C lowered the current of the dip position to 25% of the original value. This means that the dip position is temperature sensitive.

4.3 The effect of AMQW laser length on output power profile:

In the previous two sections, it was shown that the power profile depends on the AMQW ridge waveguide laser length. I categorized all widely tunable AMQW lasers output power in two categories. The first category is for lasers with lengths in the range 750 – 850 μm, which is considered the transition cavity length[97] (TCL) range – the TCL depends on threshold, losses and doping in the laser – for these wafers. In this category the lasers take the output power profile similar to the one shown in Figure 4.7. The second category is for lasers with lengths 100 μm shorter or longer than the TCL range. These lasers take the output power profile similar to the one shown in Figure 4.6. There is a third category I did not include because the lasers in this category are not considered widely tunable. These lasers usually lase on either the long wavelength wells or on the shorter wavelength wells. The lasers that lase only on the long wavelength wells are much longer than the TCL. However the lasers that only lase on the shorter wavelength wells are much shorter than the TCL. In fact this is the definition of the TCL phenomena. Both these lasers are not considered widely tunable and the power profile shows only one threshold, similar to single quantum well lasers. For lasers close to the TCL length, as in Figure 4.6 and Figure 4.7, I also found out that the lasers are not running on multiple spatial modes, which could explain the second threshold or dip in the power profile.

The question now is why the laser length affects the output power profile in three different ways? Also, why is there more than one threshold in the widely tunable AMQW laser power profile?

To find answers to these questions, the reader should consider the spectra for 700, 800, and 900 μm long ED devices. Figure 4.11 – Figure 4.13 show measured spectra of uncoated laser diodes of the optimized doping wafer. Each figure shows for a different length laser diode. The figures show the switching sequence from the long wavelength wells to the short wavelength wells as the injected laser current is increased. Figure 4.11 shows that for the 700 μm device, the switching between the two wavelength regions occurred suddenly.

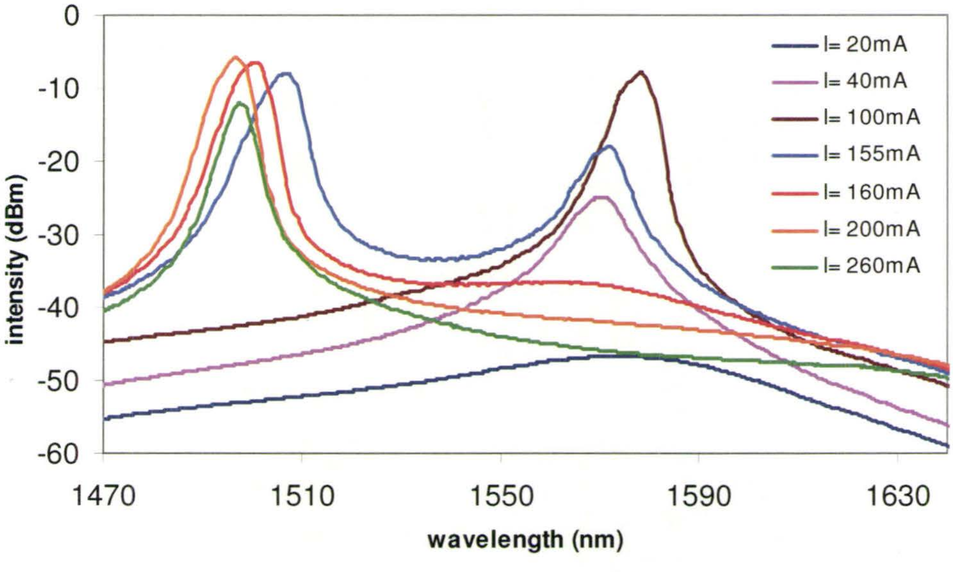

Figure 4.11: *Measured spectra for uncoated, 700μm long lasers from the ED wafer, wafer 4693.*

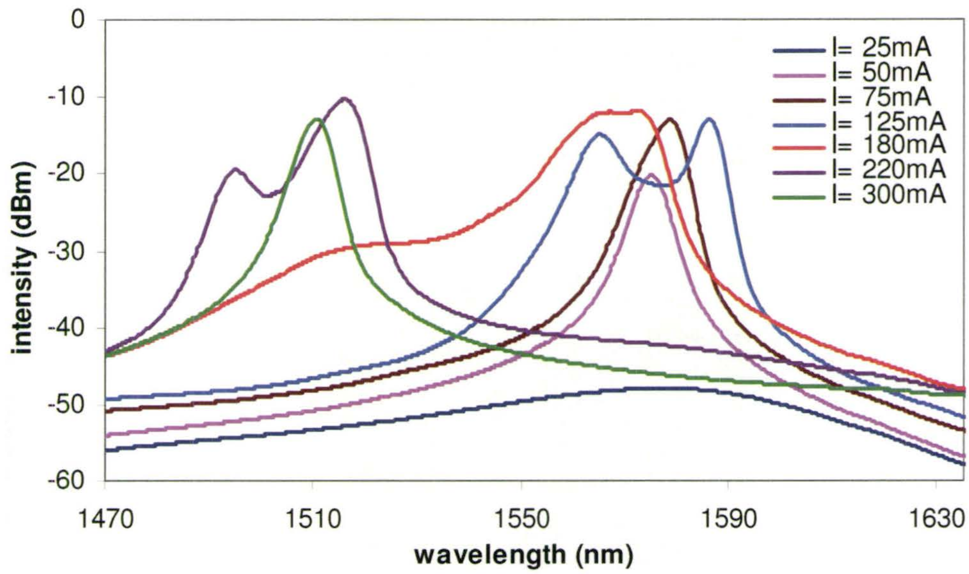

Figure 4.12: *Measured spectra for uncoated, 900μm long lasers from the ED wafer, wafer 4693.*

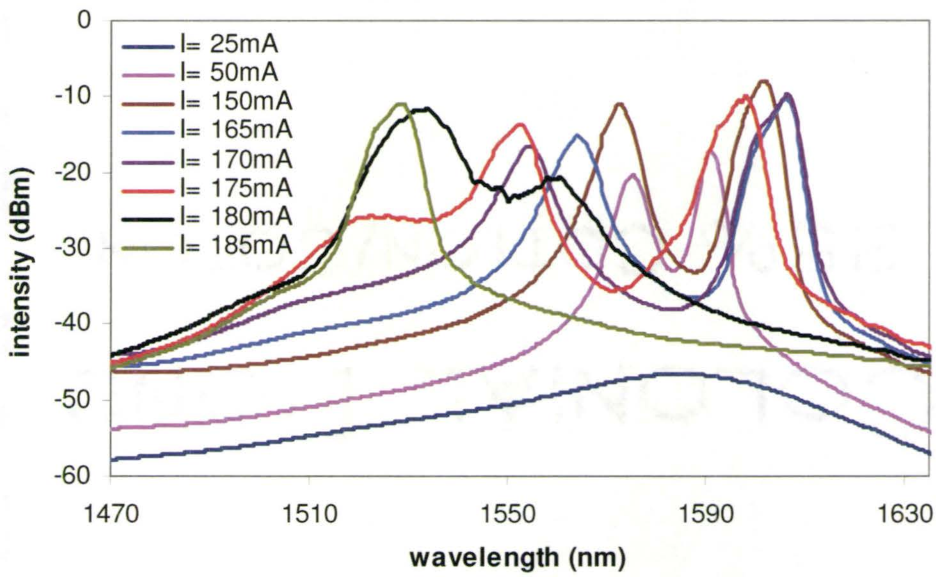

Figure 4.13: *Measured spectra for uncoated, 800μm long lasers from the ED wafer, wafer 4693.*

For the 700 μm long devices shown in Figure 4.11, the lasing stayed at the long wavelength wells until the injected current reached around 150 mA where the laser starts to show peaks at both long and short wells. Then the laser suddenly, at around 160 mA, starts to lase at the shorter wavelength wells.

In Figure 4.12 a different scenario occurs, there were stages where the laser started to lase at multiple peaks about 20 – 30 nm apart. The multiple wavelength lasing started at currents around 100 mA (curve not shown in the figure). This multiple wavelength lasing, in one stage, was centered near the long wavelength wells and then shifted as the current was increased to be centered on the shorter wavelength wells. The laser then switched again and started to lase at a single peak on the shorter wavelength wells. During the lasing process there was no lasing peak that passed through the center of the spectrum. The 800 μm long laser in Figure 4.13 behaved in a similar way to the laser in Figure 4.12. The difference in lasing behaviour occurred when the laser started to lase on multiple peaks centered at the long wavelength wells. When the injected current increased, the multiple wavelength peaks start to move farther away from each other. (See the spectra at currents in the range of 150 – 175 mA in Figure 4.13.) During this process the second peak – the inner peak – scanned through the center of the spectrum at 165 mA. At an injected current ~ 175 mA a third peak started to show and was centered on the shorter wavelength wells. Then, the laser switched to operation on two peaks centered on the shorter wavelength wells.

The last three figures show an interesting lasing behavior of these lasers. To understand how this lasing behavior is related to the laser output power profile, the reader should consider the optical power of 700 μm, 800 μm, and 900 μm lasers. Figure 4.14 shows the measured output power profile and the lasing wavelength as a function of injected current for 700 μm extended doping (ED) diode lasers. The figure shows that the second threshold in the power profile (dip) is coincident with the shift from long wavelength wells to the short wavelength wells. To explain physically why this dip happens, it is necessary to keep in mind that the gain of AMQW lasers depends on the carrier density (see Chapter 1, Figure 1.4). The long wavelength wells (LWW) reach the transparency condition at lower carrier density than the shorter wavelength wells (SWW). The reason for this is because the LWW quasi-Fermi level is lower in energy than that of the SWW. So, at low currents the laser diode will lase at the LWW after the first threshold. This is what we see in the OSA data Figure 4.11 and in the power profile data Figure 4.14. At a certain current level – in the 700 μm devices this current is around 90 mA – the lower energy states are filled – LWW reach saturation – so the carriers will start to fill in higher energy states (the SWW). Now, as more carriers are injected, these carriers will not participate in generating light since the SWW has not yet reached the transparency condition. However, injecting more carriers will heat up the device more; this explains why we see this dip or the second threshold in the output power profile. There is also the possibility that some of the carriers are siphoned off from the LWW, which can contribute to the dip as well.

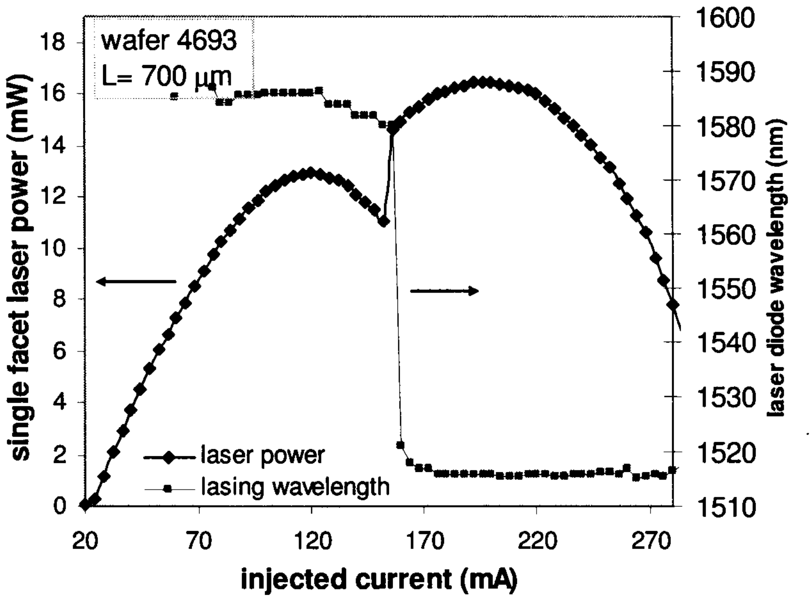

Figure 4.14: *Measured output power profile (left scale), and the first peak wavelength (right scale) as a function of injected current for 700 μm long, extended doping (ED) diode lasers.*

Figure 4.14 shows the lasing wavelength is blue shifting about 8 nm during the power roll-off. Usually when current is increased in AMQW lasers we see a red shift of this amount as a thermal effect. But this blue shift is happening because the gain is broadening towards the SWW as a result of a carrier concentration increase in the SWW. At a certain current level – in the 700 μm devices this current is around 150 mA – the transparency condition is satisfied for the SWW and the SWW start to lase. This is clear from Figure 4.14 and Figure 4.11 where the output power jumps up again and where the laser wavelength switches to the SWW. Then, the power will keep rising as more carriers are injected until the SWW saturates. At this point the power will start rolling-off again due to SWW saturation.

The 900 μm long ED laser shows similar behaviour for the output power profile as the 700 μm long ED laser (see Figure 4.6). The only difference was in the OSA data where it showed the broadening of the first peak into two peaks centered on the LWW region. These two peaks shifted together and centered on the SWW region; see Figure 4.12.

The output power profile for an 800 μm long ED laser is shown in Figure 4.15. The figure also shows the lasing wavelength as it shifts with the increase of injected current. As explained earlier, this is the second form of the laser output power profile where the difference between this profile and the profile shown Figure 4.14 is in the middle region. After the LWW saturate in this laser the output power goes through the roll-off behaviour as was explained above. This roll-off occurs very quickly and the output power goes through a linear behaviour with injection current even though the transparency condition is not yet met for the SWW. The laser at this level of current injection seems to repeat the first lasing power behaviour. Once the transparency condition is satisfied the laser output power shows a jump and then the laser goes through the normal saturation and the final roll-off as in the previous 700 μm and 900 μm ED lasers. The output power behaviour of the 700, 800, and 900 μm devices is the result of interaction of the following three conditions: (i) the transparency condition, which is the condition for a quantum well to reach threshold and start lasing; (ii) the TCL condition, which is a condition that the laser has to meet to shift wavelength from the LWW to SWW; and, (iii) the gain flatness condition, which depends on the QW structure and the level of carriers injected to the device. The 900 μm and 700 μm lasers in Figure 4.6 and

Figure 4.14 are in the range of lengths of the TCL but about 100 μm far from the center value. The result is that these lasers lase on the LWW at threshold and once the LWW are saturated, the carriers will start to pump the SWW. This will be observed as the dip in the power profile since the SWW did not reach its threshold. Once the SWW reach their lasing threshold a significant jump in the output power profile happens, which clearly can be seen in both Figure 4.6 and Figure 4.14. Now the story is different for the 800 μm device in Figure 4.15. Once that threshold condition for the LWW is met the laser will lase at the LWW. If the current increases the laser power will increase until the LWW saturates and the roll-off will start. Figure 4.15 shows that the roll-off process is cut short and the laser will resume the power increase and the dip doesn't show for the 800 μm devices. So the question is why the 800 μm devices behave this way. As a simple answer we can say that the 800 μm device satisfies the TCL center value. So, the question now will be why, when the laser length satisfies the TCL center value, the output power profile takes the second category shown in Figure 4.15 and the wavelength transition moves smoothly with the increase of carriers as shown in Figure 4.13? It turns out that when the laser length satisfies the TCL center value the LWW threshold increases i.e., the 700, 800 and 900 μm lasers used in this study have LWW thresholds of 24, 47, and 39 mA respectively. The reasonable explanation to this threshold increase is that both LWW and SWW are getting pumped when current is injected into the 800 μm laser. When the threshold condition is satisfied for the LWW of the laser, the laser will start lasing but since both wells are being pumped it will take longer for the device to start to lase at the LWW. At this point the SWW will be partially filled. Once the LWW saturates and the roll-off starts the SWW does not need much current to lase because it has been pumped from the beginning. This explains why we don't see the dip in the power profile in Figure 4.15 and why the wavelength switching for this device is smooth.

Clearly the discussion above shows that the TCL[95,97] is not one specific length, as has been recognized and published. The TCL is a range of lengths around a center length in which the laser can switch between the LWW and the SWW, and where the smoothness of the switch increases as the laser length come closer to the center value. Below or above this range the laser reaches threshold on the SWW or the LWW only.

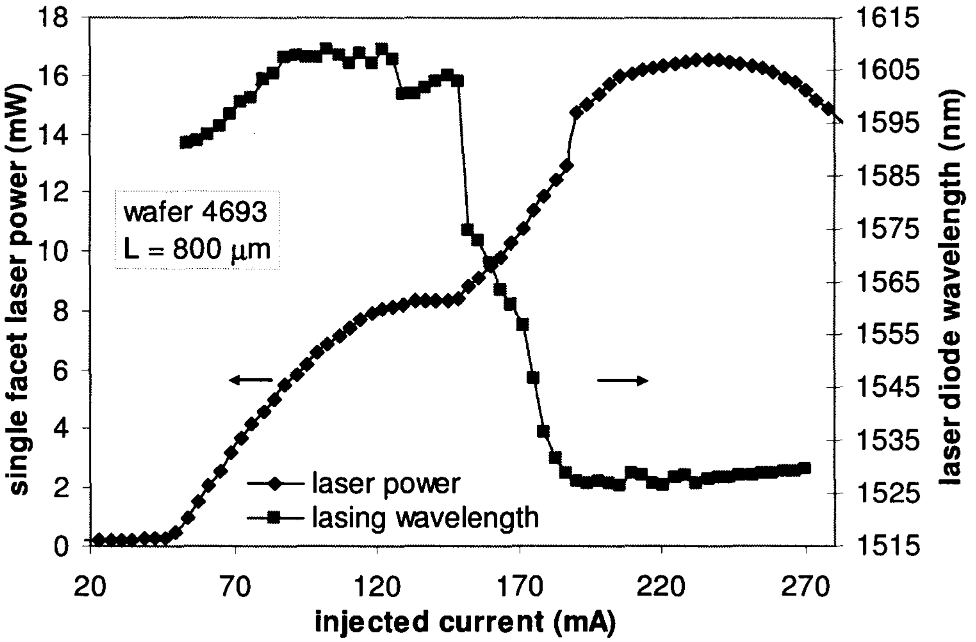

Figure 4.15: *Measured output power profile (left scale), and the first peak wavelength (right scale) as a function of injected current for 800 μm long, extended doping (ED) diode lasers.*

To apply this definition to the last wafer, wafer 4693, it can be concluded that the center value of the TCL for that wafer is approximately ~ 845 μm and the lower limit for the TCL span is ~ 670 μm while the upper limit is ~ 1020 μm. It turned out that for wafer 4693, lasers with lengths 650 μm and below lase only on the SWW and lasers with lengths 1050 μm and above lase only on the LWW.

As a result, from the above one can predict that lasers with lengths near the center of the TCL range will tune very smoothly in an external cavity[98] or split cavity[94] configurations also, these lasers should not suffer from gaps in the tuning spectrum. I also predict that the output power profile will be close to the output power profile of a single QW device in terms of no dip in the middle of the profile. Going back to the OSA data, Figure 4.11 – Figure 4.13, it is clear that the 700 μm devices are at the lower limit of the TCL so the transition was a jumping transition. The 900 μm devices are close enough to the center value that a relatively smooth shifting with a small jumping gap in the middle of the spectrum is observed. 800 μm devices are close to the center value of the TCL, such that the smoothness of the transition was clear where the second peak of the spectrum scanned over a broad range of wavelengths with no gap in the middle of the spectrum. This smoothness was reflected in the output power profile where it cut short the first roll-off of the power curve and gave a linear relation with the injected current. This linear relation is a direct effect of the relation between the carrier concentration and the gain curve as discussed earlier.

4.4 IEM experimental results:

In Sec. 3.3, simulation data for the isolation etch method (IEM) technique was introduced, which I proposed to improve current injection efficiency to the active region. In this section, the experimental results of processed lasers using the IEM are discussed. The mask was designed so that in each bar there will be three repeats of the following set of lasers (see Figure 4.16). One laser without any IEM processing, and the next adjacent 4 lasers are with isolation etched grooves 1, 3, 5, and 7 μm away from the ridge sides on both sides of the ridge. The reason for this design is to reduce the variation in the outcomes as a result of wafer non-uniformity.

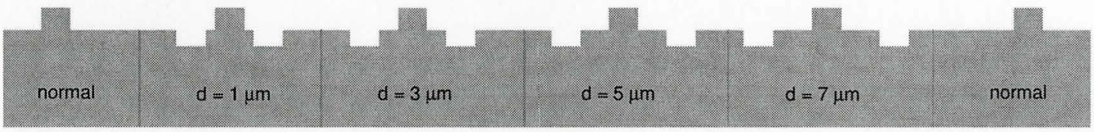

Figure 4.16: *A depiction of the set of lasers that is fabricated as three repeats in each laser bar. The distance between the ridge sidewall and the etched grooves represented by d = (1, 3, 5, or 7) μm.*

Experimentally it was found that devices adjacent to each other usually carry similar characteristics. After fabrication using the procedure detailed in Chapter 6, several bars where cleaved and tested.

Figure 4.17 shows the measured output power for 900 μm with 4 μm ridge ED normal (no grooves) and IEM devices with 1 μm grooves away from each ridge side (left scale) denoted with solid marks. Also, the figure shows the lasing wavelength for both devices (right scale) denoted with the same color but hollow marks. The figure shows the expected output power profile for the normal 900 μm long devices although the dip in the power profile was at a current above 280 mA (previous devices shifted below 200 mA). The reason for this change is the different ridge size for these devices (4 μm instead of 3 μm for the previous devices).

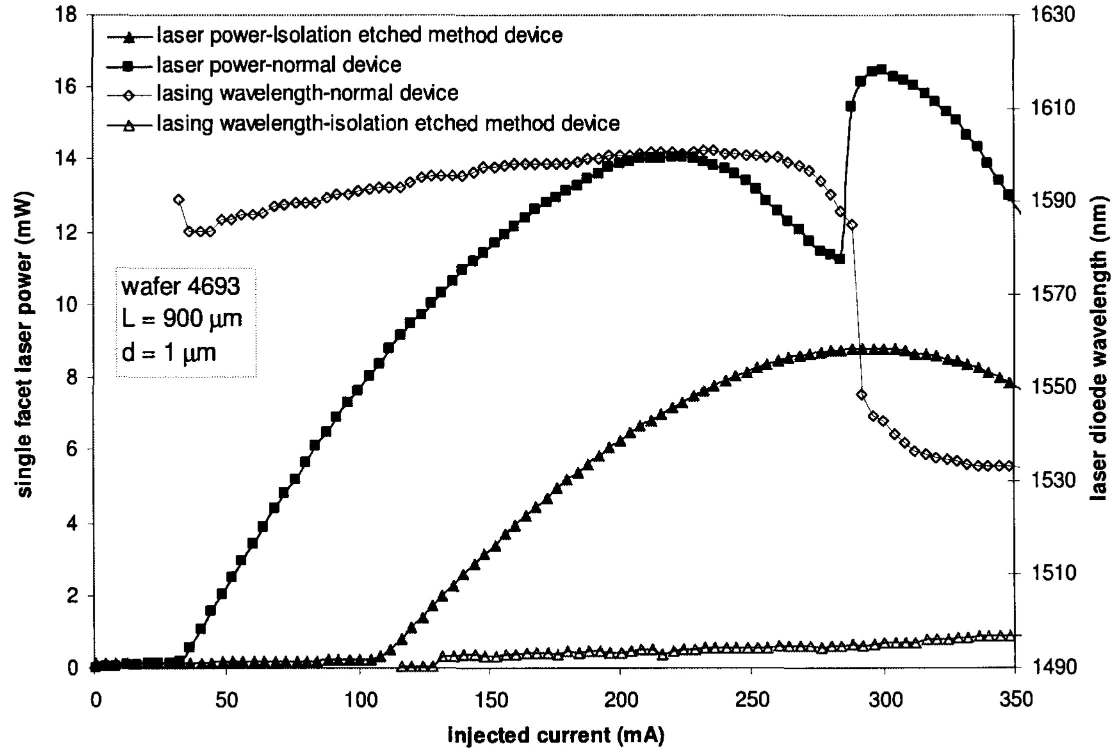

Figure 4.17: *Measured output power profile for normal and IEM 1 μm from the ridge (solid marks– left scale), and the laser first peak wavelength (hollow – right scale) as a function of injected current for 900 μm long, 4 μm ridge width, extended doping (ED) diode lasers.*

Interestingly enough, the figure shows that the similar adjacent devices with IEM grooves 1 μm away from the sides of the ridge operate only on the SWW. This is justified because the lasing wavelength of the device stayed at the SWW region, which explains why there was no dip in the power profile. Figure 4.17 also shows another interesting feature. This figure shows that the SWW lasing threshold was significantly lower (~104 mA) than that of the normal device (~284-288 mA). This is a clear indication that the current injection efficiency was nearly three times higher than that in the normal device. This is what the simulation results in Sec. 3.3.1 Chapter 3 predicted (~ 80 % injection efficiency for IEM 1 compared with ~ 25 % for the normal devices). However, the laser out put power was on average ~ 45 % lower than that of the normal device. The reason for the reduced power is that the grooves, which were 1 μm away from the ridge sides, introduced recombination centers that used a significant fraction of the injected carriers. A higher density of carriers was needed to overcome the losses, thus the SWW were filled and the laser lased on the SWW.

In Sec. 3.3.1 it was shown that when recombination centers were introduced the current injection efficiency reduced to 57 % and the laser temperature increased owing to the heating that is taking place from these recombination centers (RC). Although the injection efficiency in the IEM device with RC is now more than twice that of the normal device, the increase of the losses because of the RC and the increase of the temperature of the device are the causes of the output power drop of this device (see Figure 4.17).

Now the question one can ask is that; if the injection efficiency after introducing the RC went down to 57 %, which is slightly more than double the injection efficiency of the normal device (25 %), how come the experimental data – Figure 4.17 – still show an improvement in injection efficiency of nearly three times? To answer this question we need to go back to Figure 4.10. One of the interesting things the figure shows is the reduction in the current of the position of the dip (the second threshold) of about 50 mA as the temperature increased 12 °C. This phenomenon is not a new finding as Wang[95] reported that increasing the temperature assisted in the transition from the LWW to the SWW. The new finding here is the temperature sensitivity of the shift. Figure 4.18 shows the measured result and the best fit equation of this relation. (The shift data are extracted from the experimental data in Figure 4.10).

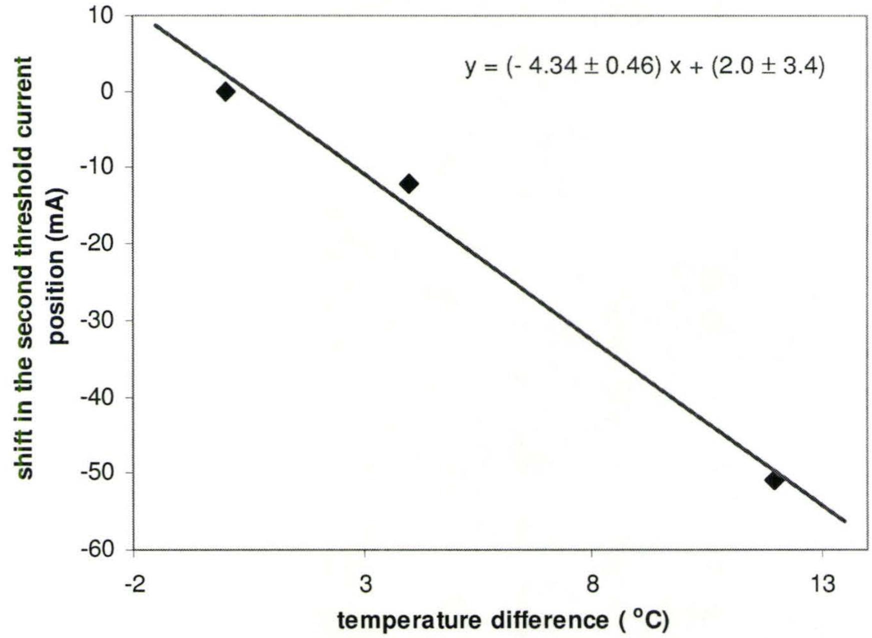

Figure 4.18: *The shift in the second threshold current position as a function of temperature difference. The data was extracted from the experimental measurements represented in Figure 4.10.*

To go back and answer the last question, it was found from the simulation data that introducing the grooves and recombination centers increases the temperature of the active region on average by ~ 9 °C. This result can be verified by comparing the reduction in measured power between Figure 4.17 and Figure 4.10, which gives an increase of ~ 10 °C. By using a 9 °C value extracted from simulation results and applying it to the relation extracted from Figure 4.18, I can calculate the shift in the second threshold due to thermal effects as 36.6 ± 7.7 mA. So to find the expected second threshold position for the IEM 1 device – without the thermal effect – we must add the 36.6 ± 7.7 mA value to the existing threshold of 104 mA which gives 140.6 ± 7.7 mA. Now using this new value, the second threshold position for the normal device can be found (without IEM or RCs). We know from the simulation data that normal device injection efficiency is almost half of the IEM 1 device. This tells us that the expected second threshold position for the normal device must be double 140.6 ± 7.7 mA. The experimental data from Figure 4.17 showed that it is 286 ± 2 mA, which is 2 × 140.6 ± 7.7 mA within experimental uncertainty.

This analysis answers the question as to the reason the experimental data – Figure 4.17 – still show an improvement in injection efficiency of nearly three times while the injection efficiency after introducing the RC went down to double the injection efficiency of normal devices. It shows that there is no confusion between the simulation and experimental results. The analysis also shows the close agreement between the simulation predictions and the experimental results. It shows that the Flex PDE simulation code can predict the experimental results of the AMQW ridge waveguide laser within the statistical limitations considering the three data points used in the fitting in Figure 4.18.

Now let us go back and see the experimental results for the rest of the IEM devices. Figure 4.19 shows the measured output power profile for a normal device and an IEM device with trenches 7 μm away from the ridge walls (solid marks, left scale), and the lasing wavelength (hollow marks, right scale) as a function of injected current.

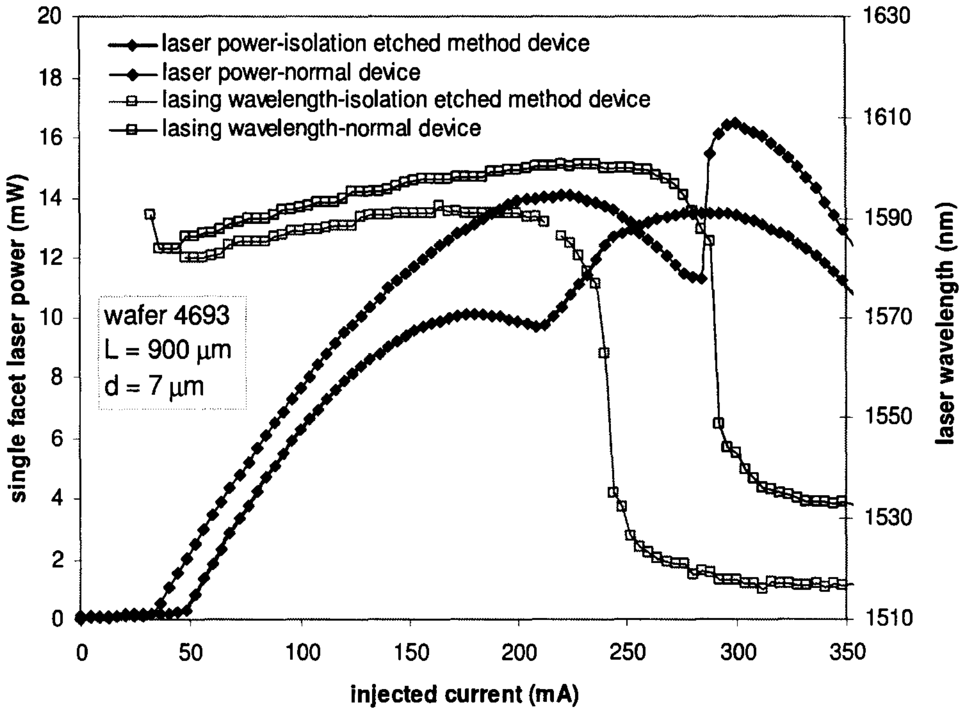

Figure 4.19: *Measured output power profile for normal device and IEM device with d = 7 μm from the ridge (solid marks– left scale), and the laser first peak wavelength (hollow marks – right scale) as a function of injected current for 900 μm, 4 μm ridge width, extended doping (ED) diode lasers.*

Both the normal and the 7 μm IEM device were made from 900 μm long, 4 μm ridge extended doping (ED) diode lasers. The figure shows that the output power of the 7 μm IEM device is 13% lower than that of the normal device. To explain this result, it was found from the simulations that the current injection efficiency did not significantly improve over normal lasers for this type of device. It appears that the distance between the grooves and the ridge (7 μm) is not short enough to prevent the carriers from leaking around the ridge sides. However, the grooves introduced recombination centers that rob carriers and heat up the device. The increase in the temperature causes the power to degrade and together with a small increase in the injection efficiency caused the shift in the second threshold.

Figure 4.20 shows the measured output power profile for a normal device and a 5 μm IEM device, which has the isolation trenches 5 μm away from the ridge (solid marks, left scale), and the lasing wavelength (hollow marks, right scale) as a function of injected current. Both devices were fabricated from 900 μm long, 4 μm ridge, extended doping (ED) diode lasers. The figure shows that the output power of 5 μm IEM device is slightly higher than that of a normal device. To explain this result, it was found from the simulations that the current injection efficiency improved over normal lasers for this type of device. This improvement increased the output power of the device however it introduced recombination centers that heat up the device and degrade the output power of the laser. As a result the overall power improvement was slightly higher than that of the normal device. Again the improvement in the injection efficiency together with the increase in laser temperature is the cause of the shift in the second threshold.

As for the 3 μm IEM device with grooves 3 μm away from the ridge, Figure 4.21 shows the measured output power of the device in comparison with the normal device. The figure shows that the output power of a 3μm IEM laser is slightly lower than that of the normal device in the first stage (before the second threshold). In the second stage the

3 μm IEM laser output power was slightly higher than that of the normal device. The current injection efficiency from the simulation was close to 33 %, which is higher than that of normal lasers for this type of device. However, because of the relative closeness of the recombination centers to the ridge area (3 μm) a fraction of the injected carriers was lost to the recombination centers. The consumption of carriers is the cause of the increase in the first threshold of the LI curve for this device and the power degradation in the first stage.

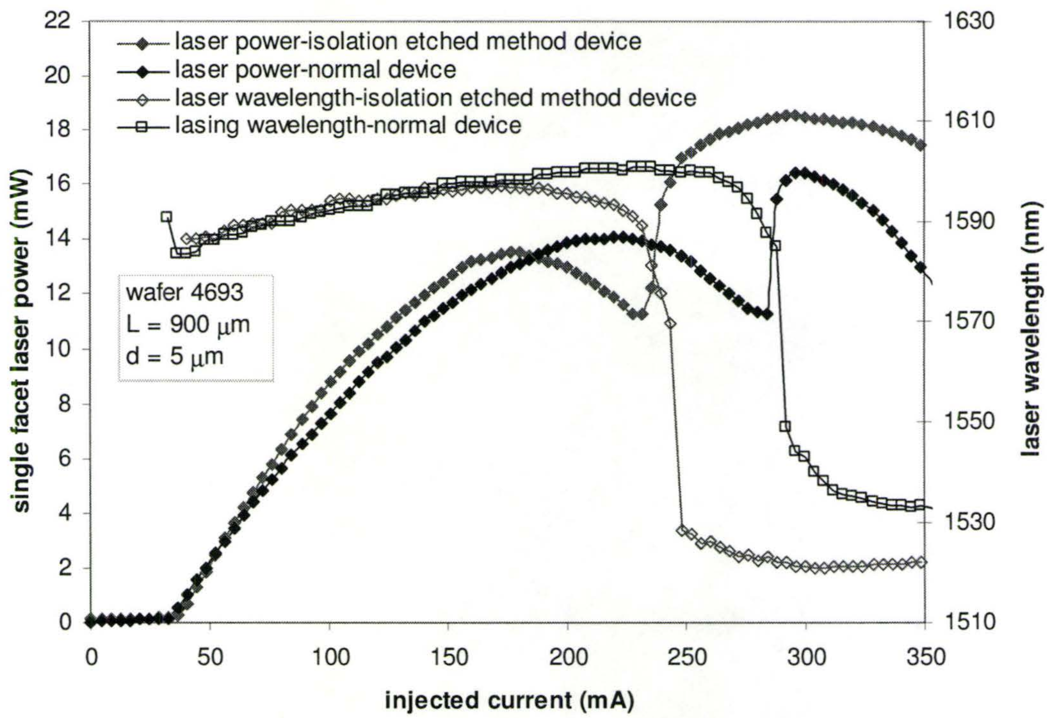

Figure 4.20: *Measured output power profile for normal device and IEM device with d = 5 μm from the ridge (solid marks– left scale), and the laser first peak wavelength (hollow marks – right scale) as a function of injected current for 900 μm long, 4 μm ridge width of wafer 4693 lasers.*

Once the recombination centers were filled and the laser went through the second threshold, the power increased as a result of the improvement of the current injection efficiency. Again the improvement in the injection efficiency together with the increase in laser temperature is the cause of the shift in the second threshold.

The results for the 5 μm IEM and 3 μm IEM devices showed that the IEM worked to improve the current injection efficiency of the laser. It also showed that in order for this method to give the desired results a passivation technique needs to be developed.

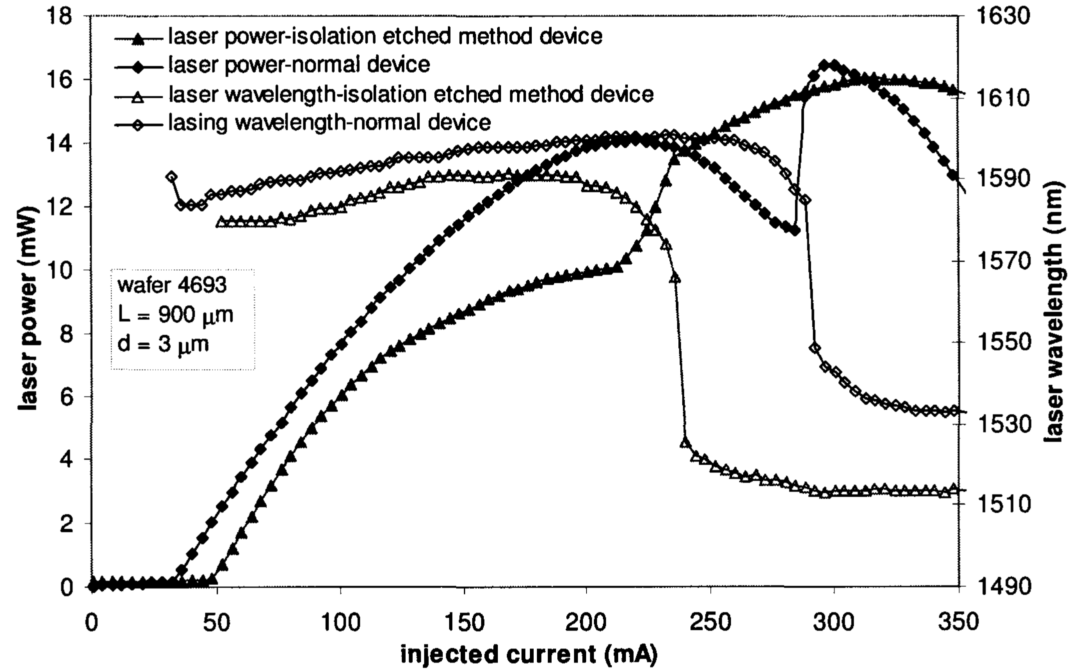

Figure 4.21: *Measured output power profile for normal device and IEM device 3 μm from the ridge (solid marks – left scale), and the laser first peak wavelength (hollow marks – right scale) as a function of injected current for 900 μm long, 4 μm ridge width, extended doping (ED) diode lasers.*

Chapter 5: Laser Application: Sub-Micrometer Resolution of Distance Measurements with a Broadly Tunable Short-External-Cavity AMQW InGaAsP/InP Diode Laser

5.1 Introduction:

In the previous chapters the low power output problem that is associated with AMQW ridge waveguide laser diodes was studied. Analysis of the power problem and solutions were presented. High power widely tunable laser diodes are beneficial in many applications, for example in industry where precise position identification is needed especially when the measurements are taken in a different medium than air. Another example for high power laser applications is in ranging and military equipment where it is necessary to achieve a good level of reflected signal especially when weather conditions are not ideal. Last but not least high power widely tunable lasers could be beneficial in speckle interferometers, to cover wider areas of the test samples. In all these applications a high power laser beam is needed. My application example in this chapter will be high resolution, absolute distance measurement. It is important to note that in the lab I used a cooperative target to do the experiment (mirrors in my case) but a real life setup may take different configurations.

Compact and non-contact measurements of absolute displacement with sub-micron resolution are of interest to industry, to military, to space, and to medical field applications. In the automotive industry, where machine vision is widely used, a compact, absolute measurement system solves many mechanical, technical and time consuming issues. The measurement of distance using a broadly tunable short-external-cavity (SXC) AMQW InGaAsP/InP diode laser in an optical interferometer is presented in this chapter. Absolute distance measurement with sub-micrometer resolution using a single laser source was reported which is, similar or better to the resolution obtained using the technique of wavelength multiplexing[99, 100, 101, 102].

Custom designed asymmetric multiple-quantum well (AMQW) lasers[11, 103] were used. The lasers were tuned using a diffractive optical element (DOE) in a short external cavity configuration[8, 98]

Our group designed spectrally broad diode lasers –see chapter 1 in this thesis– and we believed that the wide tunable range should be advantageous in certain applications. The motivation for this work was to determine the suitability of a single, widely tunable, DOE SXC AMQW laser in an optical interferometer for measurement of distance. Optical interferometers have been widely used in many industrial and medical applications. Interferometers are easy to construct and can be accurate in measuring distances. An unambiguous measurement of distance over a wide range of distance can be achieved by tuning the laser source between two or more wavelengths and using the differences of the phases of the interference fringes to extract the difference in path length between the two arms of the interferometer. The benefit of this multi-wavelength method is to eliminate the need to count fringes. In contrast to a fringe counting technique, the multi-wavelength approach allows for an interruption of the measuring sequence. Allowing interruption opens a range of industrial and medical applications.

Two techniques have been published to achieve measurement of displacement without ambiguity over differences in the arms of an interferometer from 1.2 m to 14.5 cm with resolutions better than several micrometers[100,101]. In this work I report measurement of the difference between arms of an interferometer with sub-micrometer resolution using a single, broadly tunable diode laser. It is show in this chapter that by using a non-linear least squares fitting technique we can extract the displacement (i.e., the difference in path length between the arms of the interferometer) from the raw data and compare this technique to the more common phase subtraction technique.

5.2 Theory of Operation

5.2.1 Single Wavelength Ranging Theory:

The output of a Michelson interferometer is given by[104]

$$I(\tau) = \left(K_1^2 + K_2^2\right) I_0 \left[1 + \frac{2K_1K_2}{K_1^2 + K_2^2}\mathrm{Re}\{\gamma(\tau)\}\right] \qquad \textbf{Eq. 5.1}$$

where $K_1^2\, I_o$ is the irradiance in one arm of the interferometer, $K_2^2\, I_o$ is the irradiance in the other arm of the interferometer, and $\gamma(\tau)$ is the complex degree of coherence of the light, with $|\gamma(\tau)| \leq 1$. The degree of coherence is a measure of the ability of the light to self-interfere. The fringe visibility of the interferometer is equal to $|\gamma(\tau)|$. The argument τ is the difference in propagation times for the light in each arm of the interferometer. Sources with narrow line widths, such as external cavity lasers, will have high degrees of coherence and will form fringes for large and small τ.

In the events that the irradiances in the two arms of the interferometer are equal (i.e., $K_1 = K_2$), and that the light from the source shows perfect coherence (i.e., $|\gamma(\tau)| = 1$), then the output of the interferometer is given by the simple equation

$$I(\tau) = I_{\circ}[1 + \cos(\phi(\tau))] \qquad \text{Eq. 5.2}$$

where $\phi(\tau)$ is the phase difference between the measurement arm and the reference arm and can be written as

$$\phi(\tau) = 2\frac{2\pi}{\lambda}(S_1 - S_2) = \frac{4\pi}{\lambda}S \qquad \text{Eq. 5.3}$$

S is the difference of the path lengths of the two arms, or the displacement, of the interferometer, λ is the wavelength in air of the light being used, and $\tau = 2nS/c$ with c/n the phase velocity of the light in the arms. Equations (5.2) and (5.3) demonstrate that the phase difference is a function of the wavelength and that measurement of displacements greater than $\lambda/2$ is restricted to counting fringes if only a single wavelength is used. Fringe counting during measurement of displacement means that any interruption to the measurement or any sudden changes in displacement of $> \lambda/2$ might introduce an error in the measured displacement. Since many applications introduce this type of interruption, a multi-wavelength technique has been developed[99-102].

Equation (5.2) also highlights the need to know accurately the value of the wavelength λ of the source for the interferometric measurement. All measurements of S are referenced to λ and hence can be no more accurate than λ. The vacuum wavelength $\lambda_v = \lambda n$. The refractive index of air n is a function of, *inter alia*, wavelength, air pressure, temperature, concentration of CO_2, and humidity[105]. Hence changes in the refractive index n will affect the accuracy of the measurement of S unless the changes are accounted for or unless λ is measured for the given conditions. The refractive index at a wavelength of 1.55 μm, a pressure of 103.250 kPa, a temperature of 20 C, a concentration of CO_2 of 450 ppm, and a relative humidity of 50% is estimated to be 1.000268148.

Table 5.1 gives the changes in the refractive index of air for changes in wavelength, pressure, temperature, concentration of CO_2, and concentration of water vapour at a wavelength of 1.55 μm. Changes in refractive index owing to changes in λ and atmospheric conditions limit the accuracy to roughly one part per million, unless the changes are taken into account. In this work the distances were << 1 m such that the uncertainty in displacement owing to the uncertainty in n was << 1 μm.

Table 5.1: *Changes in the refractive index of air at 1.55 μm owing to changes in wavelength, pressure, temperature, concentration of CO_2, and concentration of water vapour.*

independent variable	Δ independent variable	Δ n
pressure (101325 kPa)	1 kPa	2.65×10^{-6}
temperature (273.15 K)	1 K	-9.17×10^{-7}
wavelength (1.55 μm)	10 nm	-8.18×10^{-9}
CO_2 (450 ppm)	50 ppm	7.09×10^{-9}
relative humidity (0.5)	0.01	-8.73×10^{-9}

5.2.2 Multi-Wavelength Ranging

Measurements at multiple wavelengths can alleviate some of the difficulties associated with fringe counting and allow interruption of the measurement to occur without affecting the result of the measurement[102]. For the case of two wavelengths, the difference of the phase differences for λ_1 and λ_2 is of interest and can be written as

$$\Delta\phi = \phi_2(\tau) - \phi_1(\tau) = 2\left[\frac{2\pi}{\lambda_2} - \frac{2\pi}{\lambda_1}\right]S = \frac{4\pi}{\lambda_{12}}S \qquad \text{Eq. 5.4}$$

with $\lambda_{12} = \left[\dfrac{\lambda_1\lambda_2}{\lambda_1 - \lambda_2}\right]$

where λ_{12} is a synthetic wavelength, which is always larger than either λ_1 or λ_2. Since the synthetic wavelength is larger than either λ_1 or λ_2, the ambiguity distance has been increased. The smaller the difference between the two wavelengths, the larger the synthetic wavelength and, consequently, the larger is the ambiguity length, $\lambda_{12}/2$. However, the increase in ambiguity distance comes at the price of reduced resolution. The minimum detectable phase difference is directly related to the signal to noise ratio (SNR) of the measurement system. Williams[102] showed that the SNR can be improved by increasing the number of measurements to obtain an unambiguous range. Williams also showed that phase difference resolutions of better than $2\pi/100$ are possible. For the sake of demonstration, in this paper we assume the phase difference resolution to be $2\pi/100$.

For a two-wavelength system, the resolution will then be $\lambda_{12}/200$, or one percent of the ambiguity distance.

To achieve a sub-micrometer resolution for a two wavelength source with a mean wavelength $(\lambda_1+\lambda_2)/2$ of 1.55 μm requires a wavelength separation of $(\lambda_1-\lambda_2) > 12$ nm assuming that a phase difference of $2\pi/100$ can be detected. Notice that the wavelength separation to achieve sub-micrometer resolution will decrease if a mean wavelength of < 1.55 μm is used. However, for a wavelength separation of 12 nm and a mean wavelength of 1.55 μm, the ambiguity length is 100 μm. Thus with a two wavelength measurement system it is possible to measure unambiguously large distances but with reduced resolution. It is necessary to use more than two wavelengths to obtain both a high resolution and a large ambiguity length.

Most of the previous multi-wavelength work was done by using different wavelengths from different laser sources and hence the name multiplex wavelength interferometery. In the case that did use a single diode laser[99], the spectral tuning range of the laser was too short to achieve resolution in the sub-micrometer range. I report sub-micron resolution with a single diode laser with a tuning range of > 100 nm when operated in a diffractive optical element short external cavity.

The basic principle of wavelength multiplexing is described in reference [102]. Wavelength multiplexing depends on taking measurements of the phase difference for multiple wavelengths of the source for the interferometer for each unknown displacement. Assume that four measurements are taken at four wavelengths λ_1, λ_2, λ_3, and λ_4. If λ_1 is the longest wavelength then it would be considered the reference measurement. The separation between the wavelengths is determined by the targeted absolute distance (i.e., the ambiguity distance) that is to be measured and the resolution that is desired. Subtracting each measurement of the phase difference ϕ from the reference measurement at λ_1 yields the value of $\Delta\phi$. According to Eq. (2) $\Delta\phi$ will give the displacement S between the two arms. Careful choice of the differences of wavelengths (λ_1–λ_i) will lead from a large ambiguity length and low resolution to a large ambiguity length and a high resolution. When the value ($\lambda_1 - \lambda_2$) $\leq$ 0.1 nm and (λ_1+ λ_2)/2 = 1.55 μm, then the ambiguity length will be > 12 mm, which is equal to a phase difference of 2π. On the other hand the resolution will be low which can be improved by calculating a second phase difference by using (λ_1–λ_3) equal to a couple of nanometers. The only factor that determines the value (λ_1–λ_3) is the resolution of the previous measurement. The ambiguity length of the second measurement should be slightly larger than the resolution of the first measurement. By doing so, the over all measurement will have the same resolution as the last measurement, which should be better than the resolution of the first measurement. To increase further the resolution, a third phase difference by using the data from (λ_1–λ_4) is needed. Again the only factor that determines the value of (λ_1–λ_4) is the last resolution achieved. By choosing a wavelength difference of 100 nm for (λ_1–λ_4), the over all measurement of distance will maintain the original long ambiguity length and will preserve the latest resolution, which will be better than 0.3 μm. In short, the wavelength multiplexing method will achieve a long ambiguity length determined by the tuning range of the single diode laser. Once all these calculations are completed, one data point for one object position with high resolution will be established. As a result, the wavelength multiplexing method will be able to determine the absolute displacement and the only limits to this method are the range of wavelengths that are available and the accuracy to which the phase difference can be determined.

In short, the goal of the wavelength multiplex method is to pick the wavelengths such that only one solution to the multi-valued inversion of Equation. (5.2) is available.

5.2.3 Cosine Fitting Method:

Another approach to determining the displacement *S*, and one which I report here[9], is to fit a harmonic function to the data and to use a best fit parameter to estimate *S*. It appears that the best fit method allows for extraction of meaningful estimates of *S* in the presence of noise. A plot of the output of the interferometer as a function of wavelength shows the characteristic fringes with period equal to the displacement *S*. With the broadly tunable laser that we employ in the DOE SXC, we can obtain measurements over a broad range of wavelengths and hence measure the output as a function of wavelength.

The displacement S was extracted from the data by using a non-linear Marquardt[106] algorithm to minimize χ^2

$$\chi^2 = \sum_{i=1}^{N} \left(y_i - y(\lambda_i)\right)^2 \qquad \text{Eq. 5.5}$$

where y_i are the measured outputs of the interferometer for a monochromatic input at a wavelength of λ_i and $y(\lambda_i)$ are the values of the nonlinear function calculated as

$$y(\lambda) = a_1 + a_6(\lambda - 1500) + [a_2 + a_5(\lambda - 1500)]\ \cos\left(\frac{4\pi a_3}{\lambda} + a_4\right) \qquad \text{Eq. 5.6}$$

The uncertainty for a single measurement was not independently estimated. This uncertainty was estimated from the variance of the fit as the minimum value of $\chi^2/(N-m)$ where N was the total number of data points and m was the number of fit parameters[107]. The uncertainty of the displacement that was extracted from the data was taken as twice the square root of the product of the value of the appropriate element of the error matrix and the variance of the fit $\chi^2/(N-m)$. The factor of two gives a confidence level of approximately 95%, assuming that the uncertainties followed a normal distribution.

The dc offset and amplitude of the harmonic function were allowed to be functions of wavelength to account for any wavelength dependence in the optical components of the interferometer. The inclusion of these terms improved the fits in that the values of χ^2 were reduced and the visual qualities of the fits were improved. The inclusion of these terms reduced the number of degrees of freedom for the fit and these terms could be excluded at a loss of accuracy in the determination of S. If these terms were not included in the fit, the accuracy in the determination of the displacement S changed from 0.05 μm to 0.35 μm when the terms were excluded.

The Whittaker-Shannon sampling theorem can be used to determine the minimum number of points required to make an unambiguous measurement of S[108, 109]. Provided that there are slightly more than two samples per period of the harmonic function, i.e., provided that the sampling rate is slightly higher than the Nyquist rate, then it should be possible to recover *S* from measurements made at a finite number of wavelengths. The resolution with which *S* can be determined will depend on the total number of measurements that are made. This point is demonstrated with the experimental data by fitting to every n^{th} data point.

The sensitivity of the fit to changes in the displacement *S* is demonstrated in Figure 5.1. Figure 5.1 shows simulated data for displacements of the interferometer arms of 30.0, 30.1, 30.2, and 30.3 μm over a range of wavelengths of 100 nm, a range of wavelengths that can be obtained with the DOE SXC laser. Figure 5.1 clearly shows that a 0.1 μm change in the displacement presents a discernable change in the output of the interferometer as a function of wavelength.

5.3 Experimental Setup

The performance of multi-wavelength absolute laser ranging using single laser sources was investigated by using a custom designed and fabricated (wafer #4381) broadly tunable InGaAsP/InP diode laser[103,8]. The custom designed laser was used with uncoated facets and has a compositionally asymmetric multiple quantum well (AMQW) active region that consists of five compressively strained, 100 Å thick quantum wells. This custom designed laser can be tuned in excess of 100 nm, which is needed for this application. Conventional uncoated multiple quantum well (MQW) lasers, where the QWs are nominally of the same composition and thickness, can be tuned over only 40-50 nm[11, 98] under the same conditions as the custom designed AMQW lasers. The laser was designed[14] and fabricated using the growth and fabrication facilities at McMaster

University. The diode laser was tuned by a diffractive optical element (DOE) short-external-cavity (SXC) as described in reference [98]. The DOE SXC allowed single longitudinal mode operation on each mode within the > 100 nm tuning range of the lasers. The modes were not necessarily accessed in a sequential fashion and as a result typically four measurements of the output of the interferometer were made for each wavelength corresponding to a given longitudinal mode of the diode laser. The cavity length of the diode laser was 850 μm, which gives a mode spacing of 0.5 nm.

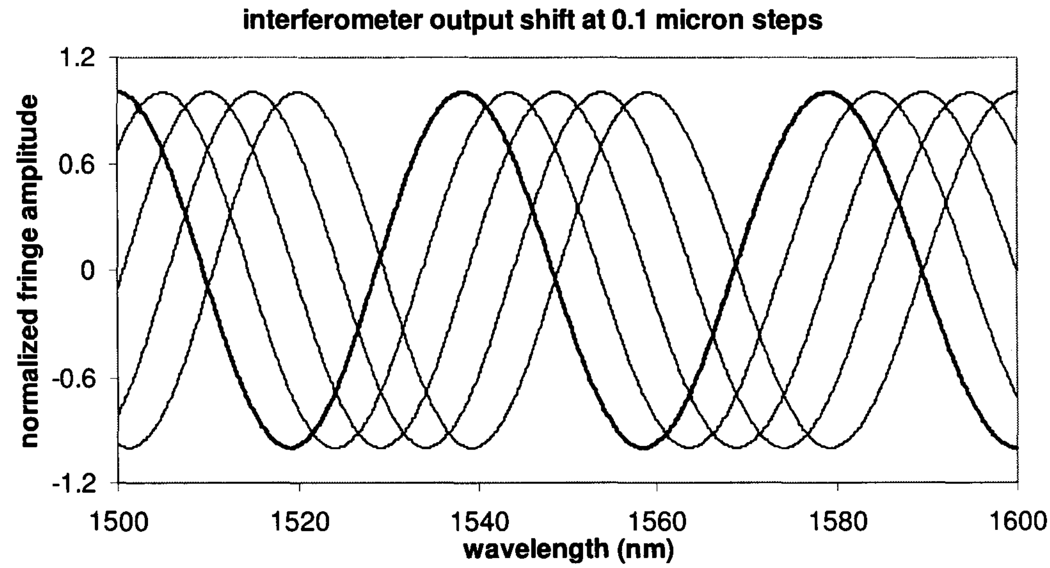

Figure 5.1: *Simulation of the output of the interferometer for displacements that differ by 0.1 μm. The thick line is for a displacement of 30 μm.*

A schematic diagram of the experimental set-up is shown as Figure 5.2. Selection of the mode of operation of the DOE SXC laser, and hence the wavelength of operation of the distance measuring interferometer, was achieved by moving the DOE along the optical axis of the laser using a BEI linear actuator [LA10-12-027A] in a flexure mount. The output of the diode laser was collimated with a lens (hence the interferometer was more of a Twyman-Green interferometer than a Michelson interferometer[110]) and passed through a beam splitter (BS1). Part of the beam went to an HP86120C multi-wavelength meter, which has an accuracy of ±2 ppm (±0.003 nm) for the wavelengths that were used. The rest of the collimated beam passed through a second beam splitter (BS2) where part of it went to a reference detector and the remainder went to the nominally 50/50 beam splitter (BS3) of the interferometer. The collimated beam was split by BS3 into the two arms of the interferometer where the reference beam went to the reference mirror (M2) and the signal beam went to the object. The object could be moved in three orthogonal directions using a 3D translator stage. Both of the beams were reflected from reference and object mirrors and were combined at the fringe detector. A chopper was inserted before the fringe detector and referenced a lock-in amplifier for phase sensitive detection. The reference detector and the output of the lock-in amplifier were connected to a HP-54600A digital oscilloscope and to a computer for data acquisition. The temperature of the laser was controlled by a thermo-electric cooling stage. A path length difference S in the interferometer arms was introduced by moving mirror M1. The distance that M1 was moved was recorded with an Oriel Motor-Mike controller [18008] display and by counting fringes from the diode laser. The fringes were counted manually and have an estimated uncertainty of one fringe.

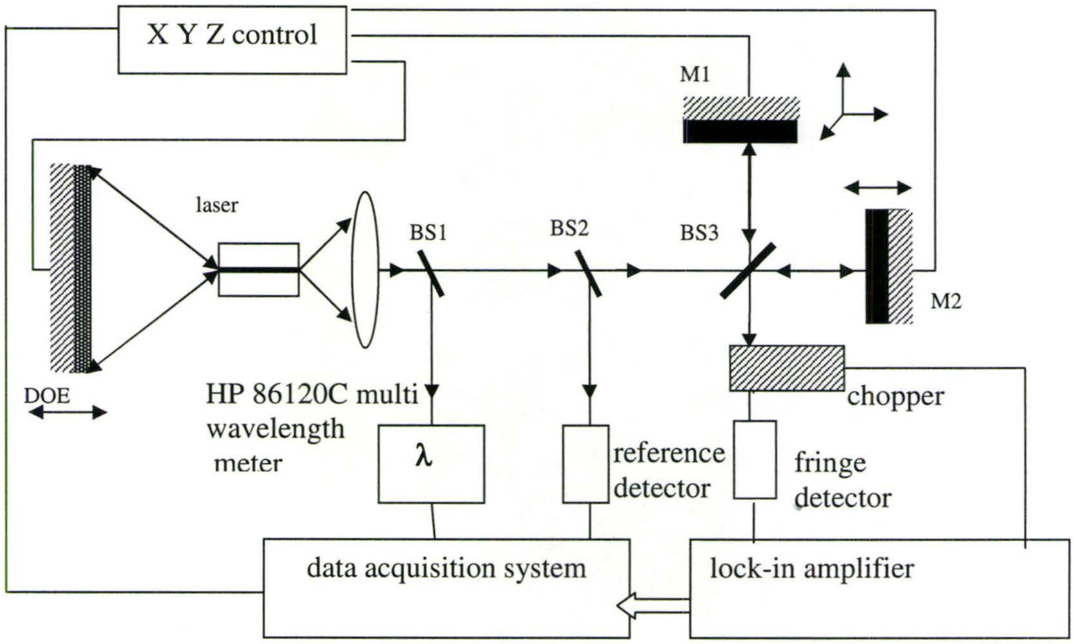

Figure 5.2: *Schematic diagram of the experimental setup. The DOE reflecting the light to one facet of LD and the tuned light collected from the other facet.*

5.4 Results and Discussion

Data from two experiments were taken to verify both the phase subtracting and the cosine fitting methods. The first experiment yielded poor estimates of the displacement when using the phase subtracting method owing to the noisy signals. Consequently the accuracy of the measurements of displacement using the phase subtraction signal was several micrometers.

The second experiment was done using the same DOE SXC AMQW diode laser. However, this time measurements were made over a greater number of modes, and the data were analyzed using a least squares fit of a harmonic function to the data. Figure 5.3 shows the output of the interferometer as a function of wavelength for a displacement considered to be the zero position and the best fit line to the data. The figure clearly shows a noisy harmonic signal. The noise is the reason for the poor accuracy that was obtained when the data was analyzed by the method of phase difference. The raw data does show the harmonic function nature of the wavelength dependence. This permits the displacement *S* to be extracted by fitting a harmonic function to the data. The parameter *S* was extracted through a non-linear least squares fit, yielding 23.4 ± 0.05 μm as the displacement *S* of the interferometer arms.

To determine the number of raw data points that is required to determine *S* and the accuracy with which *S* can be determined, we performed fits using only fractions of the total number of the raw data points. Every 2nd, 4th, 8th, 16th, 32nd, 64th, 128th data point were taken and the function was fit to these sets of data. The extracted displacement *S* and the resolution for the number of points in the fits are presented in Table 5.2. A decrease of the resolution to 0.55 μm from 0.05 μm was found as a result of fitting to 7 data points instead of all 989 data points. The data in table 5.2 shows that fitting to one eighth of the data points will cause the resolution to decrease to 0.16 μm. Figure 5.4 shows samples of the fits for 123, 30, 15, and 7 data points. This is an important result since the number of data points required for a given resolution directly affects the time required to obtain the data. The trade off is higher resolution versus a slower measurement of displacement.

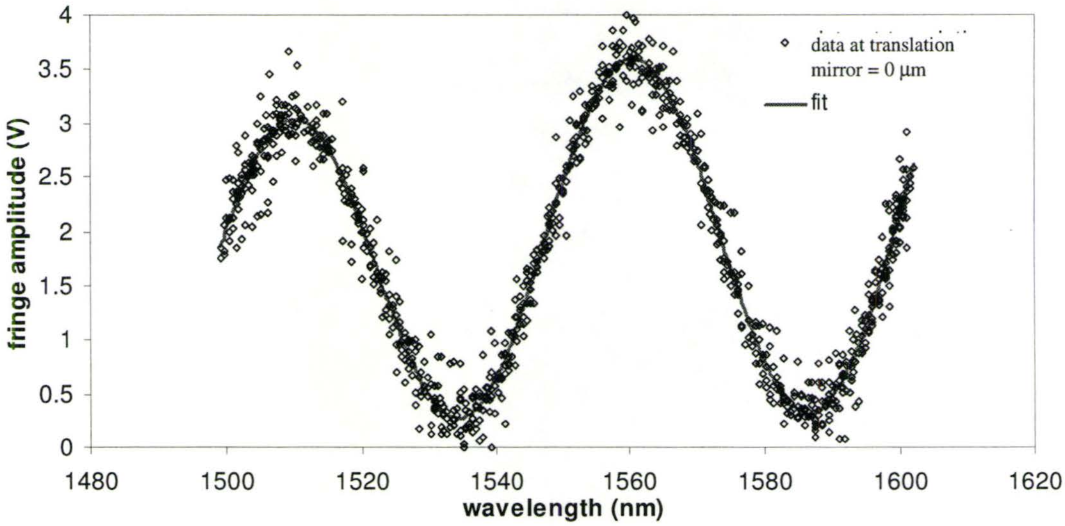

Figure 5.3: *The raw data and the best fit line for all the 989 data points of the scan for a displacement near zero. The data preserved the cosine function and the extracted S parameter from the best fit line was 23.4 ±0.05 μm.*

Table 5.2: *Extracted displacement S and resolution for different number of data points used in the fit.*

# raw data points used in the fit	Extracted S (μm)	Resolution ± (μm)
989	23.39	0.05
495	23.34	0.07
247	23.33	0.11
123	23.42	0.16
30	23.38	0.28
15	23.4	0.50
7	22.99	0.55

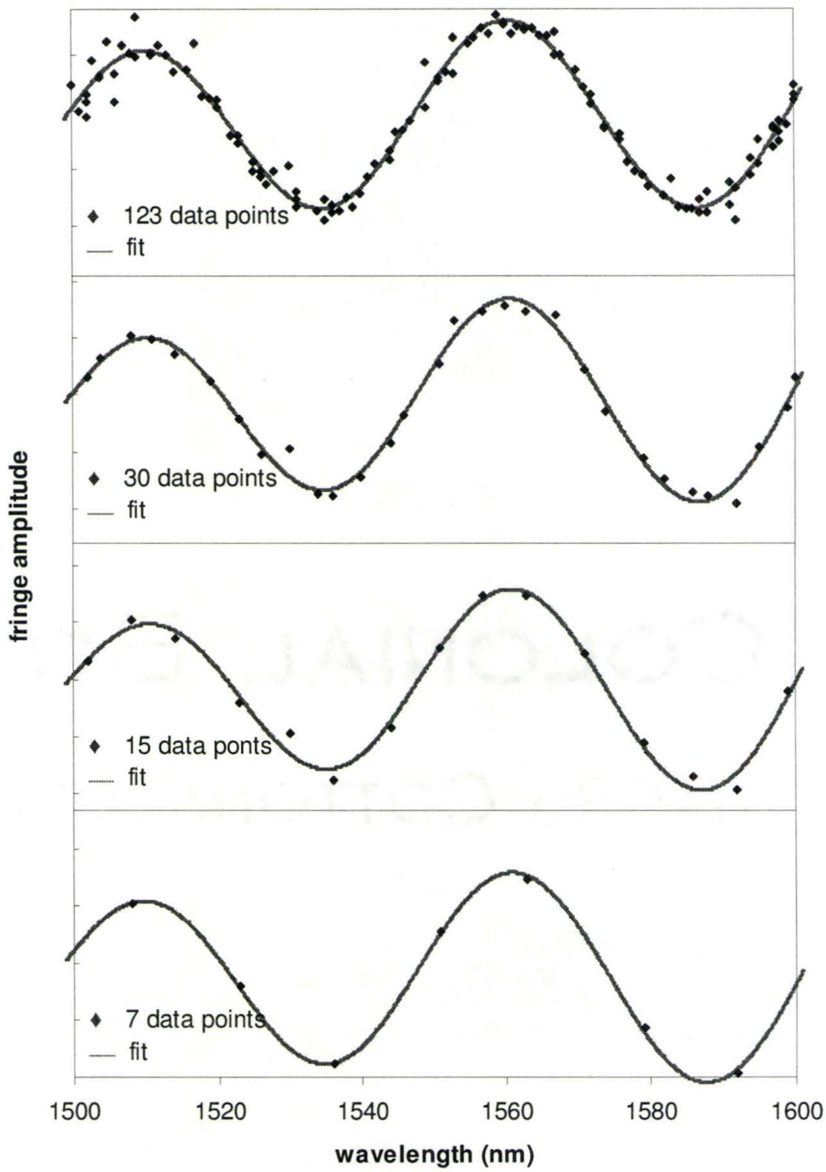

Figure 5.4: *Lines fitted to 123, 30, 15, and 7 data points. The resolution of the displacement S changed from 0.05 to 0.55 μm when changing the number of points from 989 to 7.*

Measurements were made for relative displacements of mirror M1 for 20, 40, 60, 80, 100, 200 and 400 μm. The raw data and the best line fits for the raw data are plotted in Figure 5.5. The displacements of the arms of the interferometer were extracted from each fit and the difference between the smallest displacement (actuator display = 0) and an extracted displacement yield the measured distance that the mirror was moved. The results from these measurements are presented in Table 5.3. The column labelled discrepancy is the value of the actuator display minus the measured distance. The measured distance showed sub-micrometer accuracy as compared to the actuator display and was within the estimated experimental uncertainty.

Table 5.3: *Comparison of the measured distance and the actuator display.*

actuator display (μm)	Fringe counting (μm)	*S* from the fit (μm)	resolution ±(μm)	measured distance (μm)	discrepancy (μm)
0	0	23.385	0.05	0	0
20	19.7	43.383	0.06	19.998	0.002
40	40.5	63.426	0.06	40.041	0.041
60	60.7	83.361	0.06	59.976	0.024
80	80.3	103.41	0.06	80.025	0.025
100	100.5	123.4	0.06	100.015	0.015
200	201.2	223.35	0.06	199.965	0.035
400	401.3	423.41	0.06	400.025	0.025

This method can be useful also in other applications rather than distance measurements. For example it can be used in a surface profiler setup to give accurate surface topography with better than 0.1 μm resolution in a non-contact way. Also it can be used in medical imaging like optical coherence tomography (OCT).

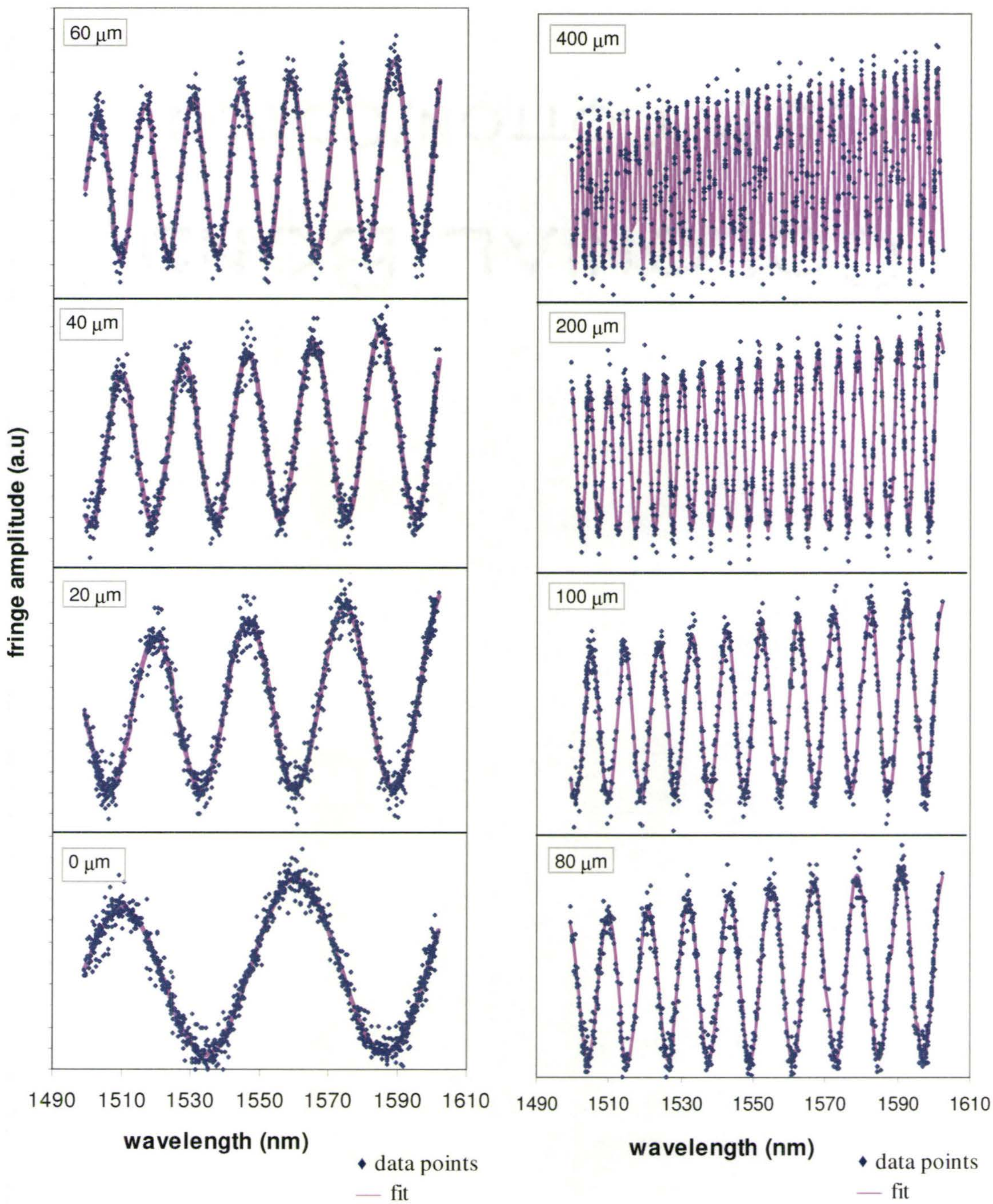

Figure 5.5: *Raw data and the best fit lines for translations of mirror M1 of 0, 20, 40, 60, 80, 100, 200, and 400 μm.*

Chapter 6

Laser Diode (LD) Fabrication Process

Optimizing the fabrication process from scratch is a very lengthy process which takes time and resources. In this chapter I present step by step how to fabricate the AMQW ridge waveguide lasers. The fabrication process starts after receiving the grown wafer from the epitaxial growth facility. The wafer goes through a cleaning process as a first step and then goes through the steps of fabricating the ridge and through the metallization steps at the end. Before starting any of these processes all personnel involved in the fabrication process have to go through all clean room training and safety programs. Also, all personnel involved in the using the clean room equipment have to be trained and read the safety reports for each machine they will operate.

[Note: All the drawings in this chapter are not to scale. The drawings show one laser diode only as a representation for the whole wafer. The finished wafer contains several hundred similar laser diodes].

6.1. Wafer cleaning process:

This step is necessary to remove surface contamination on top of the wafer. The steps of this process are as follows:

1. Blow dry wafer with pure nitrogen (N_2) dry gas.
2. Soak wafer for 10 minutes in trichloroethylene.

3. Soak wafer 10 minutes in methanol.
4. Rinse wafer in de-ionized (DI) water for 5 to 10 minutes.
5. Blow dry wafer with an N_2 gun.
6. UV ozone clean for 10 minutes.

[HF solutions are very hazardous to the human body. Refer to HF safety courses before dealing with HF solutions. Use teflon beakers only when you use HF solution].

7. Soak the wafer in premixed buffered oxide etch (BOE) for 2 minutes at room temperature. [**Note:** *For good process control an etchant called buffered oxide etch (BOE) is used to etch thin films of silicon dioxide (SiO_2) or silicon nitride (Si_3N_4). It is comprised of a mixture of a buffering agent, such as ammonium fluoride (NH_4F), and hydrofluoric acid (HF). The buffered oxide etch solution that I used comprised a 10:1 volume ratio of 40% NH_4F in water to 49% HF in water*].
8. Rinse with DI water for 10 minutes.
9. Blow dry wafer with an N_2 gun.

6.2. Ridge fabrication steps:

After the wafer is cleaned a masking material is deposited on the top surface of the wafer; see Figure 6.1. The most common masking material used in the semiconductor industry is SiO_2; however SiN, SiN_xO_y, AlN, and Al_xON_y can also be used as masking material. For our process we use SiO_2 for masking to pattern the ridge. To deposit the SiO_2 layer refer to the CVD deposition system instruction sheets in the clean room. Use settings of 90 sccm for Silane (SiH_4) and 70 sccm for nitrous oxide (N_2O). Wait until the plate temperature reaches 300 °C, and then use 50 W as the deposition power and deposit 1300-1500 Å of SiO_2. Refer to the CVD log book for the deposition rate. After cooling down the CVD chamber and removing the wafer, use an ellipsometer to measure the SiO_2 film thickness and index of refraction. Make sure that both readings are within the range and keep a record of the film thickness.

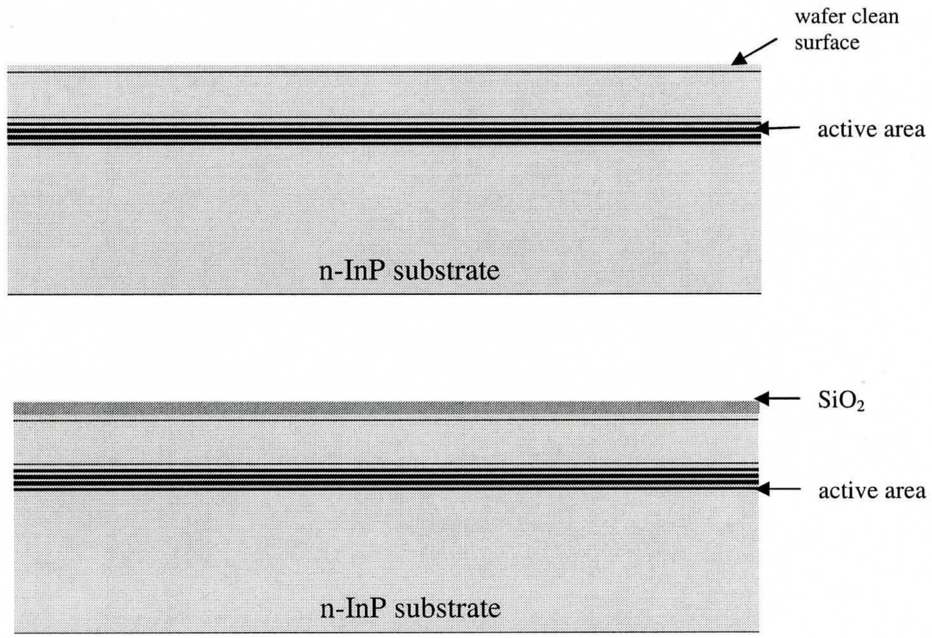

Figure 6.1: *Wafer after the cleaning process (top), and wafer with deposited SiO_2 thin film (bottom).*

After depositing the SiO_2 masking layer follow the steps below to form the ridge waveguide structures.

6.2.1. Ridge Patterning:

6.2.1.1 Photolithography:

1. Spin primer at a speed of 4000 rpm for 30 s. Use MicroPrime from Shin-Etsu. Micro Si Company.
2. Set the wafer on microscope glass slides on top of a hot plate covered with a Pyrex dish and bake for 2 minutes at 110 °C.
3. Spin positive photo-resist (PR) at a speed of 4000 rpm for 30 s on the surface of the wafer. Use S1808 (PR) from Rohm Haas Electronic Materials.
4. Set the wafer on microscope glass slides on top of a hot plate covered with a Pyrex dish and bake for 2 minutes at 110 °C.
5. Clean the mask with the following solutions in sequence: acetone, methanol, and DI water then dry with an N_2 gun.
6. Refer to the mask aligner procedure sheet. To find out the exposure time on the mask aligner raise the wafer holder, expose, and then read the power as *X*. Use the following formula to find the exposure time $t_{\text{exp}} = \dfrac{30}{X}$ s. Set the exposure time on the mask aligner.
7. Load the mask to the mask aligner after choosing the right pattern (mesa pattern) and load the wafer to the wafer holder. Coarse align the wafer so that the mesa will be aligned perpendicular to the major flat of the wafer.

8. Follow the instructions in the mask procedure to fine align the wafer to the mask and then expose the wafer using the exposure time calculated in step 7 (see Figure 6.3 top).
9. Slowly remove the wafer from the mask aligner and move it to the wet bench.
10. Mix 1 part developer (351 developer for the S1808 PR) to 5 parts DI water in a beaker.
11. Develop the PR on the wafer for 26 seconds in the developer mixture. In this step time is very critical so after the 26 seconds remove the wafer quickly and place it in a flow of DI water for 2 minutes.
12. Blow dry the wafer with an N_2 gun and make sure that the direction of the gas flow is the same direction of the mesas.
13. Examine the wafer under a high power optical microscope (see Figure 6.3 bottom). Make sure that all the mesas are clear and that the PR is cleared from the field. If the mesas are not clear or the field contains a PR residue then re-develop for 3 seconds maximum and re-examine the wafer again. Note: redevelop for a maximum of 3 times. If the mesas are not clear then strip the PR and clean the wafer and repeat all the photolithography steps above.
14. If the mesas are clear and the field is clean then hard bake the wafer on the hot plate for 2 minutes at 130°C.

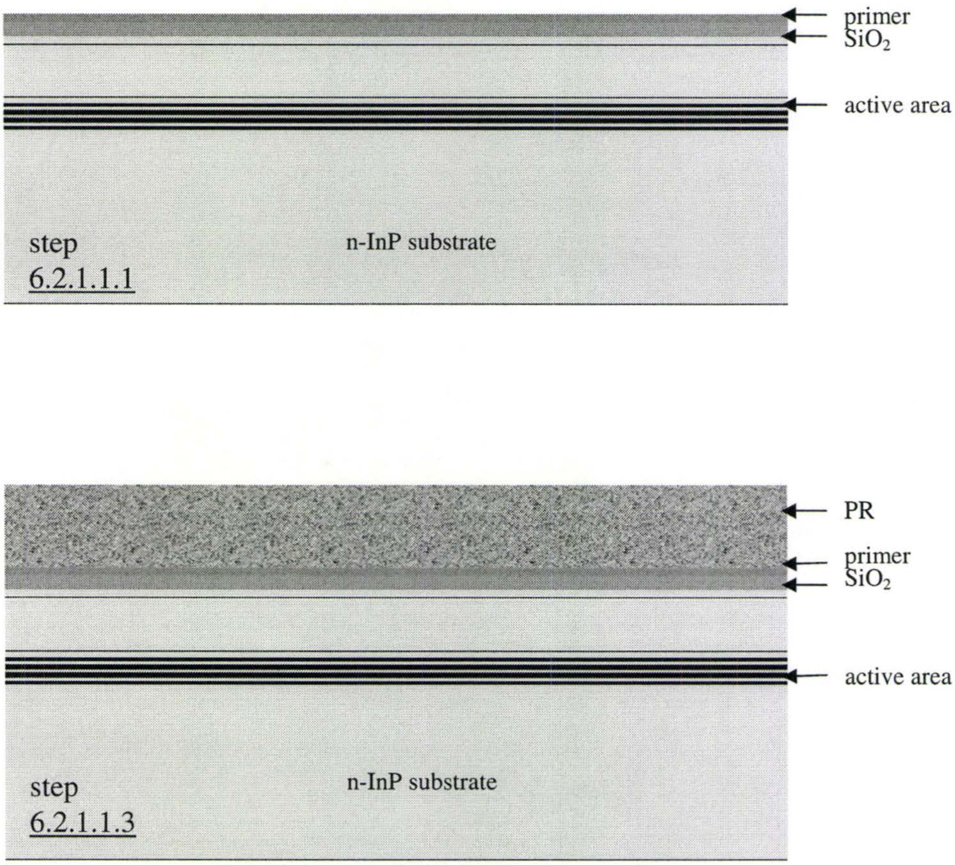

Figure 6.2: *Depositing primer (top) and photo-resist (bottom) by spinning and baking after each step.*

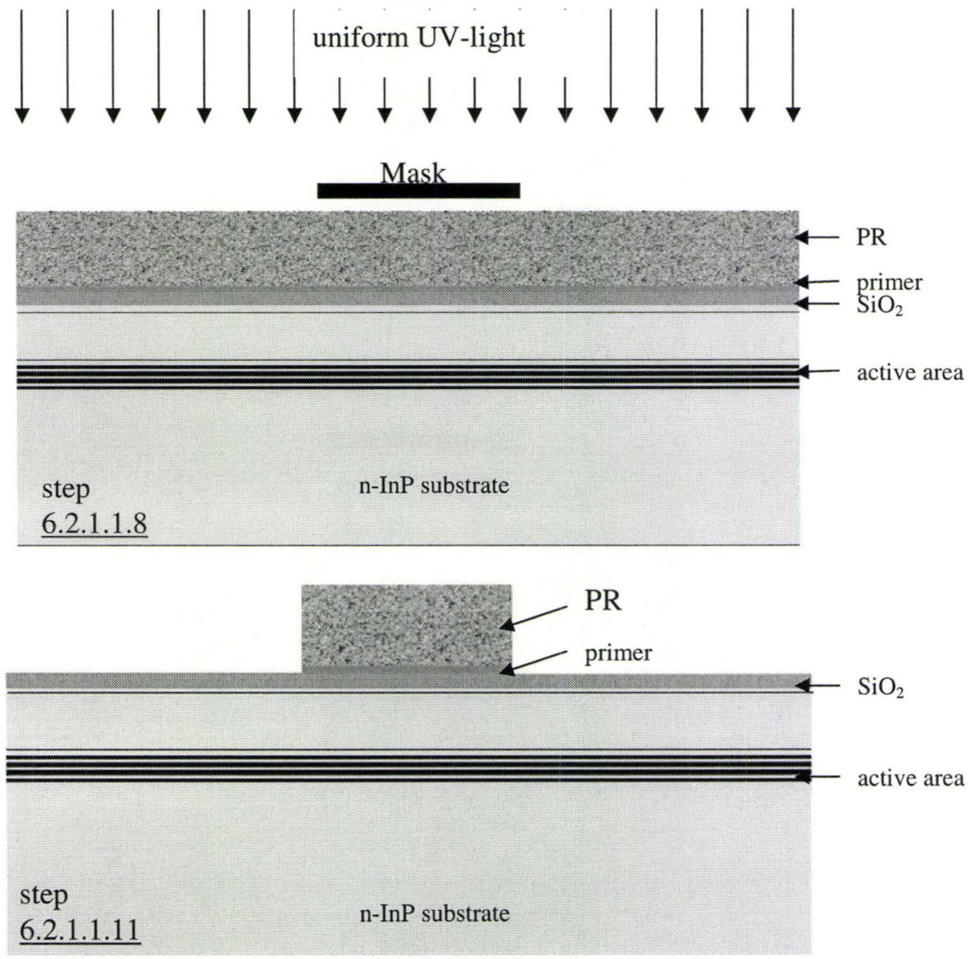

Figure 6.3: *Wafer aligned under the mask with the mask aligner, exposed with UV light (top), and then developed with 351developer and DI water mixture 1:5 (bottom).*

6.2.1.2 Etching the mask layer (SiO_2 Layer):

[HF solutions are very hazardous to the human body. Refer to HF safety courses before dealing with HF solutions].

1. Use an etch rate of 1000 Å/minute to find the etch time of the SiO_2 film.
2. Put enough quantity to cover the wafer of premixed BOE solution in a teflon beaker.

3. Set up your stop-watch to the desired etching time, open the DI water and let it flow in a Pyrex dish.
4. Use Teflon tweezers to hold the wafer and soak it in the BOE for the desired etch time. When time finishes remove the sample very quickly and soak it in the running DI water for 5 minutes.
5. Blow dry the wafer with an N_2 gun and check the wafer under a high resolution microscope (see Figure 6.4 top). Make sure that the SiO_2 is cleared from the field and there is no color graded areas especially in the middle of the wafer.

[**Note:** *Most of the time there are colour graded areas at the edges of the wafer which do not cover much of the device area. Trying to over etch to remove the SiO_2 from these areas will reduce the mesa width and damage the straight edges. Use your judgment in this situation*].

6.2.1.3 <u>Stripping the PR:</u>

To strip the PR submerge the wafer in acetone for 4 minutes then methanol for another 4 minutes then rinse the wafer with DI water for 5 minutes (see Figure 6.4). This step is necessary before the wet etching of the ridge structure because the PR and primer can contaminate the InP etching process.

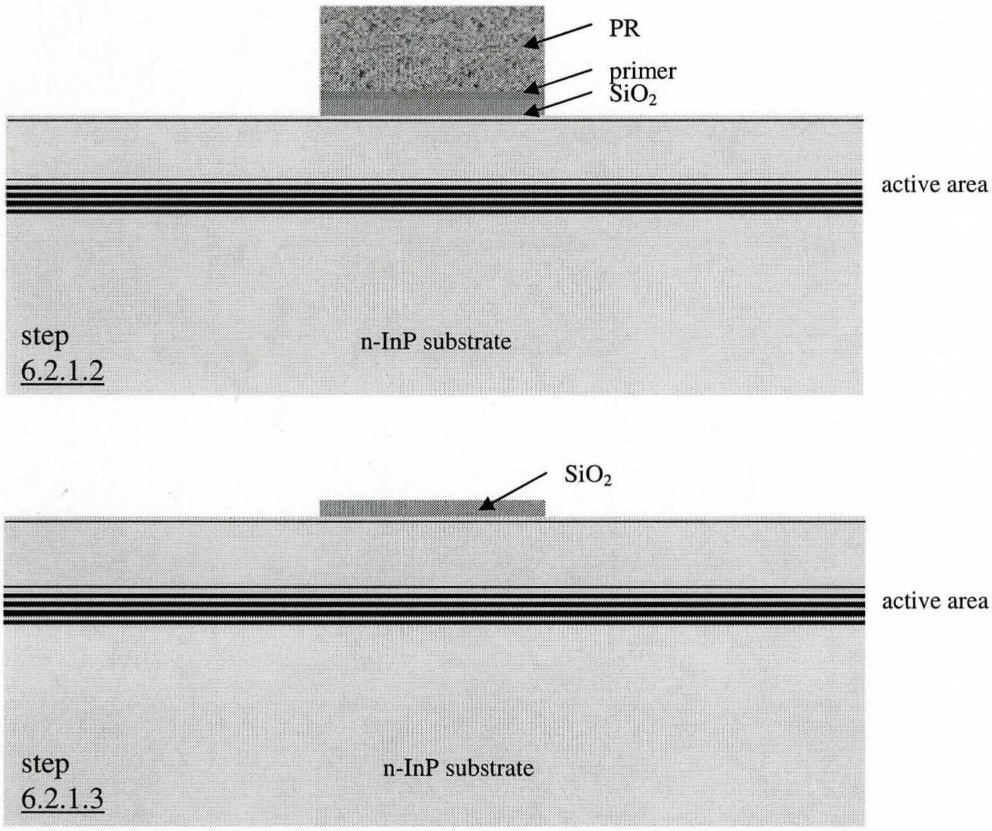

Figure 6.4: *Etching the SiO_2 layer using premixed BOE (top) and stripping the PR layer using acetone, methanol, and DI water (bottom).*

6.2.2. Etching the Ridge waveguide:

6.2.2.1 Etching the Contact layer (InGaAs)

1. Clean a beaker with glassware soap and DI water and mix the solution H_2SO_4:H_2O:H_2O_2 as 1:80:8 parts by volume in the beaker.
2. Remember to start with 80 parts H_2O add the 1 part acid H_2SO_4 and then add the 8 parts H_2O_2.

3. Use an etch rate of 4000Å/min and set up your stopwatch for the desired etch depth. Soak the wafer in the solution and etch for the desired time. Immediately rinse the wafer in DI water for 5 minutes after the etching time finishes.
4. Blow dry with an N_2 gun and examine under a high power microscope (see Figure 6.4 top).

6.2.2.2 Etching the Cladding layer (InP)

1. Clean a beaker with glass ware cleaner if necessary then mix the solution H_3PO_4: HCl as 3:1 parts by volume.
2. Remember to start with 3 parts H_3PO_4 then add the 1 part HCl.
3. Stir the mix to make a homogenous solution.
4. Use an etch rate of 4000Å/min and set up your stopwatch for the desired etch rate. Soak the wafer in the solution and etch for the desired time. Usually the wafer will start to bubble when it submerged in the mixed solution. When the bubbles stop forming the exposed InP material is etched away. Continue to etch for 20 s after the bubbles stop forming. Immediately remove the wafer from the etching mix and rinse it in DI water for 5 minutes.
5. Blow dry with an N2 gun and examine under a high power microscope (see Figure 6.4 middle).

6.2.2.3 Removing the Mask layer

To remove the SiO_2 layer just submerge the wafer in premixed BOE for 4 min and rinse the wafer in a flow of DI water for 5 minutes. Blow dry the wafer with an N_2 gun and examine under a high power microscope. The wafer should not have any SiO_2 residue.

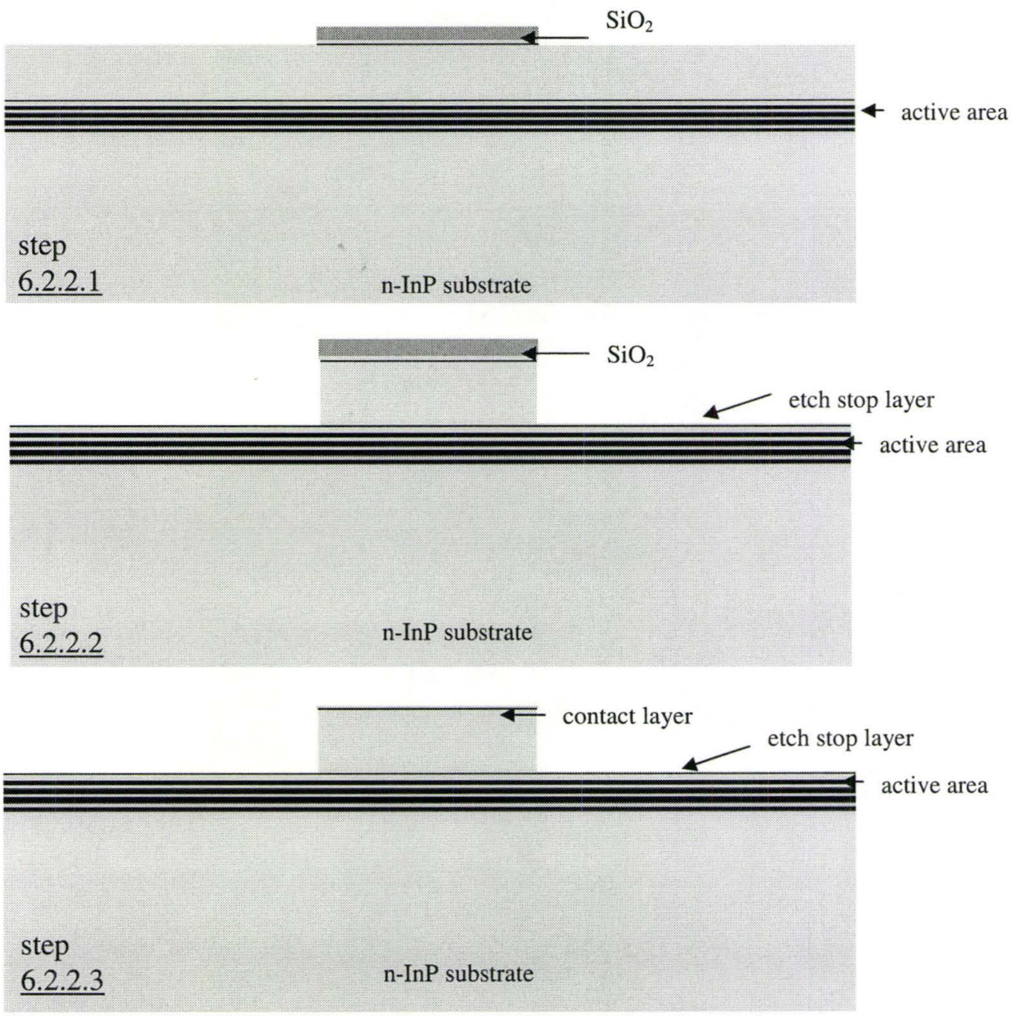

Figure 6.5: *The wafer after etching: the contact layer (top), the cladding layer (middle) and the SiO_2 layer (bottom).*

6.3. Isolation etch method:

[Note: skip this section and go to Sec. 6.4 if you don't want IEM devices]

This section is used to fabricate devices with IEM. See Chapters 3 and 4 to find more information about IEM devices. To fabricate devices with IEM on the wafer follow the steps below.

6.3.1. Deposit 1200 Å thick SiO_2:

Follow the SiO_2 deposition procedure detailed in Sec. 6.2 to deposit 1200 Å of SiO_2 see Figure 6.6.

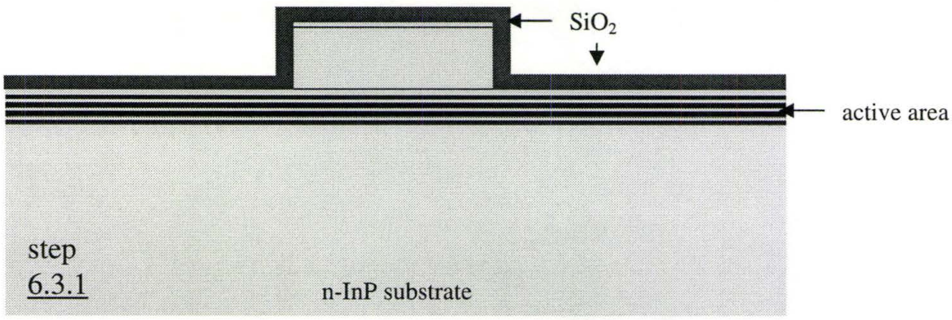

Figure 6.6: *Wafer after depositing SiO_2 for IEM. The SiO_2 film covers all three sides of the ridge.*

6.3.2. IEM patterning:

Follow the photolithography steps in Sec. 6.2.1.1 steps 1-13 but this time use the ISO pattern in the mask in step 7 (see Figure 6.7).

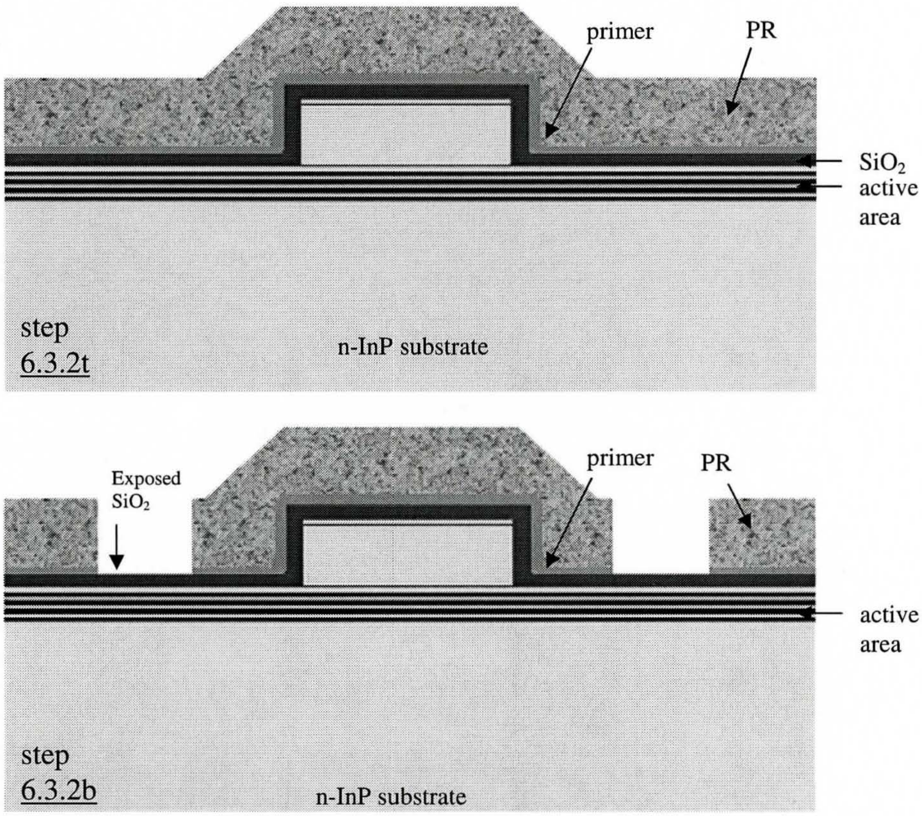

Figure 6.7: *Wafer after photolithography processes to pattern for IEM. The wafer after depositing primer, PR (top) and then the wafer after exposing and developing the PR (bottom).*

6.3.3. IEM opening:

1. To remove the SiO_2 from the trench areas follow the steps detailed in Sec. 6.2.1.2. Make sure not to over-etch the SiO_2 because over-etching will undercut the SiO_2 under the PR and make the etched trench closer to the ridge sides than anticipated (see Figure 6.8 top). Examine the wafer under a high power microscope and make sure that all the SiO_2 is removed from the trench area.

2. Follow the steps in Sec. 6.2.1.3 to strip the PR and then examine the wafer under a high power microscope (see Figure 6.8 bottom). Trenches, which indicate no SiO_2, should be seen around both sides of the ridge.

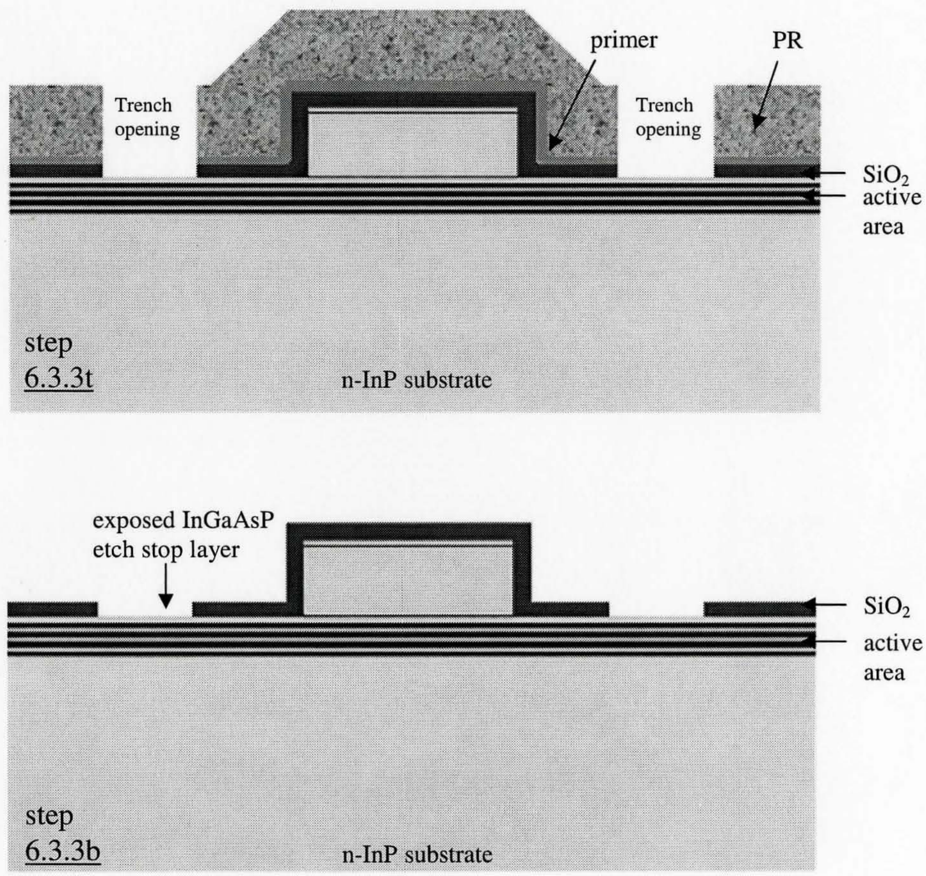

Figure 6.8: *The wafer after opening the trench for IEM (top), and after stripping the PR (bottom)*

6.3.4. Etching the trenches through the active region using ECR-RIE:

To etch the trenches through the active area use ECR-RIE. Refer to the user instruction sheet to use the ECR-RIE. Follow all safety procedures and issues when using the ECR-RIE system. To etch the trenches follow the steps below:

1. Use the gases CH_4:H_2:Ar with the following ratios 4:16:7.6 sccm.
2. Use a pressure of 10 mTorr as an etching pressure.
3. Use an RF Power of 200 W. Start with 20 W then increase the chamber pressure from 10 mTorr slowly until the plasma starts glowing then increase the RF power to 200 W. Set the pressure back to 10 mTorr.
4. Use a microwave power of 100 W. [Notice that this power is different from the RF power and you need both to run the etching mechanism].
5. Use an etch rate of 223Å/min to determine the etch time.
6. Etch for the desired time then follow the system instruction sheet to clean the sample from polymers and then power down the system.
7. Follow the system instruction sheet to remove the wafer from the system.
8. Examine the wafer under a high power microscope (see Figure 6.9 top). There might be some roughness in the trench surface due to dry etching which can be smoothened by submerging the wafer in an InP etchant for 30 seconds.
9. To remove the SiO_2 mask submerge the wafer in BOE for 5 minutes and then rinse with DI water for 5 minutes.
10. Blow dry the wafer with an N_2 gun and examine the wafer under a high power microscope.

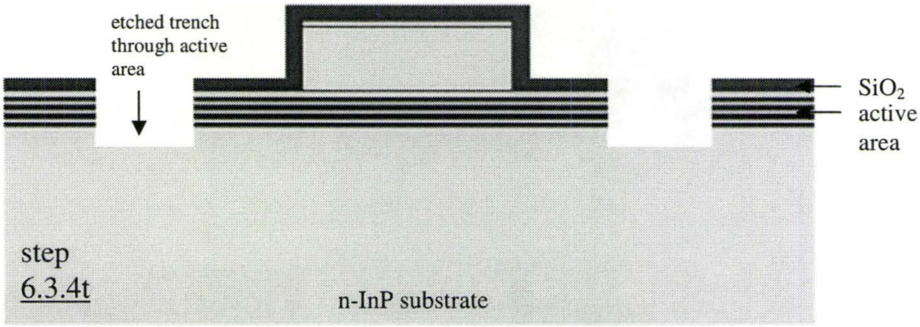

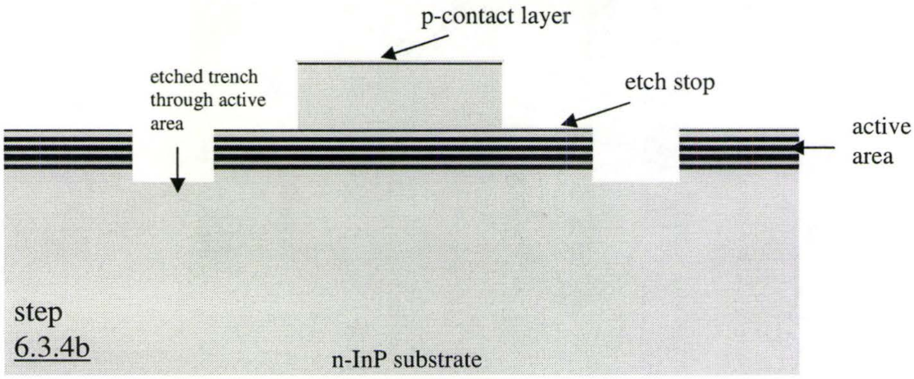

Figure 6.9: *The wafer after dry etching the trenches using an ECR-RIE system (top) and after removing the SiO_2 mask layer (bottom).*

6.4. Via opening:

The via is an opening on the insulator layer on top of the RWG to achieve a continuous contact between the p-metallization and the contact layer on the top of the ridge. The rest of the insulator layer insulates the laser diode surface from the p-metallization so the current injection is happening only from the top of the ridge to ensure current confinement to the wanted active region. To form the via on the wafer follow the steps below:

[Note: The following steps don't show the trenches. For IEM devices you still can use the same steps].

6.4.1. Deposit 1200 Å thick SiO_2:

Follow the SiO_2 deposition procedure detailed in Sec. 6.2 to deposit 1200 Å thick SiO_2 (see Figure 6.10).

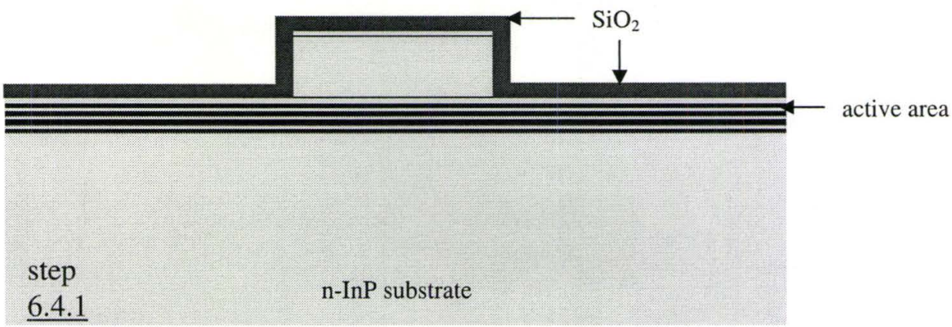

Figure 6.10: *The wafer after depositing SiO_2 for via opening. The SiO_2 film covers all sides of the ridge.*

6.4.2. Via patterning:

Follow the photolithography steps in Sec. 6.2.1.1 steps 1-13 but this time use the via pattern in the mask in step 7 (see Figure 6.11).

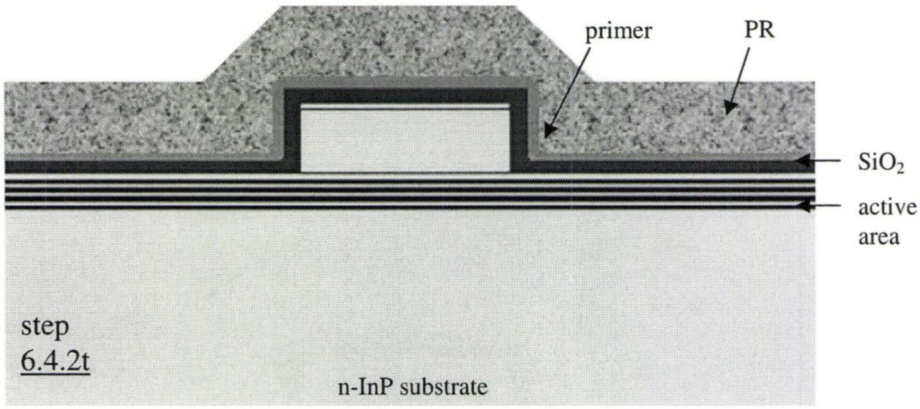

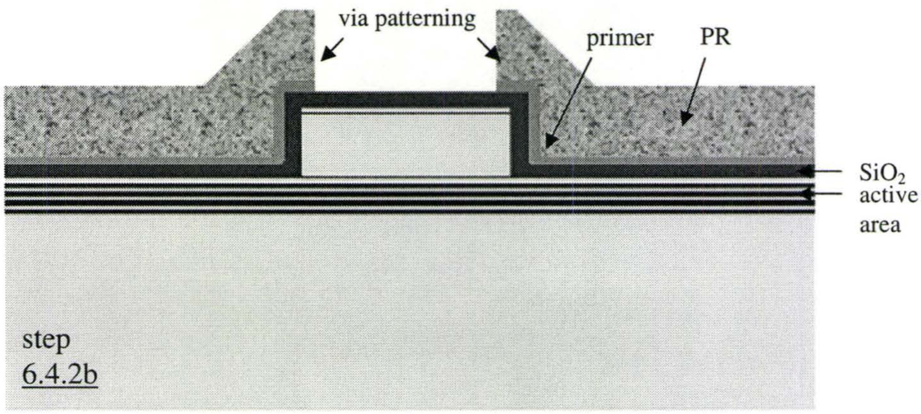

Figure 6.11: *Wafer after photolithography processes to pattern the via. The wafer after depositing primer, PR (top) and then the wafer after exposing and developing the PR (bottom).*

6.4.3. Open the Via:

1. To open the vias follow the steps detailed in Sec. 6.2.1.2. Make sure not to over-etch the SiO_2 because over-etching will undercut the SiO_2 under the PR and expose the ridge sides (see Figure 6.12 top). Examine the wafer under a

high power microscope and make sure all the SiO_2 is removed from the top of the ridge except from the side edges of the ridge top.

2. Follow the steps in Sec. 6.2.1.3 to strip the PR and then examine the wafer under a high power microscope (see Figure 6.12 bottom). For a normal process you should see the edges of SiO_2 on top of the ridges as shown in Figure 6.12. You can see that easily if you focus in between the SiO_2 surface and the contact layer surface. If you don't see lines at each side then you over-etched and you need to redo all the via steps again (Sec. 6.4).

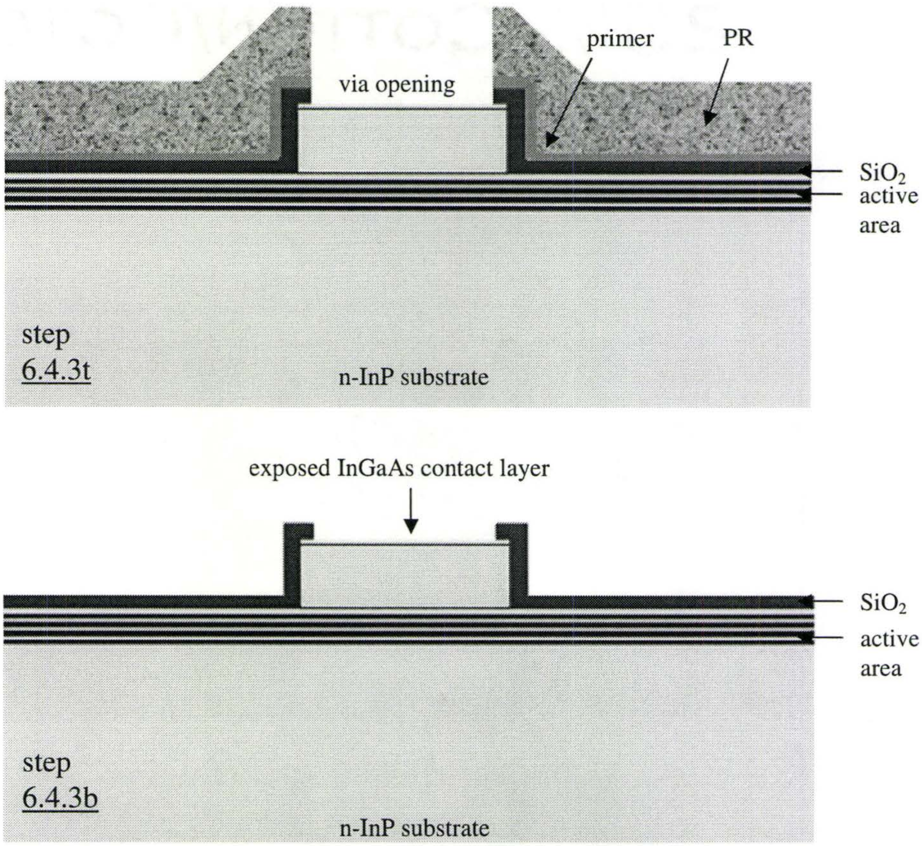

Figure 6.12: *The wafer after opening the via (top), and after stripping the PR (bottom).*

6.5. p-Metallization:

The p-metallization is done using a lift-off technique. To do the lift-off for p-metallization, the PR photolithography is prepared differently than the usual method in Sec. 6.2.1.1.

6.5.1. Lift-off Photolithography:

1. Spin Primer at speed of 4000 rpm for 30 s. Use MicroPrime from Shin-Etsu. Micro Si Company.
2. Spin positive photo-resist (PR) at a speed of 4000 rpm for 30 s on the wafer surface. Use S1808 (PR) from Rohm Haas Electronic Materials.
3. Let the wafer sit in a dish partially covered for 5 minutes.
2. Set the wafer on a microscope glass slide on top of a hot plate covered with a Pyrex dish and bake for 2 minutes at 90 °C.
3. Clean the mask with the following solutions in sequence: acetone, methanol, and DI water, and then dry with an N_2 gun.
4. Refer to the mask aligner procedure sheet. In this step we will over expose. To find out the exposure time on the mask aligner raise the wafer holder, make an exposure, and then read the power as *X*. Use the following formula to find the exposure time $t_{\exp} = \frac{40}{X}$ s. Set the exposure time on the mask aligner.

5. Load the mask to the mask aligner after choosing the right pattern (metal) and load the wafer to the wafer holder. Coarse align the wafer so that the mesa will be aligned perpendicular to the major flat of the wafer.
6. Follow the instructions in the mask procedure to fine align the wafer to the mask and then expose the wafer using the exposure time calculated earlier (see Figure 6.13).
7. Slowly remove the wafer from the mask aligner and move it to the wet bench.
8. Soak the wafer in toluene for 6 minutes. This step is designed to make the surface of the exposed PR harder than the unexposed PR, which is necessary for a lift-off process.
9. Mix 1 part developer (351 type developer for the S1808 PR) to 5 parts DI water in a beaker.
10. Over develop the wafer in the developer solution for about 60 seconds (double the normal develop time). Then use fresh developer mix for another 10 s.
11. Rinse the wafer with DI water and dry with an N_2 gun.
12. Examine the wafer under a high power microscope. Make sure the metallization pattern is not washed away in most areas in the wafer. A shadow of two lines can be seen at the edges of the PR in the metallization pattern for a normal process. These two lines are separated by 1-1.5 μm, which is an indication of undercut in the PR and is a necessary undercut for the lift-off technique.

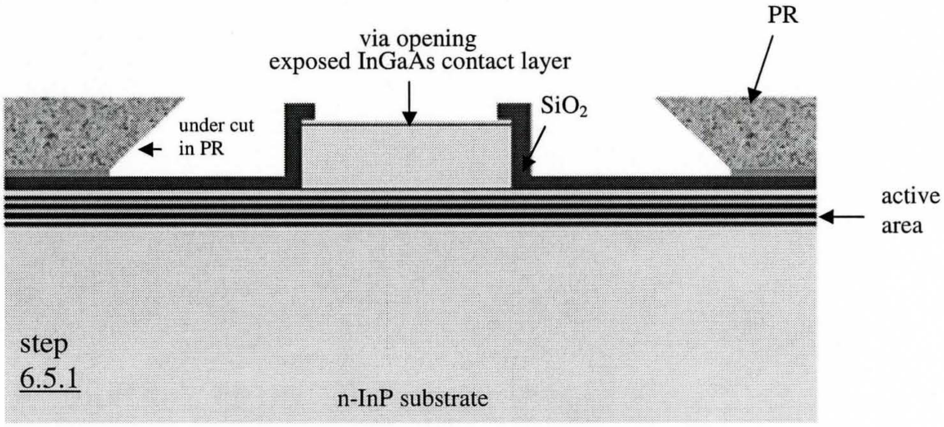

Figure 6.13: *The wafer after lift-off photolithography. Notice the undercut in the PR which is necessary for lift-off the metallization from the unwanted regions.*

6.5.2. Deposition of p-metallization:

1. Follow the system instruction sheet and safety procedures when you use the e-beam metallization system. Deposit the thin film layers of Ti/Pt/Au for p type metallization. Start with a Ti deposition 250 Å on each side of the ridge, deposit 500 Å of Pt on each side and finish with Au. Deposit 1200 Å Au on each side.
2. Use the angled wafer stage to rotate 45° for each side of the ridge by starting at 45°. At one side deposit the first metal then rotate 90° so it will be 45° on the other ridge side and deposit the same metal. Repeat this procedure for each metal (see Figure 6.14).

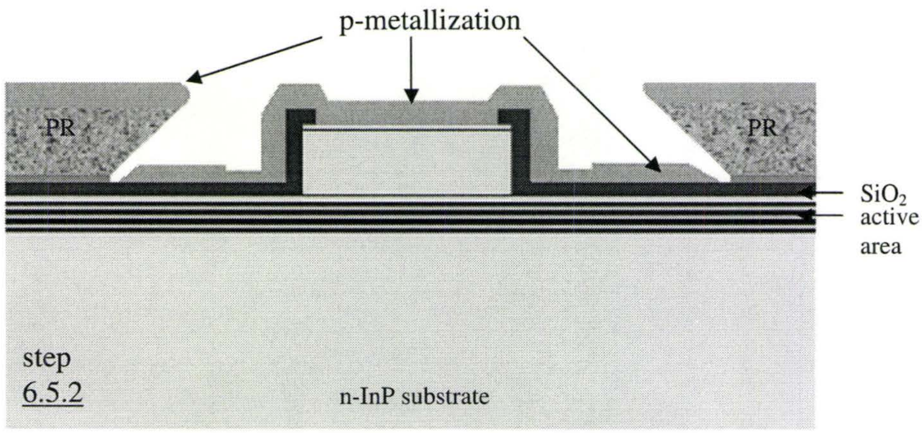

Figure 6.14: *The wafer after p-metal deposition. Notice the laser contact with metallization only on top of the ridge. The metallization on top of the PR will lift-off when the wafer is soaked in acetone.*

6.5.3. Lift-off the metallization:

Soak the wafer in acetone for 10 minutes to remove the metals from the unwanted regions. The regions without metal are the separation regions between devices. Use more soaking time if the metallization is not removed easily. Also use Q-tips with gentle rubbing to remove the metals if needed (see Figure 6.15).

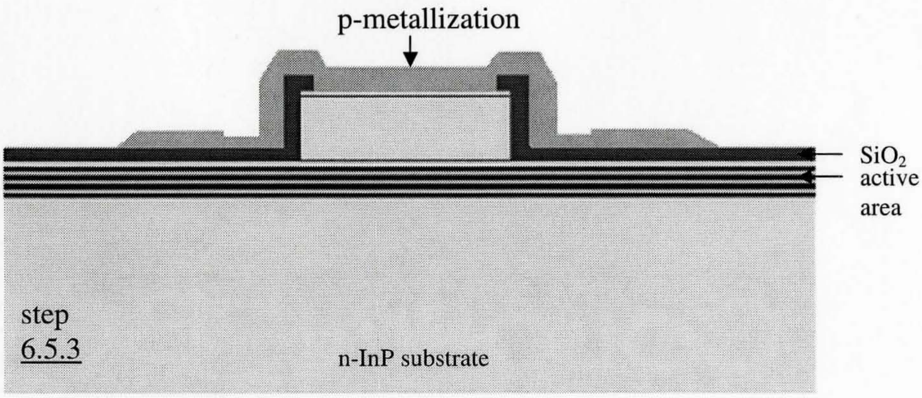

Figure 6.15: *The wafer after the metal lift-off process. The regions without metal are the separation regions between devices.*

6.6. Wafer thinning:

1. Refer to the thinning procedure instruction sheet and safety sheets in the lapping laboratory.
2. Mount the wafer face down on the lapping metal block using wax with the wafer back (i.e., the n-substrate) exposed for lapping.
3. Measure and record the wafer thickness before starting to lap.
4. Start by thinning the wafer to a thickness of 140 μm using the 15 μm steel disc and a solution of DI water with SiC (Corundum 303 from MR Semicon Inc.) powder. Thin the wafer in intervals of 2 minutes, clean the wafer after each interval with DI water and measure the wafer thickness then adjust your thinning time to reach the desired thickness.
5. Use the 5 μm disc together with a solution of DI water and 5 μm aluminum oxide (Micro Metallurgical LTD) powder to thin the wafer to about 120 μm.

6. Finally use a 1 μm disc together with 1.0 μm Alpex Alumina polishing suspension (from MR Semicon Inc.) to thin the wafer to the final thickness of 115 μm.
7. Clean the wafer and the metal block with DI water and heat on a hot plate to liquefy the wax. Slide the wafer very slowly to a Pyrex dish filled with acetone and let it soak for 10 minutes. Be careful when handling the wafer because it is very thin and very fragile.
8. Soak the wafer in fresh acetone for 2 minutes, methanol for 2 minutes, rinse with DI water for 5 minutes, and blow dry with an N_2 gun. The wafer should be ready now for back side n-metallization.

6.7. n-Metallization:

1. Mount the wafer gently on the fixed chuck n-side up.
2. Follow the system instruction sheet and safety procedures when you use the e-beam metallization system. Deposit the thin film layers of Ni/Ge/Au for the n-type metallization: Start with a deposit of 250 Å of Ni, deposit 500 Å of Ge and finish with an Au deposition of 1200 Å (see Figure 6.14).

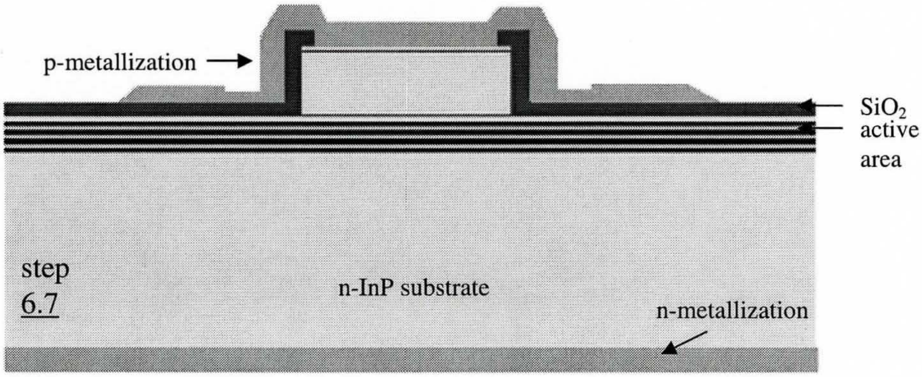

Figure 6.16: *The wafer after back side n-metallization. The p-metallization and n-metallization are the terminals to be connected to the power supply to complete the circuit.*

6.8. Wafer annealing:

1. Refer to the rapid thermal annealing (RTA) system procedure and safety sheets.
2. Set the annealing recipe for a 50 s ramp up to 400 °C, a 30 s soak at 400°C, and a 50 s ramp down to room temperature.
3. Open the UHP N_2 gas and the pure N_2 gas valves and make a test run without putting the wafer inside the system and watch the system behavior. If the system runs smoothly load the wafer and perform the annealing run; otherwise consult the RTA system engineer.

After the annealing process the wafer is ready for cleaving and testing.

Chapter 7

Conclusion and suggestions for future work

7.1. Conclusion

This thesis is a theoretical and experimental study of the output power of a certain type of quantum well (QW) laser diode. Broadly tunable InGaAsP/InP asymmetric multiple quantum well (AMQW) ridge waveguide laser diodes suffer from the problem of low output power. This problem of the AMQW laser diodes limits the use of these lasers in certain applications. The theoretical and experimental studies were carried out in this work to understand the reasons behind this output power problem and to find solutions to the problem. While focusing on the electrical and thermal properties of the device, a commercial BPM optical simulator was used to optimize the laser diode optical confinement factor and hence increase the output power. The laser diode output power almost doubled as a result of optical confinement optimization, which opens the door for electrical and thermal optimization studies.

A commercially available partial differential equation solver, FlexPDE, was used to solve the electronic and thermal equations and hence simulate the laser diode device. The FlexPDE solutions – which were validated with published data – showed poor current injection efficiency to the center of the device active area. The FlexPDE simulator solutions showed that the main reason for this poor current injection efficiency is the nature of the ridge structure. Since the ridge structure is an essential part of this type of laser diode, effort was focused into reducing the effect of the ridge structure on the current injection efficiency. The device simulations showed that the doping profile can affect significantly the current injection efficiency to the active area. Different types of doping profiles were simulated and the effect of delta doping on the device was studied. The simulation results showed that extending the doping profile closer to the active area would improve significantly the current injection efficiency by reducing the effect of the ridge structure. Also, the simulations showed that the current injection efficiency did not improve when delta doping was introduced to the doping profile. On the other hand, the device simulations showed that the novel method of forced electrical confinement dramatically improved the current injection efficiency of the device. This improvement can be varied according to the amount of recombination centers that are introduced to the isolation etch area. This recombination center effect was included in the FlexPDE scripts.

Experimental data on InGaAsP/InP AMQW laser diodes showed that extending the doping profile close to the SCH/active region interfaces increased significantly the output laser power. The experimental data not only supported the simulation results carried out in this study regarding the doping issue, but also discharged the fear that some laser diode researchers expressed about extending the doping profile closer to the active area. The experimental results showed that the increase in the output power as a result of extending the doping profile was much more significant than the losses the device endures as a result of the interaction of this extended doping with the optical field.

For the first time, the AMQW laser power profiles are categorized according to the different shapes and the dip in the output power profile. A detailed explanation of the reasons behind the different categories is reported. Also, an experimentally supported explanation for the dip in the output power profile and its position was postulated.

On the issue of the forced electrical confinement, the experimental data showed that the isolation etch method (IEM) has good potential in improving the output power of the AMQW laser diode. Both the theoretical and experimental study showed that minimizing the recombination center effect could make the IEM a preferred method in broadly tunable AMQW laser diode production lines.

The over all output power went from a range of 2-5 mW to a range of 15-18 mW as a result of this study. A discussion to the two distinct output power profile shapes was included in the study, while detailed explanations for the dip in the power profile were reported and were supported by experimental measurements.

A unique method of distance measurement using one of the first optimized, broadly tunable InGaAsP/InP short-external-cavity diode lasers was reported. This method uses a non-linear, least squares fitting method to extract the displacement from the raw data. This fitting method together with the wide tuning range (100 nm) made it possible to achieve sub–micron resolution of the displacement. The uniqueness of this method is that the sub–micron resolution of the displacement is achieved even in the presence of significant noise and mode hopping. Because of this achievement this novel method can be a suitable candidate for real life applications.

7.2. Suggestions for future work

Broadly tunable AMQW ridge waveguide laser diodes are used in many fields. The physics of these devices is thus an important topic which contains many interesting phenomena and challenges. I am always fascinated by these small but powerful devices. One important lesson I learned from my Ph.D studies about these devices is that there will be always room for improvement. For instance, the simulation code can be improved by including quantum effects. However there is a trade off between the gains that designers can achieve from this step compared with the time that will take to run such improved code. The same argument can be associated with the inclusion of the optical field equation to the code. It is fascinating to have simulated LI curves compared with the experimental ones but the computational price for doing so should be weighed in the process.

On the other hand, this study showed the sensitivity of the performance of AMQW ridge waveguide laser diodes to the doping profile. In my opinion the process of refining the doping profile is worth investigating to optimize the device. Also the study showed the potential of the IEM on improving the laser optical performance. However the introduce of recombination centers as a direct result of this process can limit the benefits of this method. The issue of recombination centers is a passivation issue so there is a need to investigate different passivation techniques to reduce and finally eliminate the amount of recombination centers generated. In my experimental work I used a simple SiO2 thin film layer to isolate the exposed regions but more complex thin film layers using ZrO_2, Al_2O_3, and Ga_2O_3 based materials are worth investigation[111]. An innovative idea for passivation could be to engineer the bandgap at these exposed regions to introduce a wider bandgap that will work as a mechanism to block the carriers from reaching the exposed edges. Engineering the bandgap of the exposed regions can be as simple as returning the etched wafer to the growth chamber and at the growth temperature flow phosphoric gas to replace some of the arsenic atoms at the exposed etched regions. Conversely, engineering the band gap could be as complicated as doing a re-growth after etching[112]. In either case it is worth investigating since the outcome might have a large impact on the optical performance of these devices.

Appendix A:

Model validation with published data:

To have confidence in the model described in Chapter 2 and the implementation of the model, it must be validated. One method to validate is to compare the results of simulations using the model with published data. The validation step should be easy work if the doping profile is well defined. If the doping profile is not well defined then the validation process basically looks more into validating the trends that simulations and the publication show. Unfortunately there are few publications that give a well defined doping profile for the device under study. In this section I validate the model with publications that give sufficient details about their devices.

One of the papers that gave well defined doping profiles was Lee *et al.*[113]. The doping profile I used in the simulation in comparison to their doping profile is shown in Figure A.1. Since their doping profile is complicated there were a few features I could not match in my simulations but I could approximate their profile.

In their paper Lee *et al.* tried to investigate numerically the variation of band diagrams and the relevant physical quantities such as quasi-Fermi levels. Quantum size effects are ignored and they used the basic semiconductor device equations for heterostructures.

Figure A.2 shows energy band diagrams of the simulation compared with the published plots at 0 and 1.2 V. The figure shows plots that lay on top of each other for both the published data in the paper and simulation. Figure A.3 shows plots of the electric field across the junction for both the simulation and published data at different

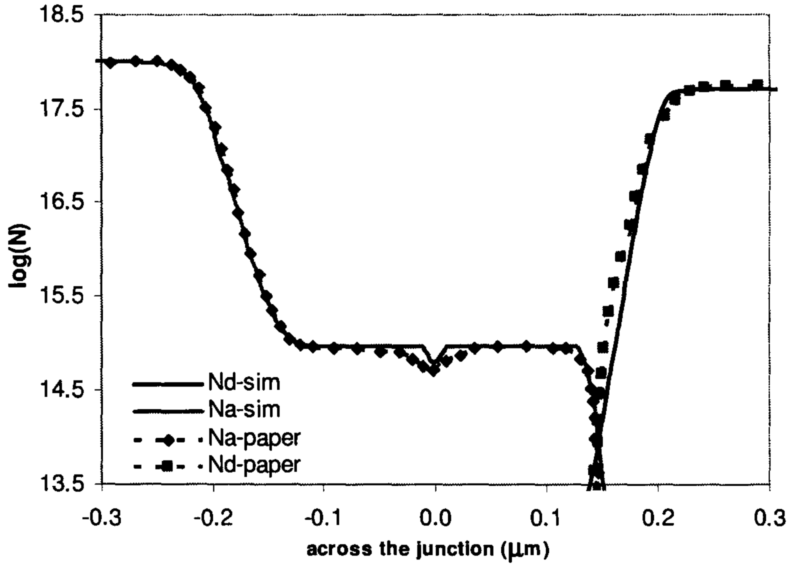

Figure A.1: *Doping profile used in reference [113] compared with the doping profile used in the simulation.*

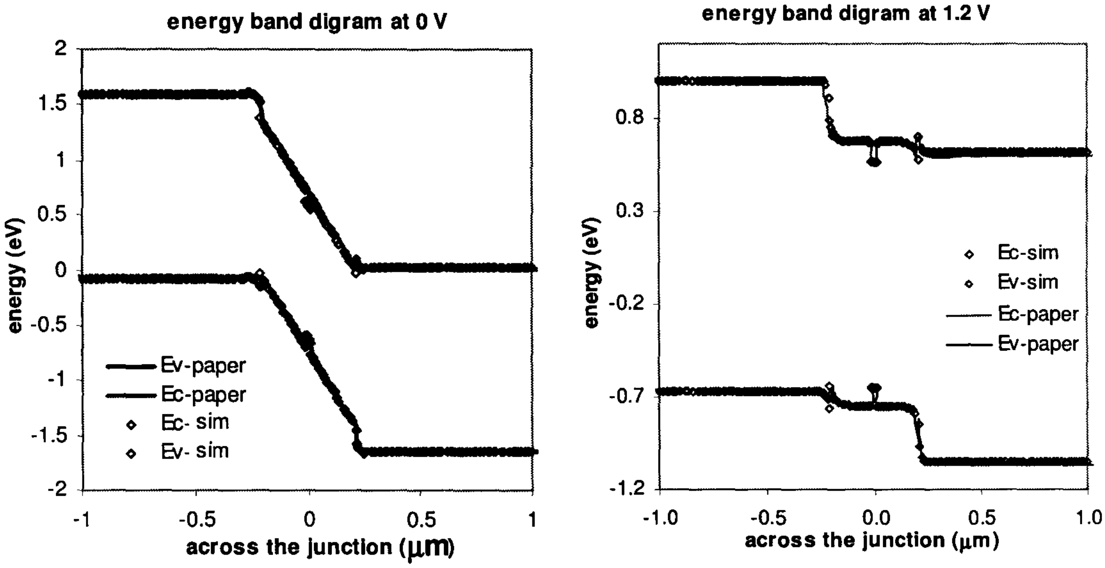

Figure A.2: *Energy band diagrams of the simulation compared with the paper plots at 0 and 1.2 V. Both the simulation and the published data lay on top of each other.*

applied voltages. The dotted curves are for the simulation data while the solid lines are for the published data. It is well known that any changes in the doping profile will be reflected on the junction electric field. You can see the spikes in the electric field left and right of the device center and also the device center which is a result of the change in the doping profile see Figure A.1. These spikes can be seen in the published data and in my simulation as well. At the beginning I did not see the spikes in the center in my simulation because I did not add a dip in my doping profile at the center to save on converging time. Then later when I added this dip, which is shown in Figure A.1, my simulations did not match the dip in the reference but were the closest I could get to the published data without increasing the converging time significantly. The amplitude of these spikes increase with the increase of the doping profile variation. It is easy to see the spikes at the center are much smaller than the spikes on each side because the variation of the doping profile at the center is smaller than that at the sides. This also explains why the spikes at the device center for the simulation data are less than those in the published data.

Figure A.4 shows the electrostatic potentials of the devices for both simulations and the paper at different applied voltages (top curves). Again the dotted curves are for the simulation data and the solid lines are for the published data. The bottom curves in Figure A.4 shows the magnified simulated electrostatic potential data near the center of the junction for applied voltages over 1.3 V. The same trend can be seen as in the published data. However, the magnitudes of the peaks are slightly higher in the paper because of the doping profile mismatch discussed earlier. The author gives the built-in potential as 1.607 V[113], which is the same as I obtained. Finally Figure A.5 shows the IV curves for the simulation and published data.

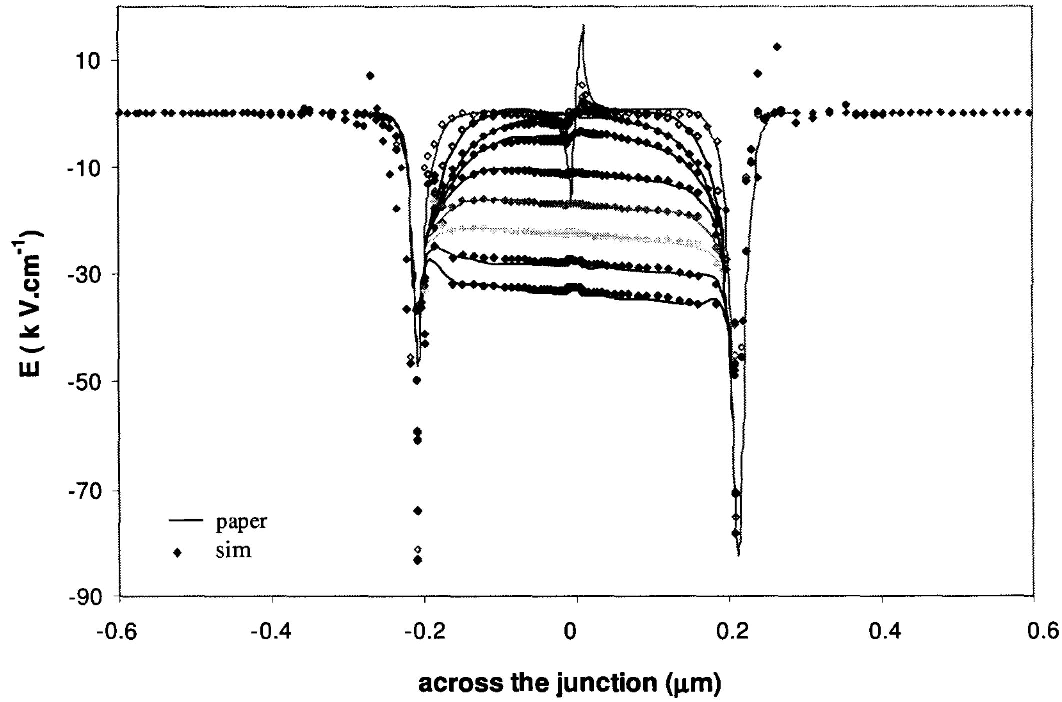

Figure A.3: *Electric field plots across the junction for both simulation and paper data at different applied voltages where the solid lines are for the published data and the dotted curves are for the simulation data.*

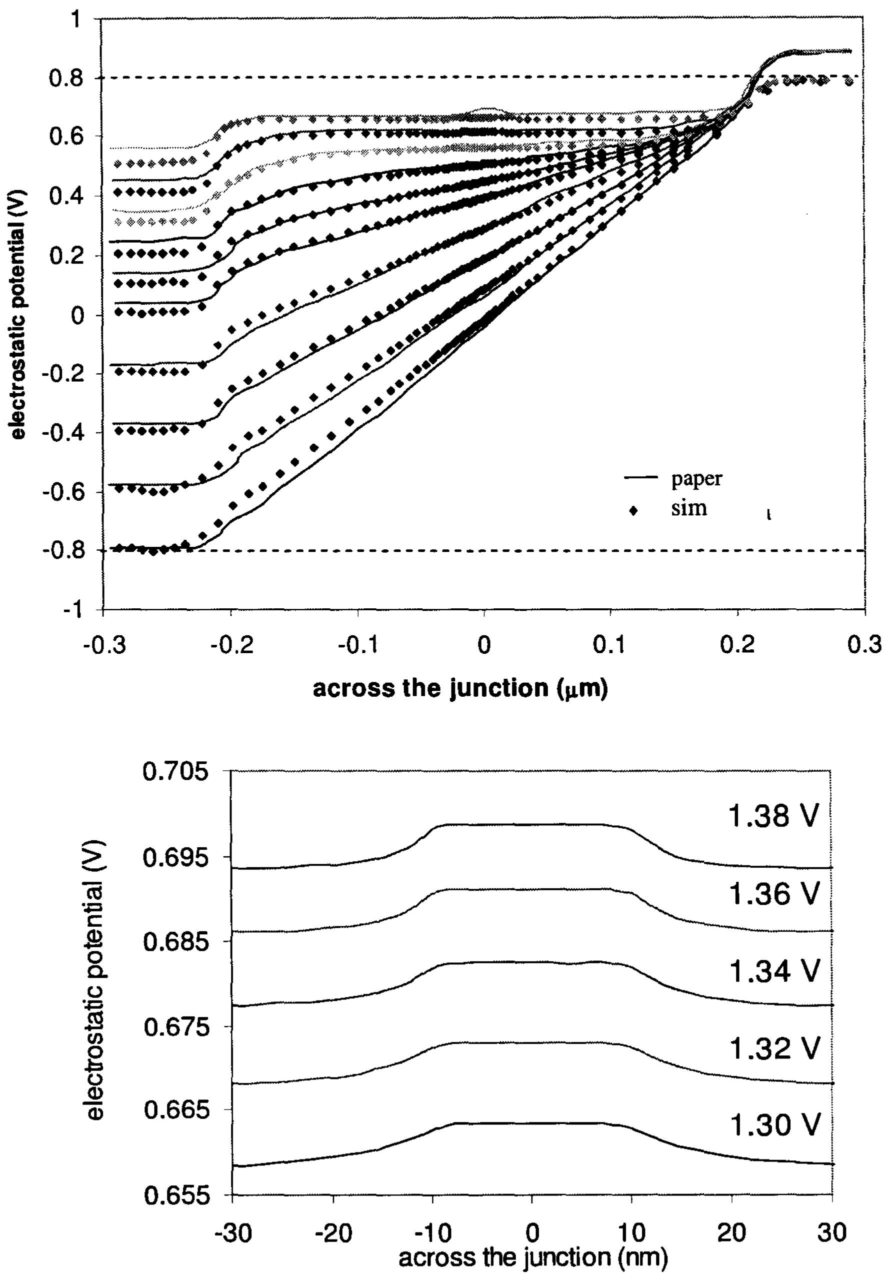

Figure A.4: *Electrostatic potential of the device for both simulation and published results at different applied voltages (top curves). The bottom curves are for simulated data near the center of the junction for applied voltages over 1.3 V where we can see the same trend as in the paper.*

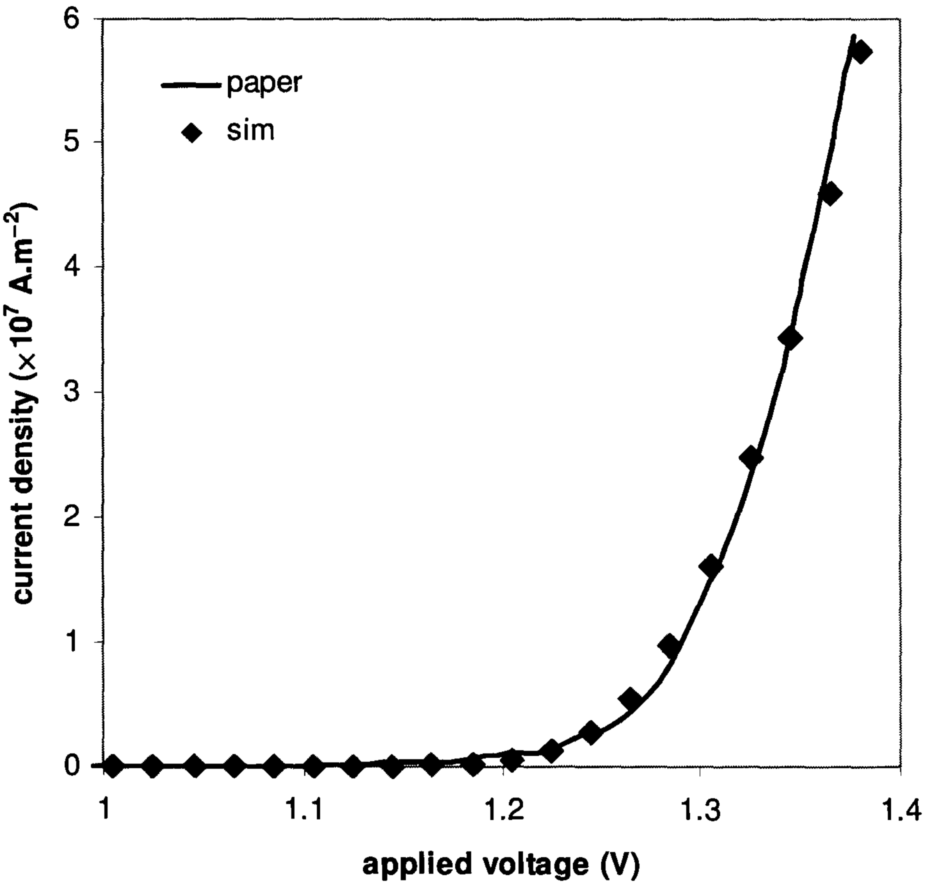

Figure A.5: *J-V curve from published results and from simulation at different applied voltages.*

Appendix B:

Information on the layers for the three laser structures that are reported in this thesis are given in this Appendix.

Laser Structure of Wafer 4261

Number of layers: 21
Number of QW's: 5
Structure thickness: 29330.0 Å

Layer	Layer name	Composition						Strain			Thickness (Å)	Doping level (cm^{-3})	Dopant	
		Material	x	y	Gap (nm)	PL (nm)	MQW PL (nm)	%	% Critical	Sum (%Å)			Species	type
21	Cladding	p-InGaAs	0.47	1	1694	1664.2			-0.1	-106.2	2000	1×10^{19}	Zn	p
20	Cladding	p-InP			918.4	909.6			0.0	-105.8	1300	1×10^{18}	Zn	p
19	Cladding	p-InP			918.4	909.6			0.0	-105.8	2000	4×10^{17}	Zn	p
18	Cladding	p-InGaAsP	0.28	0.61	1338	1319.5			-0.1	-105.8	30	4×10^{17}	Zn	p
17	Cladding	p-InP			918.4	909.6			0.0	-105.3	1000	4×10^{17}	Zn	p
16	SCH	InGaAsP	0.08	0.18	970.7	960.8			0.1	-105.3	700	undoped		
15	SCH	InGaAsP	0.23	0.49	1061	1049.4			-0.3	-106.0	700	undoped		
14	Barrier	InGaAsP	0.23	0.31	1095	1082.0		0.60	37.6	-104.4	150	undoped		
13	Well	InGaAsP	0.23	0.8	1720	1689.0	1599.1	-1.01	-47.3	-195.1	100	undoped		
12	Barrier	InGaAsP	0.23	0.31	1095	1082.0		0.60	12.5	-94.0	50	undoped		
11	Well	InGaAsP	0.23	0.71	1551	1525.8	1458.5	-0.72	-31.1	-124.2	100	undoped		
10	Barrier	InGaAsP	0.23	0.31	1095	1082.0		0.60	12.5	-52.0	50	undoped		
9	Well	InGaAsP	0.23	0.69	1517	1493.2	1430.4	-0.66	-27.8	-82.3	100	undoped		
8	Barrier	InGaAsP	0.23	0.31	1095	1082.0		0.60	12.5	-16.6	50	undoped		
7	Well	InGaAsP	0.23	0.69	1517	1493.2	1430.4	-0.66	-27.8	-46.8	100	undoped		
6	Barrier	InGaAsP	0.23	0.31	1095	1082.0		0.60	12.5	18.9	50	undoped		
5	Well	InGaAsP	0.23	0.8	1720	1689.0	1599.1	-1.01	-47.3	-11.4	100	undoped		
4	Barrier	InGaAsP	0.23	0.31	1095	1082.0		0.60	37.6	89.8	150	undoped		
3	SCH	InGaAsP	0.23	0.49	1061	1049.4			-0.3	-0.9	700	undoped		
2	SCH	InGaAsP	0.08	0.18	970.7	960.8			0.1	0.6	700	undoped		
1	Cladding	n-InP			918.4	909.6			0.0	0.0	7500	1×10^{18}	Si	n
0	Substrate	n-InP									7500	1×10^{18}	Si	n

Laser Structure of Wafer 4381

Number of layers: 21
Number of QW's: 5
Structure thickness: 33066.0 Å

Layer	Layer name	Composition						Strain			Thickness (Å)	Doping level (cm^{-3})	Dopant	
		Material	x	y	Gap (nm)	PL (nm)	MQW PL (nm)	%	% Critical	Sum (%Å)			Species	type
21	Cladding	p-InGaAs	0.47	1	1694	1664.2			-0.1	-18.1	2000	1×10^{19}	Zn	p
20	Cladding	p-InP			918.4	909.6			0	-17.6	15000	1×10^{18}	Zn	p
19	Cladding	p-InP			918.4	909.6			0	-17.6	2000	4×10^{17}	Zn	p
18	Cladding	p-InGaAsP	0.28	0.61	1338	1319.5		-0	-0.1	-17.6	30	4×10^{17}	Zn	p
17	Cladding	p-InP			918.4	909.6			0	-17.2	1000	4×10^{17}	Zn	p
16	SCH	InGaAsP	0.04	0.09	970.7	960.8			0.2	-17.2	1500	undoped		
15	SCH	InGaAsP	0.11	0.24	1061	1049.4			0.2	-18.4	700	undoped		
14	Barrier	InGaAsP	0.23	0.31	1095	1082.0		0.6	54.7	-19.2	218	undoped		
13	Well	InGaAsP	0.23	0.8	1720	1689.0	1599.1	-1	-47.3	-151	100	undoped		
12	Barrier	InGaAsP	0.23	0.31	1095	1082.0		0.6	12.5	-49.9	50	undoped		
11	Well	InGaAsP	0.23	0.71	1551	1525.8	1458.5	-0.7	-31.1	-80.1	100	undoped		
10	Barrier	InGaAsP	0.23	0.31	1095	1082.0		0.6	12.5	-7.95	50	undoped		
9	Well	InGaAsP	0.23	0.69	1517	1493.2	1430.4	-0.7	-27.8	-38.2	100	undoped		
8	Barrier	InGaAsP	0.23	0.31	1095	1082.0		0.6	12.5	27.5	50	undoped		
7	Well	InGaAsP	0.23	0.69	1517	1493.2	1430.4	-0.7	-27.8	-2.74	100	undoped		
6	Barrier	InGaAsP	0.23	0.31	1095	1082.0		0.6	12.5	62.95	50	undoped		
5	Well	InGaAsP	0.23	0.8	1720	1689.0	1599.1	-1	-47.3	32.72	100	undoped		
4	Barrier	InGaAsP	0.23	0.31	1095	1082.0		0.6	54.7	133.9	218	undoped		
3	SCH	InGaAsP	0.11	0.24	1061	1049.4			0.2	2.05	700	undoped		
2	SCH	InGaAsP	0.04	0.09	970.7	960.8			0.2	1.22	1500	undoped		
1	Cladding	n-InP			918.4	909.6			0	0	7500	1×10^{18}	Si	n
0	Substrate	n-InP									7500	1×10^{18}	Si	n

Laser Structure of Wafer 4693

Number of layers: 23
Number of QW's: 5
Structure thickness: 35566.0 Å

Layer	Layer name	Composition						Strain			Thickness (Å)	Doping level (cm^{-3})	Dopant	
		Material	x	y	Gap (nm)	PL (nm)	QW PL (nm)	%	% Critical	Sum (%Å)			Species	type
23	Cladding	p-InGaAs	0.47	1	1694	1664.2			-0.1	-18.1	2000	1×10^{19}	Zn	p
22	Cladding	p-InP			918.4	909.6			0	-17.6	15000	1×10^{18}	Zn	p
21	Cladding	p-InP			918.4	909.6			0	-17.6	2000	1×10^{18}	Zn	p
20	Cladding	p-InGaAsP	0.28	0.61	1338	1319.5			-0.1	-17.6	30	1×10^{18}	Zn	p
19	Cladding	p-InP			918.4	909.6			0	-17.2	1000	1×10^{18}	Zn	p
18	SCH	InGaAsP	0.04	0.09	970.7	960.8			0.2	-17.2	1500	1×10^{18}	Zn	p
17	SCH	InGaAsP	0.11	0.24	1061	1049.4			0.2	-18.4	550	5×10^{17}	Zn	p
16	SCH	InGaAsP	0.11	0.24	1061	1049.4			0.2	-18.4	150	undoped		
15	Barrier	InGaAsP	0.23	0.31	1095	1082.0		0.6	54.7	-19.2	218	undoped		
14	Well	InGaAsP	0.23	0.8	1720	1689.0	1599.1	-1	-47.3	-151	100	undoped		
13	Barrier	InGaAsP	0.23	0.31	1095	1082.0		0.6	12.5	-49.9	50	undoped		
12	Well	InGaAsP	0.23	0.71	1551	1525.8	1458.5	-0.7	-31.1	-80.1	100	undoped		
11	Barrier	InGaAsP	0.23	0.31	1095	1082.0		0.6	12.5	-7.95	50	undoped		
10	Well	InGaAsP	0.23	0.69	1517	1493.2	1430.4	-0.7	-27.8	-38.2	100	undoped		
9	Barrier	InGaAsP	0.23	0.31	1095	1082.0		0.6	12.5	27.5	50	undoped		
8	Well	InGaAsP	0.23	0.69	1517	1493.2	1430.4	-0.7	-27.8	-2.74	100	undoped		
7	Barrier	InGaAsP	0.23	0.31	1095	1082.0		0.6	12.5	62.95	50	undoped		
6	Well	InGaAsP	0.23	0.8	1720	1689.0	1599.1	-1	-47.3	32.72	100	undoped		
5	Barrier	InGaAsP	0.23	0.31	1095	1082.0		0.6	54.7	133.9	218	undoped		
4	SCH	InGaAsP	0.11	0.24	1061	1049.4			0.2	2.05	150	undoped		
3	SCH	InGaAsP	0.11	0.24	1061	1049.4			0.2	2.05	550	5×10^{17}	Si	n
2	SCH	InGaAsP	0.04	0.09	970.7	960.8			0.2	1.22	1500	1×10^{18}	Si	n
1	Cladding	n-InP			918.4	909.6			0	0	7500	1×10^{18}	Si	n
0	Substrate	n-InP									7500	1×10^{18}	Si	n

Bibliography

1- J. P. Van der Ziel, R. C. Miller, W. Wiegmann, and Jr. W. A. Nordland, "Laser oscillations from quantum states in very thin GaAs–$Al_{0.2}Ga_{0.8}As$ Multilayer structures", Appl. Phys. Lett., vol. 26, pp. 463–465, 1975.

2- R. Dingle, and C. H. Henry, "Quantum effects in hetrostructure lasers", U.S. Patent 3982207, Sep. 1976.

3- N. Holonyak Jr., R. M. Kolbas, W. D. Laidig, B. A. Vojak, R. D. Dupuis, and P. D. Dapkus, " Low-threshold continuous laser operation (300-337 K) of multilayer MOCVD AlxGa1-xAs–GaAs quantum well structures", Appl. Phys. Lett., vol. 33, pp. 737–739, 1978.

4- S. Ikeda, A. Shimizu, and T. Hara, "Asymmetric dual quantum well laser-wavelength switching controlled by current injection" Appl. Phys. Lett., vol. 55, No. 12, pp. 1155-1157, 1989.

5- H. Kawaguchi and T. Kawakami, "Transverse-mode control in an injected laser by a strip-loaded waveguide", IEEE J. Quantum Electron, QE-13, No. 8, pp. 556-560, Aug. 1977.

6- M. J. Robertson, S. Ritchie, and P. Dayan, "Semiconductor waveguides: analysis of optical propagation in single rib structures and directional couplers", IEE Proceedings, vol. 132, Pt. J, No. 6, pp. 336-342, Dec. 1985.

7- K.S. Chiang, "Analysis of rectangular dielectric waveguides", Electron. Lett., vol. 28, No. 4, pp. 388-390, 1992

8- S. C. Woodworth, D. T. Cassidy, and M. J. Hamp, "Sensitive absorption spectroscopy by use of asymmetric multiple-quantum-well diode laser in an external cavity", Applied Optics, vol. 40, No. 36, pp. 6719-6724, 2001.

9- H. M. Enshasy, and D. T. Cassidy, "Sub-micrometer resolution distance measurement with broadly tunable short-external-cavity InGaAsP/InP diode laser", IET Optoelectronics J., vol. 1, No. 4, pp. 157-162, 2007.

10- J. Wang, and D. T. Cassidy, "Broadly tunable, short external cavity diode laser for optical coherence tomography", I.E.T. Optoelectronics J., vol. 2, No. 1, pp. 46-54, 2008.

11- S. C. Woodworth, D. T. Cassidy, and M. Hamp, "Experimental analysis of a broadly tunable InGaAsP laser with compositionally varied quantum wells", IEEE J. Quantum Electron., vol. 39, No. 3, pp.426-430, 2003.

12- X. Zhu, D. T. Cassidy, M.J. Hamp, D. A. Thompson, B. J. Robinson, Q. Zhao, and M. Davies, "1.4-μm InGaAsP-InP strained multiple –quantum-well laser for broad-wavelength tunability", IEEE Photonics Tech. Lett., vol. 9, No. 9, pp. 1202-1204, Sept. 1997.

13- C. C. Huang, C. H. Cheng, Y. S. Su, and C. F. Lin, "174-nm mode spacing in dual-wavelength semiconductor laser using non-identical InGaAsP quantum wells", IEEE Photonics Tech. Lett., vol. 16, No. 2, pp. 371-373, Feb. 2004.

14- G. B. Morrison, S. C. Woodworth, H. Wang, and D. T. Cassidy, "Galerkin method for calculating valence-band wave-functions in quantum-well structures using exact envelop theory", IEEE J. Quantum Electron., vol. 40, No. 3, pp.222-230, 2004.

15- S. L. Chuang, Physics of optoelectronic devices, New York: John Wiley & Sons, Inc., Chapter 4, pp.125-199, 1995.

16- J. Bardeen, "An improved calculation of the energies of metallic Li and Na", J. Chem. Phys., vol. 6, pp. 367-371, 1938.

17- J. Luttinger, and W. Kohn, "Motion of electrons and holes in perturbed periodic fields", Phys. Rev., vol. 97, pp. 869-883, 1955.

18- H. Wang, D. Bruce, D. T. Cassidy, "Gain characteristics of Asymmetric multiple quantum well lasers", IEEE. J. Quantum Electron., vol. 42, No. 5, pp. 464-470, 2006.

19- C. F. Lin, M. J. Chen, and B. L. Lee, "Wide-range tunable dual-wavelength semiconductor laser using asymmetric dual quantum wells", IEEE Photonics Tech. Lett., vol. 10, No. 9, pp. 1208-1210, Sep. 1998.

20- H.S. Gingrich, D. R. Chumney, S. Z. Sun, S. D. Hersee, L. F. Lester, and S. R. J. Brueck, "Broadly tunable external cavity laser diode with staggered thickness multiple quantum wells", IEEE Photonics Tech. Lett., vol. 9, No. 2, pp. 155-157, Feb. 1997.

21- H. Wang, D. T. Cassidy, "Gain measurement of Fabry-Pérot semiconductor lasers using a nonlinear least-squares fitting method", IEEE J. Quantum Electron., vol.41, No. 4, pp. 532-540, April 2005.

22- FlexPDE Solution Inc., http://www.flexpde.com/index.html

23- Johnson Lee and M. O. Vassell, "Variations of energy-band-diagrams with forward bias voltages for step-like separate-confinement-heterostructure for single-quantum-well lasers", IEEE Photon. Technol. Lett., vol.4, No. 11, pp 1222-1224, Nov. 1992.

24- S. L. Chuang, Physics of optoelectronic devices, New York: John Wiley & Sons, Inc. Chapter 2, pp.20-79, 1995.

25 - A. H. Marshak and C. M. Van Vliet, "Electrical current and carrier density in degenerate material with non-uniform band structure", Proc. IEEE, vol. 72, pp. 148-1644, 1984.

26 - C. M. Wolfe, N. Holonyak Jr. and G. E. Stillman, Physical properties of semiconductors, Prentice Hall, Englewood Cliffs, New Jersey, 1989.

27- B. Grossman and M. Hargrove, "Numerical solution of semiconductor transport equations with current boundary conditions", IEEE Trans. Elect. Devices, vol. ED-30, pp. 1092- 1096, 1983.

28- O. W. Purbo, D. T. Cassidy, and S. H. Chisholm, "Numerical model for degenerate and heterostructure semiconductor devices", J. Appl. Phys., V. 66, pp.5078, 1989.

29- O. W. Purbo, "Numerical models for degenerate and heterostrcture semiconductor diodes", Master Thesis, McMaster University, Apr. 1990.

30- R. J. Van Overstraeten and R. P. Mertens, "Heavy doping effects in silicon", Solid State Electron, vol. 30, pp. 1077-1087, 1987.

31- J. A. del Alamo and R. M. Swanson, "Modeling of minority-cattier transport in heavily doped silicon emitters", Solid State Electron, vol. 30, pp. 1127-1136, 1987

32- C. R. Selvakumar and D. J. Roulston, "A new simple analytical emitter model for bipolar transistor", Solid State Electron, vol. 30, pp. 723-728, 1987

33- A. H. Marshak, "On the nonequilibrium carrier density equations for highly doped devices and heterostructures", Solid State Electron, vol. 31, pp. 1551-1553, 1988

34 - B. G. Streetman, Solid state electronic devices, Prentice Hall, Englewood Cliffs, New Jersey, 4th Edition, 1995.

35- S. M. Sze, Physics of semiconductor devices, John Wiley and Sons, third edition, Hoboken, New Jersey, 2007.

36- S. Selberherr, Analysis and simulation of semiconductor devices, Springer, New York, 1984.

37- W. B. Joyce and R. W. Dixon, "Analytic approximations for the Fermi energy of ideal Fermi gas", Appl. Phys. Lett., vol. 31, pp. 354-356, 1977.

38- J. S. Blakemore, "Approximation of the Fermi Dirac integrals, especially the function $F_{1/2}$(x) used to describe electron density in a semiconductor", Solid State Electron, vol. 25, pp. 1067-1076, 1982.

39- X. A. Humett, F. S. Mastres, and J. Millan, "An analytical approximation for Fermi-Dirac integral $F_{3/2}(x)$", Solid State Electron, vol. 24, pp. 981-982, 1981.

40- D. Bendnarczyk and J. Bednarczyk, "The approximation of the Fermi-Dirac integral $F_{1/2}$(x)", Phys. Lett., vol. 64A, pp. 409-410, 1978.

41- R. Olshansky, C. J. Manning and W. Powazinik, "Measurement of radiative and nonradiative recombination rates in InGaAsP and AlGaAs light sources", IEEE J. Quantum Electron. QE-20, No.8, pp. 838–854, Aug. 1984.

42- D. Wilt, A. Yariv, "A self-consistent static model of the double-heterostructure laser", IEEE J. Quantum Electron., QE-17, No. 9, pp.1941-1949, Sep. 1981.

43- Y. Liu, K. D. Choquette, and K. Hess, "The electrical turn-on characteristics of vertical-cavity-surface-emitting lasers", Appl. Phys. Lett., V. 83, No. 20, pp. 4104-4106, Nov. 2003.

44- S. Laux, and Karl Hess, "Revisiting the analytic theory of p-n junction impedance: Improvements guided by computer simulation leading to a new equivalent circuit", IEEE Trans. Electron. Dev., vol.46, No. 2, pp. 396-412, Feb. 1990.

45- D. Wilt, A. Yariv, "A self-consistent static model of the double-heterostructure laser", IEEE J. Quantum Electron., QE-17, No. 9, pp.1941-1949, Sep. 1981.

46- O. V. Roos, "Recombination-generation current in degenerate semiconductors", Solid State Electron, vol. 21, pp.633-636, 1978.

47- D. J. Deforge, "Numerical modeling of asymmetric multiple quantum well lasers", Thesis, McMaster University, 2002.

48- K. H. Hellwege, E. Landolt-Börnstein, "Numerical data and functional relationships in science and technology", New Series, Groups III-V, vol. 22a, Springer, Berlin, 1983.

49- K. Utaka, Y. Suematusu, K. Kobayashi, and H. Kawanishi "GaInAsP/InP Integrated Twin-Guide Lasers with First-Order Distributed Bragg Reflectors at 1.3 μm Wavelength", Jpn. J. Appl. Phys. vol. 19, pp. L137-L140, 1980.

50- R. E. Nahory, M. A. Pollack, W. D. Johnston Jr., and R. L. Barns, "Band gap versus composition and demonstration of Vegard's law for $In_{1-x}Ga_xAs_yP_{1-y}$ lattice matched to InP", Appl. Phys. Lett. vol. 33, No. 7, pp. 659-662, 1978.

51- A. F. Mills, Heat and mass transfer, Boston, MA: Iwin, 1995.

52- M. Szymanski, "Two-dimensional model of heat flow in broad-area laser diode: Discussion of upper boundary condition", Elsevier, Microelectronics Journal, vol.38, pp. 771-776, 2007.

53- W. Nakwaski, "Static thermal properties of broad-contactdouble-heterostructure laser diodes", Optical Quantum Electronics, vol. 15, pp. 513-527, 1983.

54- S. Adachi, "Lattice thermal resistivity of III-V compound alloys", J. Appl. Phys., vol. 54, No. 4, pp. 1844-1848, April 1983.

55- W. Nakwaski, "Thermal conductivity of binary, ternary and quaternary III-V compounds", J. Appl. Phys., vol.64, pp. 159-166, 1988.

56- M. Gudent, and J. Piprek, "Material parameters of quaternary III-V semiconductors for multilayer mirrors at 1.55 μm wavelength", Modelling Simul. Mater. Sci. Eng., vol. 4, pp. 349-357, UK, 1996.

57- W. Both, and J. Piprek, "Thermal resistance of ridge-waveguide laser diodes based on GaAs, GaSb or InP", J. Thermal Analysis, vol. 37, pp.61-71, 1991.

58- T. Kobayashi and Y. Furukawa, "Temperature distribution in the GaAs-AlGaAs Double-Hetrerostructure laser below and above threshold current", Jpn, J. Appl. Phys., vol. 14, No. 12, pp. 1981-1986, Dec. 1975.

59- S. Marchetti and T. Rozzi, "Electric field singularities at sharp edges of planar conductors", IEEE Trans. Antennas Propagat., vol.39, no. 9, pp. 1312-1320, Sept. 1991.

60- R. De Semedt, and J. G. Van Bladel, "Field singularities near aperture corners", IEE Inst. Elec. Eng. Proc., vol. 134, pt. A, no. 8, pp. 694-698, Sept. 1987.

61- B. Laikhtman, A. Gourevitch, D. Donetsky, D. Westerfeld, and G. Belenky, "Current spread and overheating of high power laser bars", J. Appl. Phys., vol. 95, no. 8, pp. 3880-3889, April 2004.

62- G. P. Agrawal and N. K. Dutta, Long-wavelength semiconductor lasers, Chapter 2, New York, 1986.

63- P. J. A. Thijs, L. F. Tiemeijer, J. J. M. Binsma, and T. van Dongen, "Progress in long-wavelength InGaAs(P) quantum-well semiconductor lasers and amplifiers", IEEE J. Quantum Electron., vol. 30, pp. 477-499, Feb. 1994.

64- S. J. Sweeney, A. F. Phillips, A. R. Adams, E. P. O'Reilly, and P. J. A. Thijs, "The effect of temperature dependent processes on the performance of 1.5-μm compressively strained InGaAs(P) MQW semiconductor diode lasers", IEEE Photonic Technol. Lett., vol 10, no. 8, pp. 1076-1078, Aug. 1998.

65- E. P. O'Reilly and M. Silver, "Temperature sensitivity and high temperature operation of long wavelength semiconductor lasers", Appl. Phys. Lett., vol. 63, no. 24, pp. 3318-3320, 1993.

66- J. Braithwaite, M. Silver, V. A. Wilkinson, E. P. O'Reilly, and A. R. Adams, "Role of radiative and nonradiative processes on the temperature sensitivity of strained and unstrained 1.5μm InGaAs(P) quantum well lasers," Appl. Phys. Lett., vol. 67, pp. 3546–3548, 1995.

67- A. R. Adams, M. Asada, Y. Suematsu, and S. Arai, "The temperature dependence, efficiency, and threshold current of In1-xGaxAsyP1-y lasers related to intervalence band absorption", Jpn. J. Appl. Phys., vol. 19, no. 10, pp. 621-624, 1980.

68- J. Piprek, D. Babic, and J. E. Bowers, "Simulation and analysis of double-fused 1.55μm vertical-cavity lasers", J. Appl. Phys., vol. 81, pp. 3382–3390, 1997.

69- L. Shterengas, "Effect of heterobarrier leakage on the performance of high-power 1.5 μm InGaAsP multiple-quantum well lasers", J. Appl. Phys., vol. 88, no. 5, pp. 2211-2214, Sept. 2000.

70- A. A. Bemussi, H. Temkin, R. A. Logan, and D. C. Coblentz, "The effect of barrier recombination on the high temperature performance of quaternary multi-quantum-well lasers", Appl. Phys. Lett., vol. 66, no. 1, pp. 67-69, 1995.

71- B. B. Elenkring, S. Smetona, and J. G. Simmons, "Maximum operating power of 1.3 μm strained layer multiple quantum well InGaAsP lasers", J. Appl. Phys., vol. 85, no. 4, pp. 2367-2379, Feb. 1999.

72- J.F. Hazell, J. G. Simmons, J. D. Evans, and C. Blaauw, "The effect of varying barrier height on operational characteristics of 1.3 μm strained-layer MQW lasers", IEEE J. Quantum Electron., vol. 34, pp. 2358-2363, 1998.

73- M. J. Hamp, D. T. Cassidy, R.B. Robinson, Q.C. Zhao, and D. A. Thompson, "Effect of barrier thickness on carrier distribution in asymmetric multiple quantum well InGaAsP lasers", IEEE Photon. Technol. Lett., vol. 12, pp. 134-136, 2000.

74- S. Ikeda, and A. Shimizu, "Theoretical analysis of dynamic response of asymmetric dual quantum well lasers", Appl. Phys. Lett., vol. 61, pp. 1016-1018, 1992.

75- A. D. Vandermeer, and D. T. Cassidy, "A rate equation model of asymmetric multiple quantum well lasers", IEEE J. Quantum Electron., vol. 41, pp. 917-924, 2005.

76- G. L. Belenky, D. V. Donetsky, C. L. Reynolds, R. F. Kazarinov, G. E. Shtengel, S. Luryi, and J. Lopata, "Temperature performance of 1.3-μm InGaAsP-InP lasers with different profile of p-doping", IEEE Photon. Technol. Lett., vol. 9, no. 12, pp. 1558-1560, Dec. 1997.

77- S. Seki, H. Oohasi, H. Sugiura, T. Hurono, and K. Yokoyama, "Dominant mechanism for limiting the maximum operating temperature of InP-based multiple-quantum-well lasers", J. Appl. Phys., vol. 79, no. 5, pp. 2192-2197, March 1996.

78- J. Piprek, P. Abraham, and J. E. Bowers, "Self-consistent analysis of high-temperature effects on strained-layer multi-quantum well InGaAsP/InP lasers", IEEE J. Quantum Electron., vol. 36, no. 3, pp. 366-374, March 2000.

79- N. Tessler, S. Marcinkevicius, U. Olin, C. K. Silfvenius B. F. Stalnacke, and G. Landgren, "Vertical carrier transport in InGaAsP multiple-quantum-well laser structures: effect of p-doping", IEEE J. Special Topic Quantum Electron., vol. 3, no. 2, pp. 315-319, April. 1997.

80- D. Heo, I. K. Han, J. I. Lee, and J. Jeong, "Study on InGaAsP-InGaAs MQW-LD with symmetric and asymmetric separate confinement heterostructure", IEEE Photon. Technol. Lett., vol. 16, no. 8, pp. 1801-1803, Aug. 2004.

81- G. L. Belenky, C. L. Reynolds, R. F. Kazarinov, V. Swaminathan, S. L. Luryi, and J. Lopata, "Effect of p-doping profile on performance of strained multi-quantum-well InGaAsP-InP lasers", IEEE J. Quantum Electron., vol. 32, no. 8, pp. 1450-1455, Aug. 1996.

82- A. A. Chelny, M. S. Kobyakova, and P Eliseev, "Effect of the doping level of a p-cladding layer on the performance of GaAs-AlGaAs multiquantum-well lasers", IEEE J. Quantum Electron., vol. 40, no. 2, pp. 113-117, Feb. 2004.

83- J. H. Kim, G. M. Yang, S. C. Choi, J. Y. Choi, H. K. Cho, K. Y. Lim, and H. J. Lee, "Delta-doping of Si in GaN by Metalorganic chemical vapor deposition", Jpn. J. Appl. Phys., vol. 38, part 1, no. 2A, pp. 681-682, Feb. 1999.

84- M. K. Kwon, I. K. Park, S. H. Beak, J. Y. Kim, and S. J. Park, "Improvement of photoluminescence by Si delta-doping in GaN barrier layer of GaN/$In_xGa_{1-x}N$ multi-quantum wells", Phys. Stat. Sol. (a), vol. 202, no. 5, pp. 859-862, April 2005.

85- R. Kuchibhotla, J. C. Campbell, C. Tsai, W. T. Tsang, and F.S. Choa, "InP/InGaAsP/InGaAs SAGM avalanche photodiode with delta-doped multiplication region", Electron. Lett., vol. 27, no. 15, pp. 1361-1362, July 1991.

86- I. K. Han, S. H. Cho, P. J. S. Heim, D. H. Woo, S. H. Kim, J. H. Song, F.G. Johnson, and M. Dagenais, "Dependence of light-current characteristics of 1.55-μm broad-area lasers on different p-doping profiles", IEEE Photon. Technol. Lett., vol. 12, no. 3, pp. 251-253, March 2000.

87- N. Hatori, A. Mizutani, N. Nishiyama, F. Koyama and K. Iga, "Threshold reduction of p-type δ-doped InGaAs/ GaAs quantum well lasers by using auto-doping of carbon", Electron. Lett., vol. 33, no. 12, pp. 1096-1097, June 1997.

88- V. Sargũnas, D. A. Thompson , and G. Simmons, "High resistivity in n-type InP by He+ bombardment at 300 and 60 K", Solid-State electron., vol. 38, no. 1, pp. 75-81, 1995.

89- J. T. Hsieh, J. A. Rossi, and J. P. Donnely, "Room-temperature cw operation of GaInAsP/InP double-heterostructure diode lasers emitting at 1.1 μm", Appl. Phys. Lett., vol. 28, no. 12, pp. 709-711, 1976.

90- D. A. Nelson, Y. D. Shen and B. M. Welch, "The effects of proton implant on GaAs isolation properties", J. Electrochem. Soc. Vol. 134, pp. 2549-2552, 1987.

91- J. B. Mitchell, G. Foti, L. M. Howe, J. A. Davies, S. U. Campisano and E. Rimini, "A_channeling investigation of proton and deuteron damage in germanium ", J. Radiation Effects, vol. 26, no. 3, pp. 193-199, 1975.

92- K. Okamoto, H. Ohta, S. F. Chichibu, J. Ichihara, and H. Takasu, "Continuous-wave operation of m-plane InGaN multiple quantum well laser diodes", Jpn. J. Appl. Phys., vol. 46, no. 9, pp. L187-L189, 2007.

93- T. Makino, J. D. Evans, and G. Mak, "Maximum output power and maximum operating temperature of quantum well lasers", Appl. Phys. Litt., vol. 71, no. 20, pp. 2871-2873, Nov. 1997.

94- F. K. Khan, and D. T. Cassidy, "Widely tunable coupled-cavity semiconductor laser", Appl. Optic., vol. 48, no. 19, pp. 3809-3817, July 2009

95- H. Wang, Study of InGaAsP/InP asymmetric multiple quantum well lasers, Ph.D thesis, Engineering Physics, McMaster University, 2006.

96- B. Witzigmann, and M. S. Hybrson, "A theoretical investigation of the characteristic temperature T_0 for semiconductor lasers", IEEE J. S.T. Quantum Electron., vol. 9, no. 3, pp. 807–815, 2003.

97- M. J. Hamp, D. T. Cassidy, "Critical design parameters for engineering broadly tunable asymmetric multiple-quantum-well lasers", IEEE J. Quantum Electron., vol. 36, no. 8, pp. 978-983, Aug. 2000.

98- D. T. Cassidy, and M. J. Hamp, "Diffractive optical element used in an external feedback configurations to tune the wavelength of uncoated Fabry–Pérot diode lasers", J. Mod. Opt., vol. 46, pp. 1071–1078, 1999.

99- T. Suzuki, O. Sasaki, and T. Maruyama, "Absolute distance measurement using wavelength-multiplexed phase-locked laser diode interferometry", Opt. Eng., vol. 35, No. 2, pp. 492-497, Feb. 1996.

100- S. Donati, G. Giuliani, and S. Merlo, "Laser Diode Feedback interferometer for Measurement of Displacements with Ambiguity", IEEE J. Quantum. Electron., vol 31, No. 1, pp. 113-119, Jan. 1995.

101- K. Meiners-Hagen, V. Burgarth, and A. Abou-Zeid, " Profilometry with multi-wavelength diode laser interferometer", Meas. Sci. Technol., vol. 15, pp. 741-746, 2004.

102- C. C. Williams and H. K. Wickramasinghe, "Optical ranging by wavelength multiplexed interferometry", J. Appl. Phys., vol. 60, No. 6, pp. 1900-1903, Sept. 1986.

103- M. J. Hamp and D. T. Cassidy, "Critical design parameters for engineering broadly tunable asymmetric multiple-quantum-well lasers", IEEE J. Quantum. Electron., vol. 36, pp 978-983, 2000.

104- J.W. Goodman, Statistical optics, John Wiley & Sons, 1985.

105- P. E. Ciddor, "Refractive index of air: new equations for the visible and near infrared", Appl. Opt., vol. 35, No. 9, pp. 1566-1573, March 1996.

106- P. R. Bevington and D. K. Robinson, Data reduction and error analysis for physical sciences, New York: McGraw-Hill, Ch. 8, 1992.

107- W. H. Press, S. A. Teukolsky, W. T. Vetterling, and B. P. Flannery, Numerical recipes in fortran, 2nd ed. New York: Cambridge Univ. Press, Chapter 15, 1992.

108- C.E. Shannon "Communications in the presence of noise", Proc. IRE, vol. 37, pp. 10–21, Jan. 1949.

109- E. T. Whittaker, "On the Functions which are Represented by the Expansions of Interpolation-Theory", Proceedings of the Royal Society of Edinburgh, vol. 35, pp. 181-194, 1915.

110- M. Born, E. Wolf, Principles of optics, 6th ed. New York: Cambridge Univ. Press, Chapter 7, 1980.

111- M. Houssa, E. Chagarov, and A. Kummel, "Surface defects and passivation of Ge and III-V interfaces", MRS Bulletin, vol. 34, pp. 504-513, July 2009.

112- N. C. Frateschi, Semiconductor optical amplifier with reduced effects of gain saturation, U.S. PATENT No. US6,891,665, B2, May 2005.

113- J. Lee, M. O. Vassell, and G. J. Jan, "Energy-band diagrams of P-i-N heterostructures for single quantum-well lasers", IEEE J. Quantum Electron., vol. 29, no. 6, pp. 1469-1476, June 1993.